OSAKA UNIVERSITY

PHD DISSERTATION

A research on high energy density plasma generation using X-ray diagnosis

---

Author:
Seungho LEE

Supervisor:
Prof. Shinsuke FUJIOKA

A thesis submitted in fulfillment of the requirements
for the degree of Doctor of Philosophy

in the

Laser Fusion Group, Institute of Laser Engineering
Department of Physics

May 13, 2019

OSAKA UNIVERSITY

Abstract

Department of Physics

Doctor of Philosophy

A research on high energy density plasma generation using X-ray diagnosis

by Seungho LEE

Efficient generation of high energy density plasma (HEDP) is essential for realizing laser fusion energy. In this study, a new HEDP generation method by high-intensity laser was experimentally investigated by spatio-temporal-resolved and spectral-resolved measurement of X-rays.

In the compression of spherical shell fuel used in conventional laser fusion scheme, the hydrodynamic instability, especially the Rayleigh-Taylor instability degrade the compression ratio. A non-uniformity of laser intensity on the fuel, fuel surface roughness, internal defects of fuel can be the source of Rayleigh-Taylor instability. In this study, a solid sphere is proposed as a new shape of fusion fuel for fast ignition. In the compression process of a spherical shell fuel, the spherical shell is accelerated for few tens of nano-second on a hydrodynamically unstable state. Increase in distortion in solid fuel due to hydrodynamic instability is relatively smaller than spherical shell fuel. In the experiment, a solid sphere and a shell are compressed with a high-intensity laser without any spatial smoothing techniques which results in 22 % root-mean-squar of pressure non-uniformity on the fuel surface. A short pulse high-intensity laser is irradiated to a thin metal foil to generate a short pulse of K_α X-ray. An X-ray is imaged using a spherically curved crystal and X-ray transmittance image with high spatial resolution (Δx = 10 μm) and high temporal resolution (Δt = 1 ps) was recorded on the imaging plate. The shadows of the high density core and its temporal evolution was observed when using solid fuel, while no shadows of the high density core was observed using the shell fuel. it is experimentally showed that a solid sphere can be hydrodynamically stable and can be compressed to a high density.

The maximum compression ratio of a solid fuel is determined by the balance of the pressure driven by the laser and the Fermi pressure of the fuel. In order to increase the compression ratio using solid sphere, it is necessary to increase the pressure of the shock wave. In the conventional shock wave generation method, the shock wave is driven by the laser energy deposited near the critical density, 2 to 3 digits lower than the solid density. While a high energy electrons can deposit their energy directly to the over-solid density. The pressure of shock wave can be increased by absorbing high energy electrons behind the shock front. For using this scheme effectively, > 10 % conversion efficiency and < 100 keV temperature electron is required. A new method for efficient generation of high energy electron is studied. We have demonstrated the mixture irradiation of 527 nm and 1053 nm laser results in 150 $\pm$ 21 keV of temperature and 13.1 $\pm$ 2.1 % of energy conversion was measured. While only 527 nm laser irradiation case, 51 $\pm$ 4 keV, 4.5 $\pm$ 5 % of temperature and conversion, respectively, was observed. These experimental results can be explained by a staged electron heating occurs near one-sixteenth critical density of the 527 nm laser which is correspond to quarter critical density of the 1053 nm laser. The two-color laser irradiation is a novel approach for efficient production of hot

electrons and opens a new frontier of laser plasma interaction research.

This research has succeeded in proposing and demonstrating a novel method, which is completely different from the conventional method in high density plasma generation and high density plasma heating. This result will greatly contribute to the development of future high energy density scientific research.

Acknowledgements

First of all, I would like to express the endless gratitude to my supervisor, Prof. Shinsuke Fujioka for his continuous encouragement, guidance and many discussions on researches for more than four years. He give me the opportunity to do a Ph.D. course, and provided me a lot of supports not only on the research but also on the life Thanks him, I could grow as a high energy density plasma experimentalist, i could publish my dissertation. I would like to appreciate Prof. Yoshitaka Kuno for giving me advices and discussion on this dissertation. I would like to appreciate Prof. Mitsuo Nakai for discussing on my dissertation and give me a lot of comments on the research. I would like to appreciate Prof. Yasuhiko Sentoku for the discussion on my dissertation and researches. I would like to appreciate Assistant Professor. Takayoshi Sano for giving me a lot of discussions on two-color laser plasma interaction and on this dissertation. I would like to thank Prof. Hiroyuki Shiraga who was my supervisor of my master course. He suggested me to use an X-ray diagnostics. Emeritus Prof. Kunioki Mima and Emeritus Prof. Hiroshi Azechi give me a lot of theoretical discussions on two-color laser plasma interaction. So i would like to give a thank them. I would like to thank Associate Professor Hiroshi Sawada (University of Nevada), for helping development for X-ray spectrometer and imaging system, Mr. King Fai Farly Law, ,Mr. Kazuki Matsuo and Mr. Hiroki Morita for supporting my experiment and give a lot of physical discussion. II would like to acknowledge to Associate Prof. Tomoyuki Johzaki (Hiroshima University), Dr. Atsushi Sunahara (Purdue University), Associate Prof. Hideo Nagatomo, Prof. Hitoshi Sakagami (National Institute for Fusion Science: NIFS), Dr. Natsumi Iwata, Dr. Takashi Shiroto and Dr. Daiki Kawahito. They supported me on the analysis of experimental data by theoretically and computationally. I would like to thank laser operation group : Mr. Koji Kawabata, Mr. Yuhei Kawakami, Mr. Tetsuji Kawasaki, Mr. Shinji Urushihara, Mr. Kiyonobu Sawai, Mr. Takayasu Sakamoto, Mr. Keisuke Takahashi, Mr. Yoshinori Kubota and Mr. Osamu Maegawa. I would like to thank target fabrication group : Ms. Hitomi Hosokawa, Mr. Mizuho Nagata, Ms. Yumi Kaneyasu, Assistant Prof. Kohei Yamanoi and Prof. Takayoshi Norimatsu. Finally I am grateful to my family for endless support of my life.

Contents

Chapter 1

Introduction on high energy density plasma

A high energy density(HED) plasma exists in space such as planets, stars, and neighborhood of them. The HED state is defined as a physical system with a pressure exceeds 1 Mbar. The pressure of 1 Mbar is a value determined from the typical Fermi pressure of a matter(For ice DT, Fermi pressure = 0.164 Mbar). Matters in HED state can not keep their normal state anymore, are either compressed or are expanded. Exploring HED plasma physics leads us understanding such planets and stars. Especially controlling a nuclear fusion energy, which is an energy source to keep the stars shining, leads to humanity obtaining a semi-permanent energy source. One of the most attractive scheme to generate HED plasma on the earth is the inertial confinement fusion(ICF)[34]. Achieving an ignition is a grand challenge for ICF research. The ignition is defined as a state which a nuclear fusion continues using its own nuclear fusion energy without any external energy source.

1.1 The first ignition design

In the center core of the Sun, hydrogen is exist at more than 150 g/cc(thousand times solid density) , and at pressures larger than 100 Gbar (10^{11} times of atmosphere pressure) and 2 keV temperature. These pressures are maintained by the gravity. The nuclear fusion occur in the core of the Sun, which maintaining the internal energy of the Sun. The most active fusion reaction is the fusion of deuterium D and tritium T.

$$D + T = \alpha(3.5\ \text{MeV}) + n(14.1\ \text{MeV}) \tag{1.1}$$

As a result of the fusion, α particle with 3.5 MeV kinetic energy and neutron with 14.1 MeV kinetic energy are generated. These kinetic energies are absorbed inside the core, the internal

energy is maintained.

Humankind tried to use this energy on the earth and have been developed many techniques. The most critical issue was how to confine such high pressure, high temperature plasma. There are two method for confining a plasma using magnetic field (magnetic confinement fusion : MCF) and inertia(ICF). In this dissertation, only about ICF will be discussed. In ICF, a fuel is confined by the inertia of accelerated fuel. The fuel is accelerated by irradiating the fuel surface with high intensity laser. As a reaction of blow off of the fuel surface, target is accelerated. For compressing hydrogen to 150 g/cc densities and > 5 keV temperature, 100 Gbar pressure should be realized using other than gravity. The pressure applied to an implosion system generating kinetic energy then it is converted to internal energy. Because pressure is energy density, the maximum average pressure equals the applied pressure multiplied by the compression ratio. Also, the additional pressure increase occurs near the center of the core because of convergence effects. To minimize the required implosion pressure (laser intensity), the Fermi-degenerate state should be achieved during compression process. The isentropic compression can be achieved by shaping the laser pulse in time. When implosion starts, the initial laser intensity is set the initial shock speed in the fuel is comparable to sound speed (1 Mbar) and subsequently increase the laser intensity to achieve the quasi-isentropic. Owing to the convergence effect, and by adjusting the laser pulse shape for all accelerated particles intersect near the center of the core, the fuel is compressed and heated. A radiation hydrodynamic simulation was used for the ignition calculation. In the simulation, 60 kJ of laser energy were used for one micron wavelength laser. A solid sphere fuel which is consisted of liquid DT having 0.4 mm radius is irradiated by the pulse shaped laser. The laser intensity is applied from the initial intensity of 10^{13} to the maximum intensity of 10^{17} W/cm^2 within 20 ns. The calculated results shows that the fuel can be compressed to 1000 g/cc density and 10 keV temperature. However, the laser intensity above 10^{15} W/cm^2 used here and it was not appropriate for realization of ICF because of lowering of laser absorption and non-thermal electrons generated by the laser plasma instabilities which is the source of preheat. For reducing the maximum laser intensity, a spherical shell target was adapted for ICF. Because the shell target have low mass, lower laser intensity is required for accelerating the fuel to $3 \times 10^7 cm/s$, compare to solid fuel. A shock speed is proportional to the square root of pressure while the shell speed is proportional to the pressure. Using shell target was more appropriate choice for reducing the maximum laser intensity.

1.2 Central hotspot ignition

A small spherical fuel is directly or indirectly irradiated by a high intensity (10^{15} W/cm^2) laser. The laser energy (direct) or radiation energy (indirect) heat the fuel surface so that the thermal pressure of fuel surface increases. A thermal pressure gradient towards the center of spherical fuel, the fuel is accelerated toward the center. The accelerated fuel collides at the fuel center, a kinetic energy is converted to an internal energy within hundreds of pico-second. This is called stagnation, which is a confined state by an inertia of the accelerated fuel. Within stagnation, nuclear fusion reaction occurs. This method is called a central hotspot ignition which is a conventional ICF method.

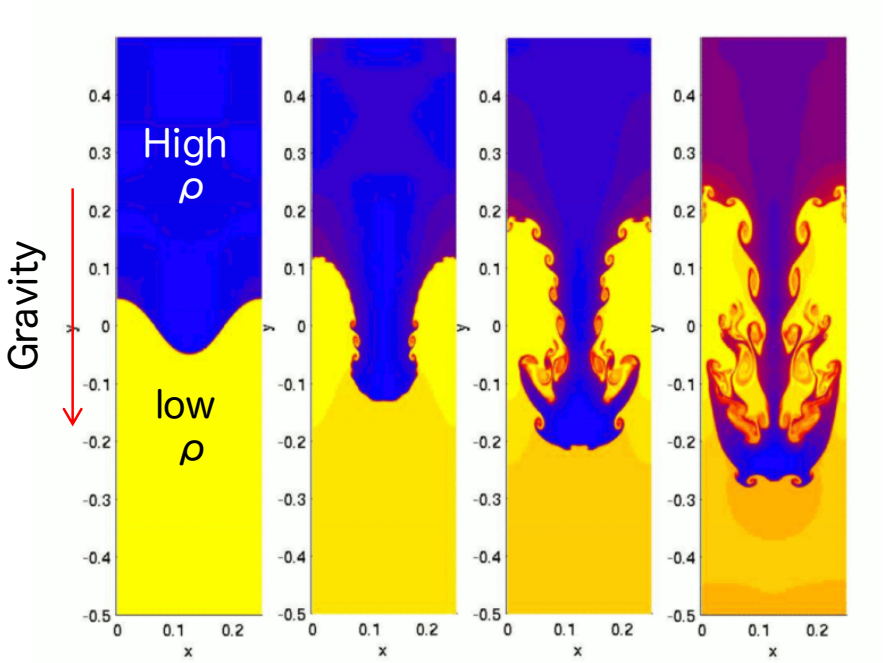

FIGURE 1.1: A image of Rayleigh Taylor instability. Figure taken from Li, Shengtai and Hui Li. ?Parallel AMR Code for Compressible MHD or HD Equations?.

Using central hotspot ignition method, the ignition seemed to achievable efficiently. However, in central hotspot ignition, stringent requirements for fuel and lasers are exist due to a hydrodynamic instability such as Rayleigh-Taylor instability (RTI). RTI is an instability of an interface between two fluids of different densities which occurs when the lighter fluid is pushing the heavier fluid, as shown in Fig. 1.1. The outer part of the shell feels outward gravity of the sphere as a reaction of the instantaneous acceleration toward the sphere center. And a

density gradient toward the center. In this situation, the initial perturbations on the fuel temporally grows exponentially by the RTI. It may breaks the fuel and degrade the compression ratio. Also, in deceleration phase, which is the timing after the compression pressure is lower than the plasma pressure, perturbations inside of the fuel shell grows with the same manner for acceleration phase.

Due to RTI, the initial perturbation should be controlled. A spatial non-uniformity of laser intensity on the fuel surface and the defect of the fuel and the non-sphericity of the fuel can be the source of the RTI. To suppress the initial perturbation, many techniques have been developed. The coherent laser beam have a large spatial intensity non-uniformity due to the interference with neighborhood. A random phase plate(RPP) was developed to shift the phase distribution randomly[52, 19, 36]. It makes the laser intensity smooth while there still exist high spatial mode spike. Smoothing by spectral dispersion (SSD) techniques were also developed[47]. By using SSD with RPP, a high spatial mode spike can also be smoothed. Also a target fabrication techniques have been developed and now it is still being developed.

Another approaches to reduce the effect of RTI have been developed. Reducing the growth rate of RTI can also suppress the effect of RTI. A mid-Z material doping to the ablator[3, 15], slow implosion and generating decaying shock wave using picket pulse before driving the main shock wave[21] can reduce the growth rate of RTI. All of these techniques should be used when implode the shell fuel.

1.3 Fast ignition

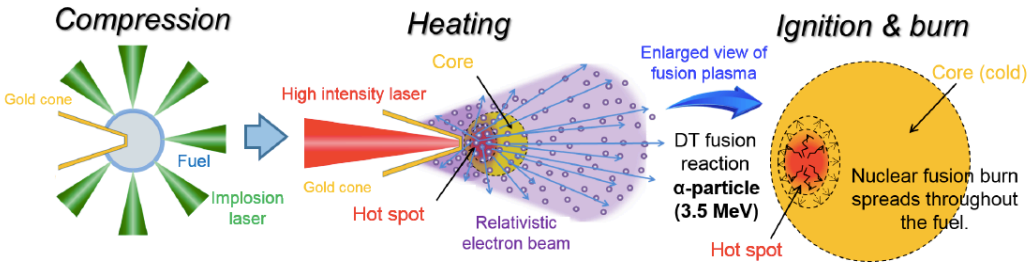

FIGURE 1.2: The concept of fast ignition.

Fast ignition (FI) is an advanced scheme of ICF which was proposed by Tabak, *et.al*.[49]. A schematic view of a concept of FI is shown in Fig. 1.2. In FI, the target is compressed to a high density by a nano-second laser pulse and heated by a high-intensity short laser pulse

generated particles (electrons or ions). Unlike the central hotspot ignition, FI separates the processes of fuel compression and heating. The laser intensities of them is typically 10^{15} W/cm^2 for the compression laser and 10^{19} W/cm^2 for the heating laser. FI has two advantages compare to conventional central hotspot ignition : efficient generation of the fusion plasma and less requirements on symmetry. FI targets are ignited by a high energy particle beam, the pressure of compressed core can be less than that of central hotspot ignition. The hotspot pressure is typically designed as the 4-5 times of Fermi pressure in central ignition to generate high temperature plasma at the center. Hereafter, the pressure divided by the Fermi pressure is defined as adiabat. While in FI, the compressed core pressure can be designed almost same as Fermi pressure ideally (adiabat 1). Of course, it is technically difficult to compress the fuel without any entropy increase. While it have to be refer here low adiabat design is acceptable in FI but never in central hotspot ignition. Therefore, a larger compressed core can be achieved compare to central hotspot ignition with a same laser energy. This makes the energy gain large. Also, due to such reason, non-symmetrical compression is acceptable, even it degrades the compression rate.

1.4 Challenges in fast ignition

In FI, generating a ignition condition plasma, with areal density > 0.5 g/cm^2 and temperature > 10 keV is the grand challenge. The ignition condition is defined as the state which plasma keep their internal energy without any external source by using fusion energy. Firstly, this ignition condition shown above is the iso-choric ignition condition[]. In FI, the time scale of heating process is almost same as the heating laser pulse duration. Few tens of ps is instantaneous for the hydro motion. Thus, during the heating, the volume of the compressed core does not change. The high energy density plasma can not keep their energy because they emits radiations, expands, and conducts heat to their neighborhood cold plasma. Once the ignition condition is reached, core plasma can maintain its own temperature by fusion energy, but to reach that point it must be overcome such energy losses.

There are some issues for the realization of ignition condition.

- A high density core plasma generation which have areal density larger than the range of high energy electrons.
- Increasing the laser to core coupling by suppressing the high energy electron beam divergence.

A stable core plasma formation and a high density core generation which have areal density more than the range of high energy electrons, are the issues on fuel compression. A compression of shell target is unstable due to hydrodynamic instabilities. Many ideas have been studied for reducing the hydrodynamic instabilities. Physical approaches such as using slow implosion, mid-Z material doped ablator were developed. Technical approaches for reducing the initial perturbation such as a target fabrication method, laser spatial smoothing techniques have been developed. While it is still not easy to generate the high density core plasma using shell target because upper techniques should be thoroughly controlled.

In heating process, a large divergence of high energy electrons degrade the energy deposition due to a stand-off distance from the electron source to the core plasma. The high energy electrons are generated at under solid density plasma. While core plasma is generated near the center of the spherical fuel, and it is typically about a radius of the spherical fuel. For ignition scale plasma, the fuel radius is typically 1 mm. While the electron have a large divergence, i.e., 50 $^\circ$ of half spray angle and increases with laser intensity. To achieve the efficient heating, shorter stand-off distance or smaller divergence angle should be achieved. The stand-off distance can be reduced by changing the pressure balance of the fuel surface, while it results in degrading compression ratio due to non-symmetricity. Suppressing the electron beam divergence is appropriate choice.

1.5 Outline of dissertation

In this dissertation a solid fuel, a new shape of FI fuel, will be introduced. Its stability was experimentally observed, and radiation hydrodynamic simulation suggest that a solid fuel can be compressed to the ignition scale (areal density $> 1\mathrm{g/cm}^2$) by using tailored laser pulse. The maximum laser intensity determines the maximum compression ratio. For generate high pressure with low intensity laser, there were one choices : using shorter wavelength. A shock pressure enhancement using high energy electron is the fascinate scheme for reducing the required maximum laser intensity for ignition. Also, in the fast ignition experiment, a quantitative understanding of the physical process of FI is also introduced by using X-ray diagnosis.

In chapter 2, the X-ray diagnosis which were used in this research, are introduced. By using several X-ray diagnostics, we can understand about the HED generation process.

In chapter 3, a new target shape for FI, a solid fuel will be introduced and an experiment on solid fuel compression is described. Flash K_α backlighting method was used for measuring the plasma density. A measured core plasma image shows that the solid fuel is effective for FI

target and stable than shell target. Also, an adiabatic compression for generating high density plasma is also introduced.

In chapter 4, it is described on non-thermal hot electron generation using two-color lasers plasma interaction. In this study, as an efficient generation method of this high energy electron, plasma was irradiated simultaneously with two laser beams, which have different wavelengths and one of which is twice as long as the other. A nano-second laser generated hot electrons can be used for a shock pressure enhancement and a magnetic field generation.

In chapter 5, the experiment on FI with and without magnetic field is described. Using a heating model, the experimental data was analyzed. By measuring the absolute number of Cu-K_α X-ray, the energy coupling efficiency from laser to the core plasma is estimated.

And concluded in chapter 6.

Chapter 2

X-ray diagnosis

For understanding the physics of HED plasma generation, spatially resolved and/or temporally resolved measurement of physical parameters is necessary : electron/ion temperature, density, size of the plasma, etc. HED plasma generated by FI is typically indicates over-solid density and/or over keV temperature plasma. A X-ray diagnosis is a powerful method for exploring the HED plasma. Due to its high optical depth for visible lights, those are absorbed inside the plasma. So that no internal informations are contained in visible light. X-rays having a longer range than the thickness of the plasma, it can transmit the internal information of the plasma to the outside. By measuring them, it leads us understanding of the inside of HED plasma. Sometimes X-ray sources can be used as a probe for exploring the HED plasma like X-ray backlighting. In this section, some HED plasma diagnosis techniques using X-ray will be introduced.

2.1 X-ray Spectroscopy using flat crystal

A plasma is consisted of three particles : ions, electrons and photons. Almost of electrons in low temperature plasma are originally trapped to an ion potential. When a plasma gain energy, electrons may obtain kinetic energy which is enough to escape the ion potential. Electrons having enough kinetic energy then escape from the ion potential. Ot free electrons may captured into the ion potential. In these processes, photons are generated and/or absorbed. So the plasma emits X-rays and absorbs X-rays. As a result of a radiation transport, the X-rays are transmit to the outside of plasma. The X-ray spectrum thus contains informations of the plasma parameters.

2.1.1 temperature measurement

The X-ray spectrum is affected by the plasma parameters : electron, ion temperature, density, size. Among them, the electron temperature is the most effective parameter for changing the

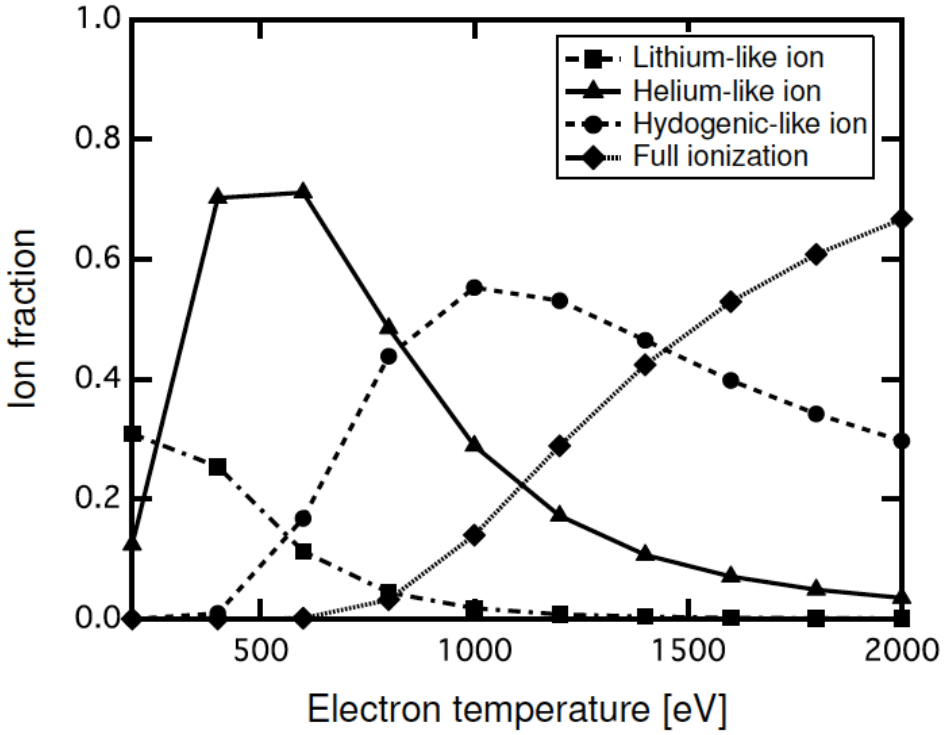

FIGURE 2.1: Electron temperature dependence of occupancy ratio of chlorine (C) ions calculated by FLYCHK.

X-ray spectrum. An X-ray having higher photon energy is generated from a higher ionized ions. Due to the thermal motion of electrons, the trapped electrons can excited mainly by the collisions of the thermal electrons. As the electron temperature of plasma increases, ionization by electron collision progresses and the occupancy density of high valence ions increases. Fig. 2.1 shows the electron temperature dependence of the occupancy ratio of chlorine ions calculated by the FLYCHK code. As the electron temperature of plasma increases, ionization by electron collision progresses and the occupancy density of highly ionized ions increases. When the tracer substance becomes He-like or H-like, from the hydrogen-like ion Lyα line (1s-2p), Lyβ line (1s-3p) and etc. are emitted, and from helium-like ion Heα line ($1s^2$-1s2p), Heβ line ($1s^2$-1s3p) and etc. are emitted. The intensity ratio of these resonance lines contains the information of the ion valence of the plasma and is a function of the electron temperature. Therefore, the electron temperature can be derived from the intensity ratio of these line X-rays

2.1.2 electron density measurement

A plasma density affect to the line shape. A state energy of trapped electrons are affected by the external electric potential. Typically, a static electric potential of neighborhood ions and a collisional potential perturbation due to electrons affect to the energy level. Because the photon energy of line emission (bound-bound transition) is determined by the energy level, the perturbed energy level results in generating different photon energy X-ray. This is called Stark broadening. However, there are several factors affect to the line shape : natural broadening, Doppler broadening, Stark broadening, opacity broadening, source size broadening, and the perfectness of the crystal. We should consider all broadenings to get a value of the Stark broadening.

Natural broadening

Natural broadening is determined from the quantum limitations, and this can be expressed like $\Delta E_{\mathrm{nat}} = h/(2\pi A_0 e)$. Here h, A_0, e is Plank constants, a life time of upper state and elementary charge respectively. A typical A_0 is 10^{-8} s which is correspond to $\Delta E_{\mathrm{nat}} = 6.58 \times 10^{-8}$ eV Full Width Half Maximum(FWHM) of Lorentzian profile broadening. Natural broadening is not the dominant broadening effect for almost of experiment and is not often directly observed, except in the line wings.

Doppler broadening

The X-ray is emitted from the trapped electrons in the ion. Due to the thermal motion of ions, the electron energy levels of the ions is broadened because of Doppler effect. The formula for Doppler broadening $\Delta E_{\mathrm{Doppler}}$ is expressed as

$$\Delta E_{\mathrm{Doppler}} = E_0 \sqrt{\frac{8eT_{\mathrm{eV}} \ln 2}{Am_{\mathrm{p}}c^2}}. \tag{2.1}$$

Here, E_0, e, T_{eV}, A, m_{p}, c is the photon energy of the spectrum line, the elementary charge, the ion temperature in unit of eV, the atomic weight of ion, the mass of proton and the speed of light, respectively.

Stark broadening

Considering the radiation from ions in high density plasma, the influence of microscopic electric field by particles around it can not be ignored. In other words, when the density of plasma

increases and the average interatomic distance approaches the orbit radius of electrons, bound electrons are affected not only by nuclei but also by surrounding electrons and ions, and perturbations occur in the excited levels. This is called the Stark effect. If the size of the direction of the external field is uniform, a line shift occurs, but since there is a spread in the size of the direction of the external field in the plasma, the observed line X-ray causes an energy spread. This spread is called Stark broadening and strongly depends on the electron density of the plasma. Therefore, it is used for electron density diagnosis of high density plasma. As the theory of Stark broadening, quasi-static approximation mainly considering the influence of slow moving ions and collisional approximation considering fast moving electron collision are considered. In the quasi-static approximation, the broadening occur with Gaussian shape, in the collisional approximation, the broadening occur with Lorentzian shape.

Opacity broadening

When the plasma is optically thick, the X-rays emitted in the plasma undergo self-absorption of the plasma. Opacity is an index that indicates the optical thickness in a plasma, and when the self-absorption effect of the plasma is large, it is a plasma with a large opacity. Since the vicinity of the center of the emission spectrum is relatively large due to the reabsorption effect, the vicinity of the peak of the spectrum shape is suppressed and the spectrum width is observed as if it were effectively expanded.

Source size broadening

When using flat crystal, without any pinhole or imaging, the finite size of X-ray source makes the line broad. That is because the Bragg condition is only determined by the incidence angle of the X-ray. When the crystal surface is big enough compare to the plasma size (typically the crystal surface size > 1cm is much bigger than plasma size < 1 mm), X-rays having same energy generated from difference points are detected in different points on the detector. The source size broadening is expressed as below.

$$\Delta h\nu_{\text{source}} = \frac{D \cdot h\nu}{l} \frac{\cos\theta_{\text{B}}}{\tan\theta_{\text{B}}}, \tag{2.2}$$

where $h\nu$, D, l, θ_{B} are the photon energy, the X-ray source diameter, the distance between the source and the detector, and the Bragg angle, respectively.

Perfectness of the crystal : rocking curve

A rocking curve shows the perfectness of the crystal. The rocking curve is an intensity distribution for changes in diffraction conditions. If the crystal is perfect single crystal, then the rocking curve has a very sharp peak at the Bragg condition. If the orientation of crystal plane is not perfect and/or crystal have some defects, then the rocking curve spread. For the single crystal, the rocking curve determines the limitation of the photon energy resolution as expressed below.

$$\Delta\theta_B = \frac{\tan\theta_B}{E}\frac{\Delta E}{E} \tag{2.3}$$

It is important to refer here that for a mozaic crystal, which will be discussed later, rocking curve does not determine the limitation of the photon energy resolution because of a para-focusing effect.

A plasma size also affect to the line intensity and its shape. All X-ray lines have different opacity according to its emission type. For example, a resonance line emission have much larger opacity than a satellite line emission because it is generated by the resonance process between X-ray generation and absorption. So, the resonance line intensity typically can be reached to the black body intensity. While the satellite line, which is unstable state that more than two electrons are excited by the electron collision. Due to its unstability, the emission can not be generated resonantly, but spontaneously generated. Fig. **??** shows the X-ray spectrum having large dependence on the plasma size.

2.1.3 Bragg diffraction

X-ray diffraction due to periodic structure of a crystal atoms, is used for X-ray spectroscopy. The only X-ray photon energy satisfying the following condition is diffracted.

$$2d\sin\theta_B = n\lambda \tag{2.4}$$

where d, θ_B, n, λ is the distance between two lattice, the Bragg angle, the order of diffraction, and the wavelength of the X-ray, respectively. This is called Bragg condition.when

2.1.4 Single crystal diffraction

A single crystal have a regular arrangement of elements. Due to the single crystal is close to ideal condition, high photon energy resolved X-ray spectrum can be obtained. Due to the flatness and/or defects inside the ctystal, the Bragg condition have finite bandwidth. The typical

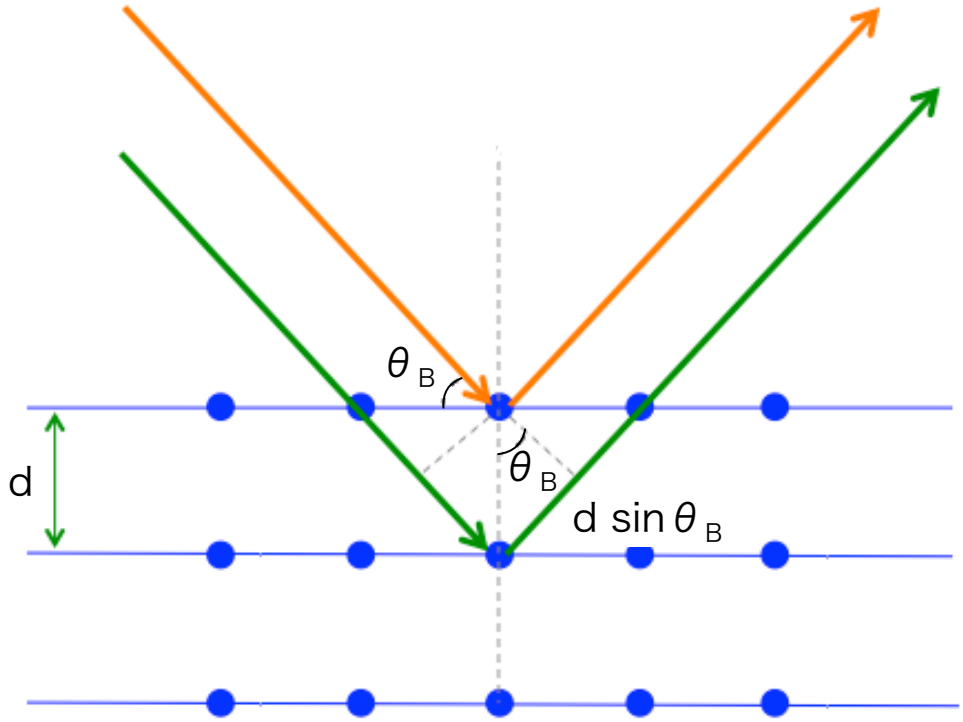

FIGURE 2.2: The principle of bragg diffraction. Blue circles are atoms of crystal, d is the spacing of the crystal surfaces. θ_B is the Bragg angle. The light path difference is to be $2d\sin\theta_B$

energy resolution $\Delta E/E$ is 10^{-5} ~10^{-4}. For example, 8 keV X-ray can be measured with 0.8 eV resolution. From the differential of Bragg condition by the photon energy, we can get the following result.

$$\Delta\theta_B = \frac{\tan\theta_B}{E}\frac{\Delta E}{E} \tag{2.5}$$

From this equation, the allowable anglular deviation $\Delta\theta_B$ is to be $10^{-3} - 10^{-4}$ [deg] for typical single crystal.

2.1.5 Mosaic crystal diffraction

Mosaic crystal is the crystal consisted of many single crystallites. Those surface of the crystallites are randomly oriented. Using some techniques those orientations can be controlled. The orientation angles have a distributions and the FWHM is defined as the mosaic angle. The mosaic crystal can be used as a X-ray spectrometer with high reflectivity. A spectroscopy with

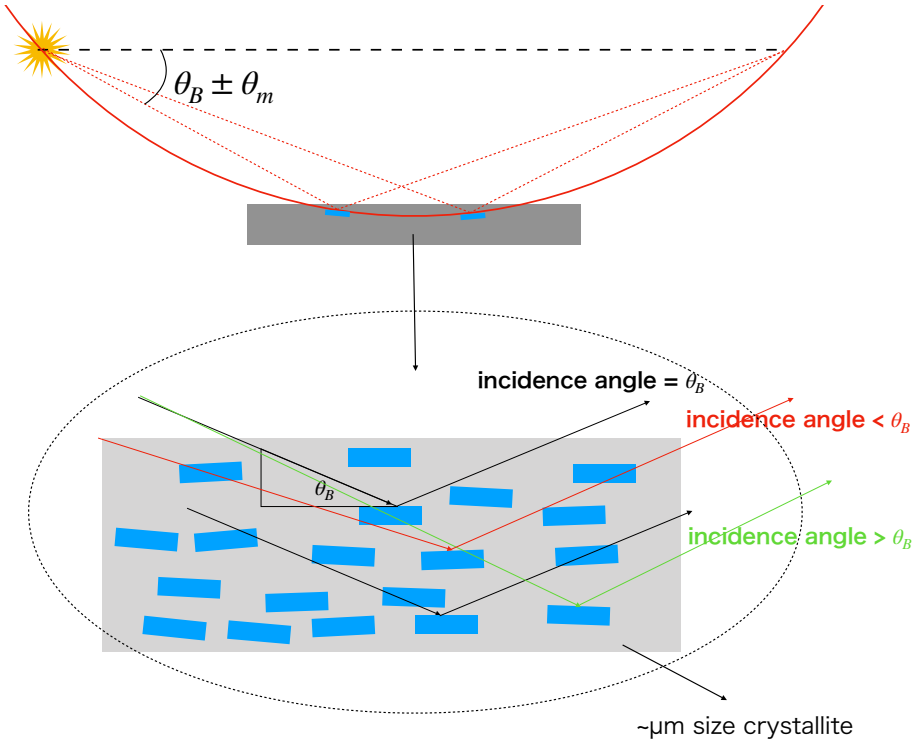

FIGURE 2.3: (a) The image of X-ray diffraction by the mosaic crystal. Due to the randomness of the small crystal pieces, the X-ray diffraction angle become wider than the single crystal one. In our system, for a single X-ray photon energy, the total surface and inside of the mosaic crystal is used for the diffraction. Because of the para-focusing effect, the photon energy does not degraded if the detector is placed the right position. (b) A mosaic crystal is consisted of small pieces of crystal and those randomness enables the diffractable photon energy.

higher dynamic range in X-ray intensity is become possible when using higher reflectivity crystal.

Fig. 2.3 shows the simple image of the mosaic crystal diffraction. Due to the randomness of the crystallites orientations, the Bragg condition is mitigated. The allowable angular deviation in mozaic crystal is equal to the mozaic angle, typically 0.5 °. This value is about 500 times higher than the single crystal one. According to Eq. 2.5, the increase of Bragg angle deviation results in spread of photon energy, which means low energy resolution. In the case of mosaic crystal, however, the photon energy resolution does not change because of para-focusing effect. The para-focusing effect can be understandable by imagining the virtual circle passing through the crystal. When the X-ray source and the detector is placed on the plane parallel to the crystal surface plane, all diffracted X-rays are collected on the detector. Also, we can think innumerable circles passing through the crystal, the totally diffracted number increase. From this reason, the integral reflectivity of the mosaic crystal is much larger than that of single crystal.

Here the integral reflectivity of the mosaic crystal and the single crystal is shown in Table. 2.1

TABLE 2.1: The specs of flat crystals for X-ray spectroscopy used in this work.

Crystal	Crystal orientation	mosaic angle [°]	2d [Å]	integrated reflectivity [mrad]
HOPG ZYA	2023	0.39	2.749	15.0
HOPG ZYB	2023	0.49	2.749	16.0
ADP	2131	-	3.082	0.13

Thickness effect

Due to the mozaic structure, the X-ray can penetrate to the direction of the thickness more than the single crystal, because the number density of crystallite satisfying the Bragg condition is smaller than the single crystal. the X-ray can be reflected from the deeper point of the crystal surface. The reflectivity of the thicker crystal is higher than the thiner mozaic crystal and saturated according to the attenuation effect inside the crystal. A highly oriented pyrolytic graphite(HOPG) was used in this research. According to the preliminary research[], the reflectivity of the HOPG crystal increases with the increase of the thickness and saturated around 1 mm thickness, as shown in Fig. 2.4 (a). Also, over 1 mm thicnkess crystal, the attenuation of the X-ray reveal on the detector which results in non-symetric spectrum broadening having high energy tail, as shown in Fig. 2.4 (b).

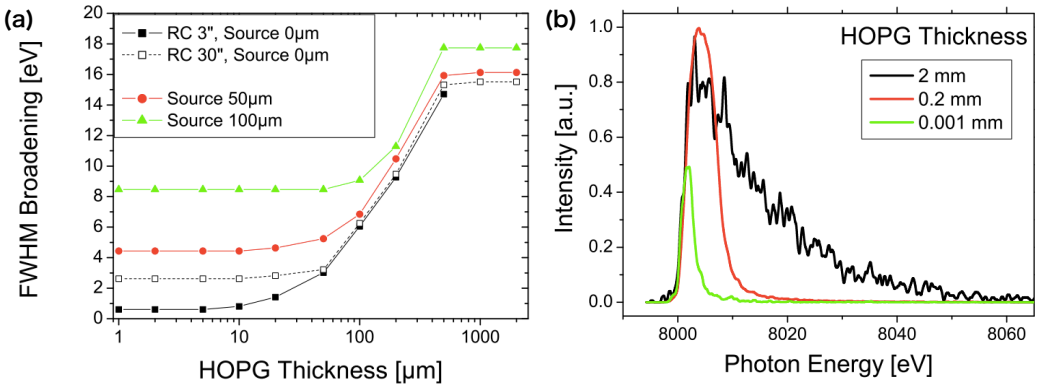

FIGURE 2.4: Ray tracing simulation result for spectrometers with 0.4 ° mosaicity using monochromatic 8.0 keV photon energy line. (a) The line broadening of the spectrum as a function of crystal thickness for different rocking curve(RC) width and size of the source. (b)The spectral profiles for an ideal point source as function of thickness.

Here it should be noted that, using HOPG crystal, pinhole is not usable anymore. Because pinholes having solid angel smaller than the mozaic angle makes the signal extremely small.

2.2 Flash K_α X-ray backlighting with high-power short-pulse laser

2.2.1 X-ray imaging using spherically bent crystal

Multi keV X-ray radiography or imaging the plasma self-emission with bent crystal X-ray mirror is an invaluable technique in HEDP research. Bent crystal imaging can provide monochromatic($\Delta E/E = 10^{-3}$), high spatial resolution($\Delta x = 10\mu$m) image. Monochromaticity allow for an easier interpretation compared to broad-band images.

Only X-rays that satisfy the Bragg condition are reflected by the crystal lattice. The crystal behaves like a mirror for X-rays satisfying the Bragg condition. Then the bent crystal can behaves like a concave mirror. The lens formula can be applicable for this.

$$\frac{1}{a} + \frac{1}{b} = \frac{1}{f} \tag{2.6}$$

where, a is the distance from the object to the crystal and b is the distance from the crystal to the imaging point and f is the focal length of the crystal. The focal length of the crystal is related to

the curvature radius R. Usually, $f = R/2$ when using on the normal direction of the spherically bent crystal. The spherically bent crystal must be used at near-normal direction for reducing the aberrations. Aberrations occur due to the difference of curvature radius between sagittal plane and meridional plane. The paraxial lens equations for image formation of a toroidal crystal are shown below.

$$\frac{1}{a} + \frac{1}{b} = \frac{2}{R_m \sin\theta_B} \tag{2.7}$$

$$\frac{1}{a} + \frac{1}{b} = \frac{2\sin\theta_B}{R_s} \tag{2.8}$$

where a is the distance from the crystal to the object, b is the distance from the crystal to the image. R_m is the curvature radius in the meridional plane, and R_s is that in the sagittal plane. A spherical crystal has the curvature radius $R = R_m = R_s$. When using spherically bent crystal imaging an object placed on off-normal axis, the effective focal length are changed on two plane : meridional plane and sagittal plane. Those two plane can be understand from Fig. 2.6. The meridional plane is the plane which contains the crystal normal direction (dashed line in

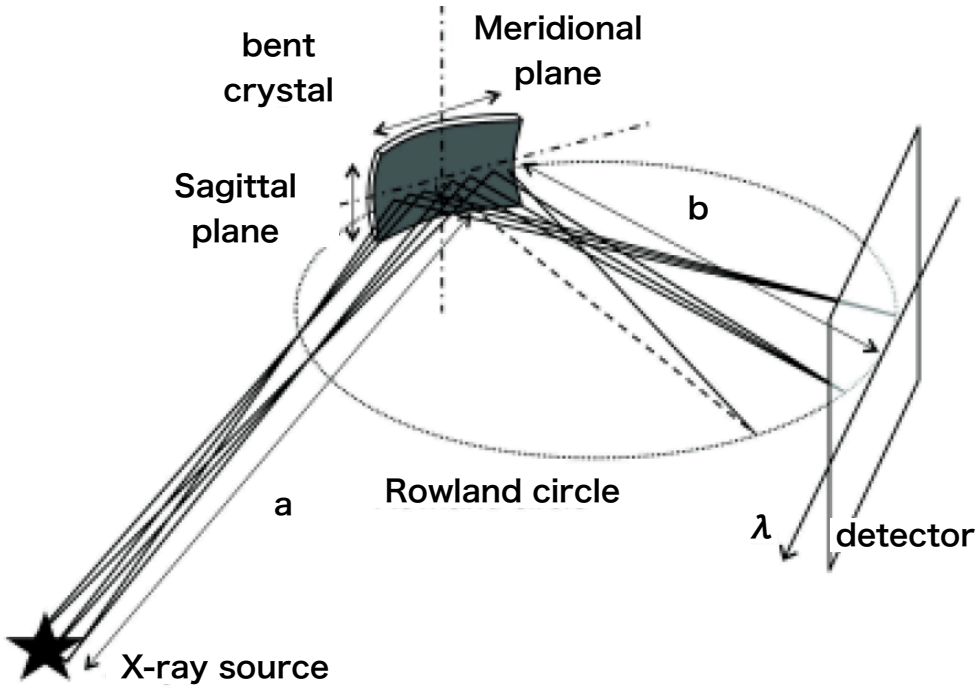

FIGURE 2.5: The schematic image of X-ray imaging with bent crystal. The meridional plane is the plane which contains the crystal normal direction (dashed line in Rowland circle) and the X-ray source - crystal center line.

Rowland circle) and the X-ray source - crystal center line. The sagittal plane is perpendicular

plane of the meridional plane. For $\theta_B < 90^\circ$, the meridional f_m and sagittal f_s focal lengths are different shown below.

$$f_m = \frac{R_m}{2} \sin\theta_B, \tag{2.9}$$

$$f_s = \frac{R_s}{2} \frac{1}{\sin\theta_B}. \tag{2.10}$$

We can get the condition of those two focal lengths are equal.

$$R_s = R_m \sin^2\theta_B. \tag{2.11}$$

From this, those two curvature radius can not be the same except $\theta_B = 90^\circ$. The difference of the focal length between two plane results in the aberration. Less than 30 μm spatial resolution is achievable, when θ_B>87° for measuring self emission, and θ_B> 70 for measuring backlight image. Less than 10 μm spatial resolution is achievable, when θ_B>88° for measuring self emission, and θ_B> 80 for measuring backlight image. These are shown in Fig. **??**

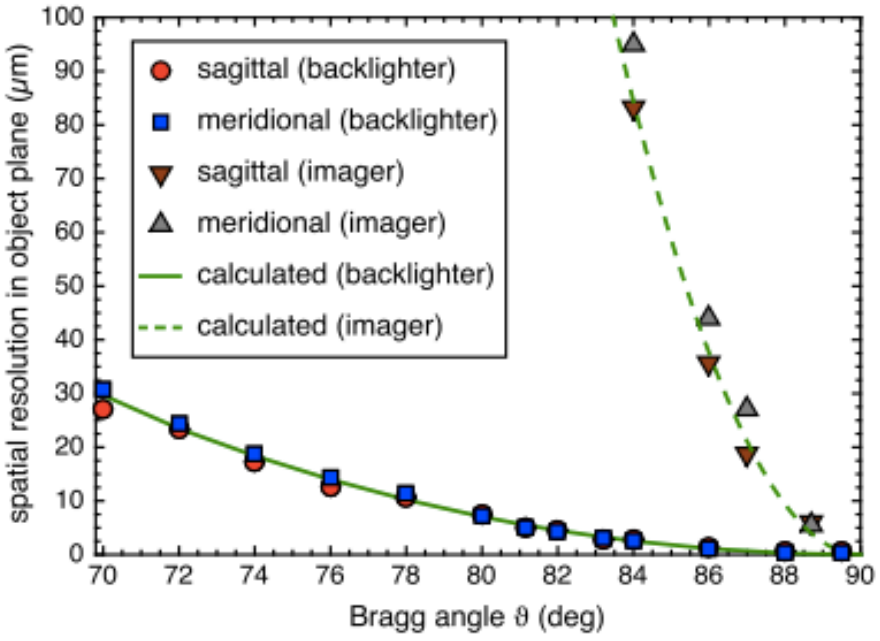

FIGURE 2.6: The Bragg angle dependence of theoretical limitation of spatial resolution for self-emission imaging system and for backlighting imaging system[].

Crystals used in this research are shown in table. **??**. Spherically bent Quartz(2131) crystal was used for Cu-K_α imaging and Quartz(2023) crystal was used for Ti-K_α imaging.

TABLE 2.2: The specs of spherically bent crystals used in this work.

Crystal	Crystal orientation	2d [Å]	Reflection order	Curvature radius [mm]	X-ray
Quartz	2023	2.749	1	200	Ti-K_α (4.541 keV)
Quartz	2131	3.082	2	200	Cu-K_α (8.048 keV)

2.2.2 Flash K_α X-ray generation using high-power short-pulse laser

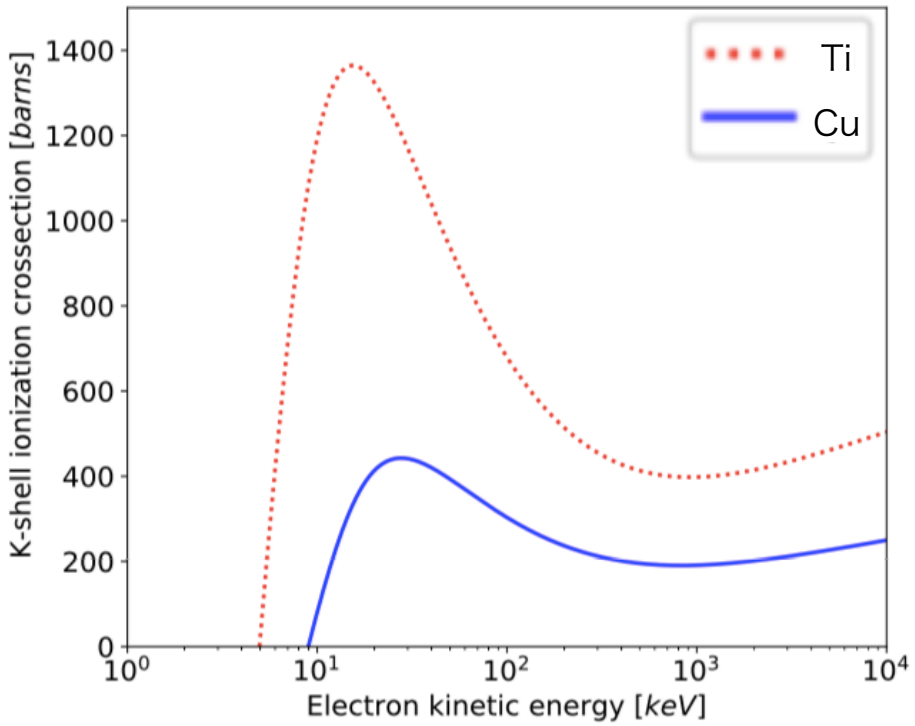

FIGURE 2.7: The K-shell ionization cross-section of Ti (red dotted) and Cu (blue solid).

X-ray backlighting is widely used for measuring the density of the plasma. The typical velocity of HEDP is 1×10^7 cm/s. A snapshot of density distribution measurement is necessary for understanding the process of HEDP formation due to compression especially . The limit of spatial resolution of spherically bent crystal is 10 μm. The traveling time of plasma with length of 10 μmis then, 10 ps. If the temporal resolution is longer than 10 ps, the spatial resolution of the image is degraded by the motions of plasma.

The Flash K_α X-ray source using high-power short-pulse(ps) laser is developed. K_α X-ray is generated from the inner-shell ionized ions. Due to the inner-shell ionization is caused by the hot-electrons having energy larger than K-shell ionization energy of ion. High-power short-pulse laser can generate electron beam which have pulse duration same as the laser pulse duration. K_α X-rays generated by electron beam then have a duration of emission same as the laser pulse duration. No K_α pulse duration measurement was performed in this research, while according to the theoretical prediction[], assuming the K_α pulse duration is the order of the laser pulse duration.

The K_α X-ray yield depend on the laser intensity. The slope temperature of electron beam depend on the laser intensity. According to ponderomotive scaling, the electron slope temperature T_h is expressed like below.

$$T_h = m_e c^2 \left(\sqrt{1 + \frac{I\lambda^2}{1.37 \times 10^{18}}} - 1 \right). \tag{2.12}$$

Here, T_h, I, λ is the electron slope temperature, laser intensity in unit of W/cm^2 and laser wavelength in unit of μm, respectively.

In this research, Ti and Cu were used as a backlighter. The K-shell ionization energy of non-ionized Ti is 4.966 keV and that of non-ionized Cu is 8.979 keV. The cross-section of K-shell ionization of Ti and Cu is shown in figure 2.7. The peak value of K-shell ionization cross-section is achieved when the electron kinetic energy is around 20 keV and decreasing until 1 MeV. Due to the dependence on electron energy to the K-shell ionization cross-section, we need proper energy to obtain higher K_α yield.

The experiment was done for estimating the best condition of high-power short-pulse laser. A 20 μm-thickness Ti foil was irradiated by 1.5 ps FWHM, kJ laser. The Ti-k_α yield was measured by RbAp flat crystal and IPs was used as a detector. The intensity of laser was changed by increasing or decreasing the laser spot size. Figure2.8 shows the measured Ti-K_α yield datas according to laser intensity. It is obvious that lower intensity laser generates more K_α photons. That is because the decrease of temperature results in the electron number increase having few tens of keV.

2.2.3 Data interpretation

Figure 2.9 (a) shows the raw data of K_α backlighting image. A square shape emission is the K_α X-ray emitted from the backlighting foil. The shadow of high density plasma shows near

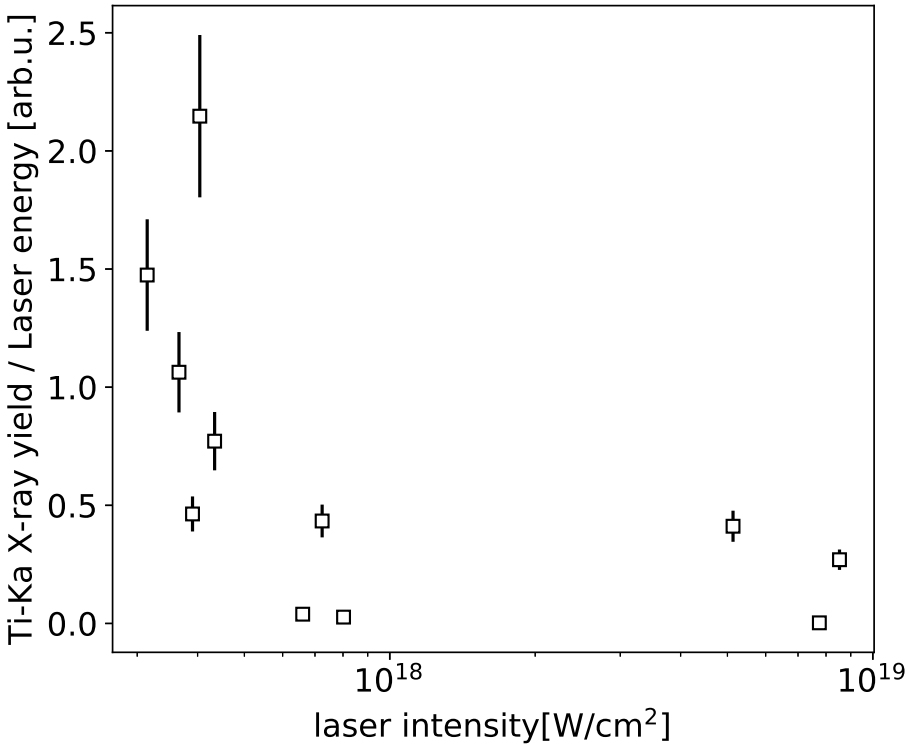

FIGURE 2.8: Laser energy normalized Ti-K_α yield versus the laser intensity. A lower intensity increase the Ti-K_α photon number. This tendency can be explained by the cross-section of K_α emission.

the center of foil. From this data, we can get the transmittance distribution.

Figure 2.9 (b) shows the line out along the red line of Figure 2.9 (a). Captured data is consisted of 3 components : (A) background signal, (B) X-ray emission from the backlighting foil, (C) target shadow. Firstly, (A) should be subtracted. Secondly, fit the (B) without (C) region. In this process, we are assuming the spatial distribution of X-ray without any irregularities. Depending on the spatial pattern of laser, X-ray source may have irregularities which results in the disturbance of accurate analysis of data. To avoid this, the pattern of laser should be carefully adjusted. Te transmittance is then obtained by dividing the background subtracted data with the fitted function. By repeating this process near the target shadow, the transmittance distribution image is obtained.

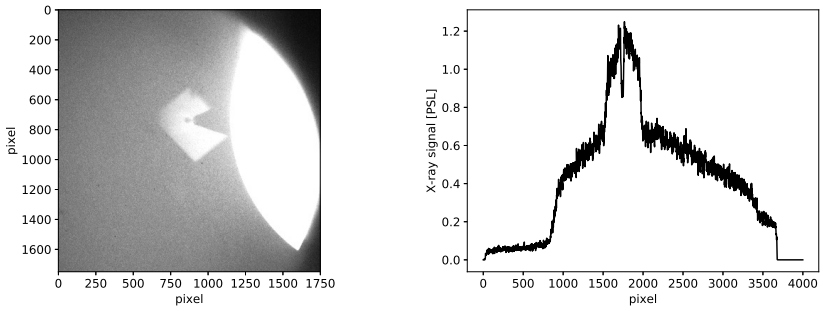

FIGURE 2.9: The image of raw data captured by backlighting method. (a) shows the Raw data image. The Ti-K_α monochromatic image of the foil and the shadow of cone-attached compressed core target is shown. Strong emission place right side of the foil is the direct light from the target consisted of photons in wide-range of photon energy. (b) shows the line out along the dashed line of (a). The data is consisted of background signal, foil emission and the shadows of the target.

Inverse Abel transformation

Due to the plasma has a density distribution along the path of X-ray passed by as showed in Fig. **??**. Inverse Abel transformation process is necessary to obtain the density at a certain point. The transmittance t is defined as $t = \exp(-\mu\rho l)$, where μ, ρ, l is the mass absorption coefficient, mass density and length, respectively. From now, $\mu\rho l$ is defined as optical depth τ. The observed data can be expressed as the integration of optical depth along the observing path as below.

$$t(x) = \exp\left(-2\int_0^{\sqrt{R^2-x^2}} \mu(x,z)\rho(x,z)dz\right), \tag{2.13}$$

$$\log[t(r)] = -\int \mu(r)\rho(r)dz = -2\int_0^R \frac{\mu(r)\rho(r)dr}{\sqrt{r^2-x^2}}. \tag{2.14}$$

Then the optical depth can be derived.

$$\mu(r)\rho(r) = \frac{1}{\pi}\int_0^R \frac{d\ln[\mathrm{t(x)}]}{dx}\frac{dx}{\sqrt{x^2-r^2}} \tag{2.15}$$

The information of the plasma we can get from the backlighting method is optical depth $\mu(r)\rho(r)\Delta L$. We need the distribution of $\mu(r)$ to obtain $\rho(r)$. So, it is necessary to get $\mu(r)$ from the simulation.

It is important to refer here that the inverse Abel transformed transmittance image has no physical meaning. Because inverse Abel transform should be done with the physical values

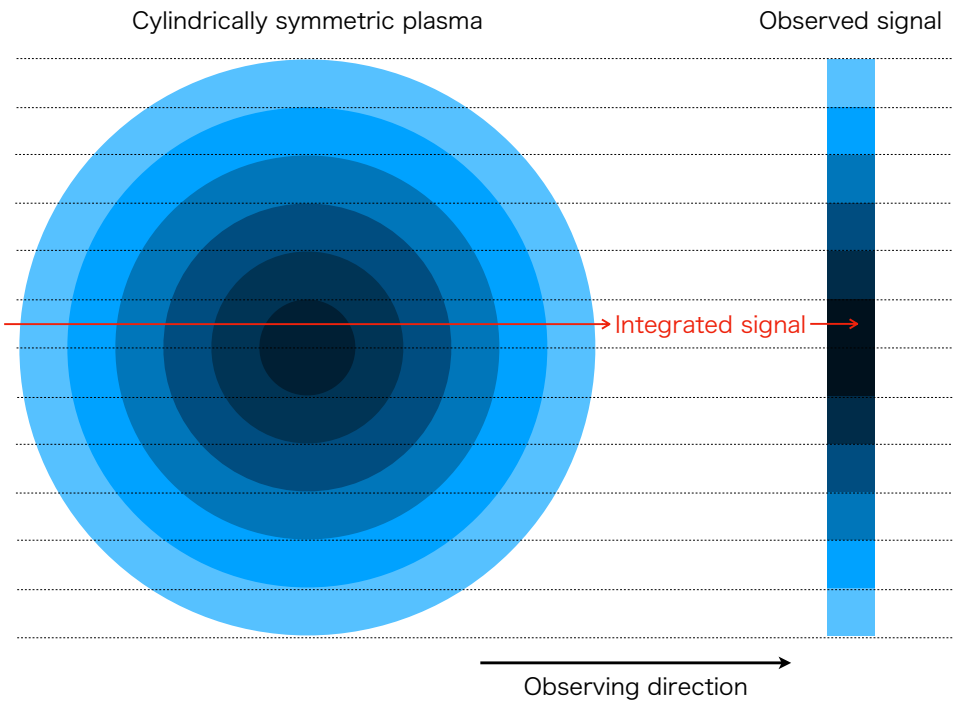

FIGURE 2.10: A measured signal is the integration of plasma emission distributed along the observing direction.

which can be evaluated from the sum of them. By taking $-\ln$ to the values of transmittance image, the distribution of the optical depth can be obtained. The total optical depth can be evaluated by summing all optical depths, so that the inverse Abel transformation is applicable.

Inverse Abel transformation of discrete data

Here, the process of inverse Abel transformation with discrete data is introduced. In cylindrically symmetric system, the image can be assumed to be a set of peaces shown in Fig. 2.11. Only physical parameters which are defined per unit volume, can be used in inverse Abel transformation. Assuming cylindrical symmetric discrete ring-shape plasma, inverse Abel transformation can be simplified using matrix. The observed data I_n can be expressed as follows:

$$I_1 = 2(S_{11}\varepsilon_1 + S_{12}\varepsilon_2 + \ldots + S_{1n}\varepsilon_n) \tag{2.16}$$

$$I_2 = 2(S_{22}\varepsilon_2 + S_{23}\varepsilon_3 + \ldots + S_{2n}\varepsilon_n) \tag{2.17}$$

$$I_n = 2(S_{nn}\varepsilon_n)/d \tag{2.18}$$

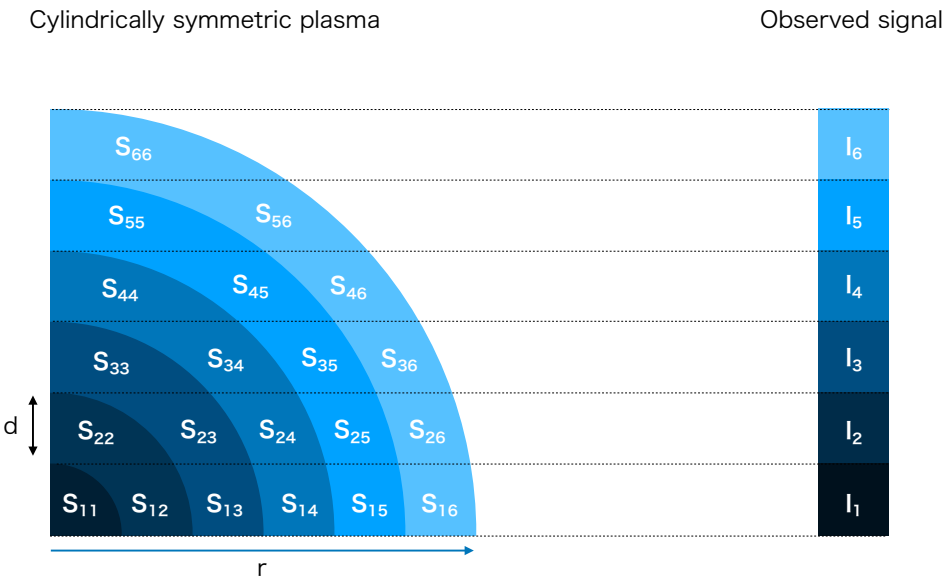

FIGURE 2.11: A image of discrete inverse Abel transformation method.

where ε_j means the local emissivity at the jth radius, S_{ij} is the area of cross position of the ith measurement line and the jth radius. By express these as a matrix, it is simplified as below.

$$[I] = 2[S][\varepsilon] \tag{2.19}$$

S can be calculated as the followings.

$$[\boldsymbol{S}(i,j)] = (i+1)^2 d^2 \left(\cos\left(\frac{i}{i+1}\right)\right)^{-1} - id^2\sqrt{(i+1)^2 - i^2}, \text{(i = j)} \tag{2.20}$$

$$[\boldsymbol{S}(i,j)] = P(i+1,j+1) - P(i,j+1) - P(i+1,j) + P(i,j), \text{(i > j)} \tag{2.21}$$

$$[\boldsymbol{S}(i,j)] = 0, \text{(i < j)} \tag{2.22}$$

$$P(i,j) = i^2 d^2 \sin^{-1}\left(\frac{j}{i}\right) + jd^2\sqrt{i^2 - j^2} \tag{2.23}$$

Thus, the actual distribution of a physical parameter ε is then can be calculated as the following.

$$[\varepsilon] = \frac{1}{2}[S]^{-1}[I] \tag{2.24}$$

Here $[S]^{-1}$ is the inverse matrix. Now the inverse Abel transformation of discrete data can be easily done.

2.3 X-ray Streak Camera

2.3.1 The operating principle of X-ray streak camera

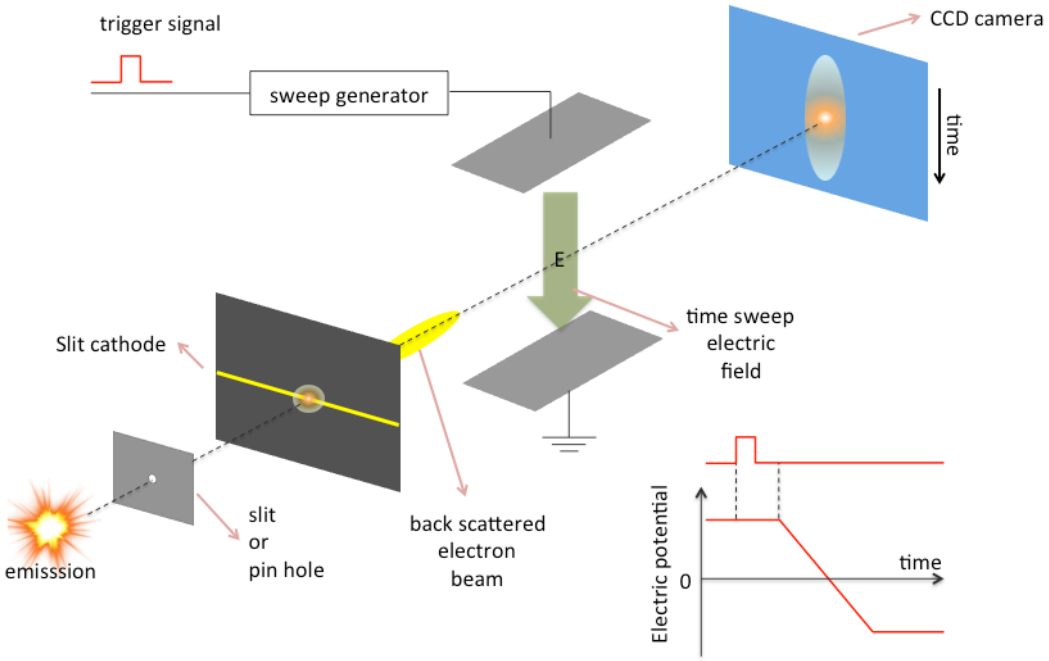

FIGURE 2.12: The principle of X-ray streak camera.

The X-rays emitted from the target is imaged on a photocathode film via an imaging device like a slit or a pinhole. By the collisions of X-rays with the electrons in photocathode, first-scattered electrons are generated. The energy of the first-scattered electrons is determined by the photon energy of X-ray. The first-scattered electrons are collide with other electrons inside the photocathode and generate low energy electrons. It is called the secondary-scattered electron, which is an electron that actually becomes an image. The higher the energy of the first-scattered electrons, the greater the number of secondary-scattered electrons. The secondary-scattered electrons have much lower energy than the first-scattered electrons. Due to the energy distribution results in the degrading of temporal resolution, few tens of kV electric fields are applied to accelerate whole electrons.

After the secondary-scattered electrons are accelerated by the electrode and the temporally changing X-ray signal is spatially separated by the temporally changing electric field. The number of secondary-backscattered electrons is increased by the Multi Channel Plate(MCP) electron multiplier. Spatially separated electrons are converted into a visible light on the fluorescent screen and it is detected by the CCD camera.

Photo electron generation[16]

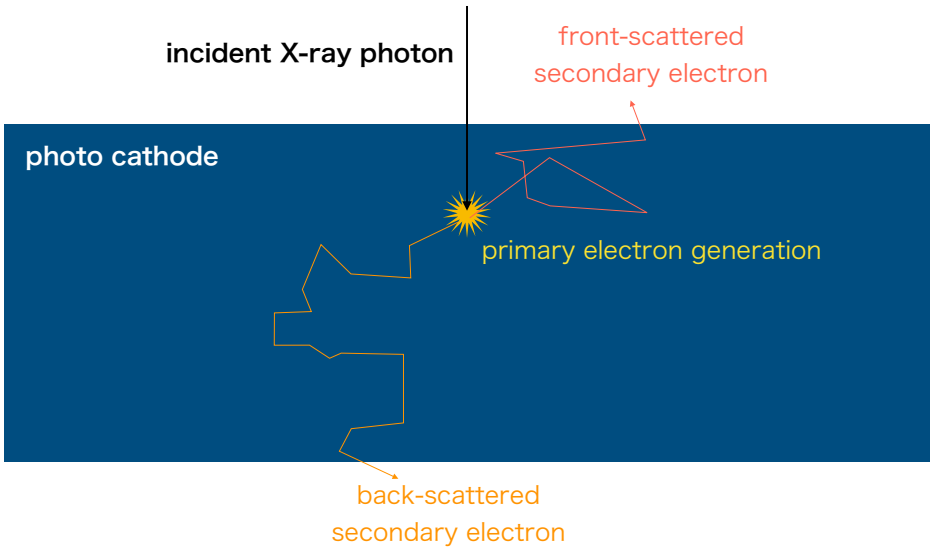

FIGURE 2.13: The process of large number of electrons generation. The irradiated X-ray photon generate the primary electron inside the photo cathode. The primary electron generated by X-ray have energy almost equal to the X-ray photon energy. This electron collide with the electrons inside the photocathode, and results in the large number of secondary elecrrons. The secondary electrons radiated to the front and the rear side of the photocathode.

The X-ray photon is converted to the electron inside the photo cathode. The large fraction of electron generation image is shown in Fig. 2.13 When the X-ray photon is irradiated to the photo cathode, the primary electrons are kicked out by the X-ray photon. The kinetic energy of primary electron is almost same as the X-ray photon energy. The number of primary electron is same as the X-ray photon number. The primary electron then collide inside the photo cathode. By the collisions of primary electron, secondary electrons are generated. The energy of secondary electrons are much lower than the primary electron. Typically, the secondary electron energy is less than 5 eV while the primary electron energy is almost same as X-ray photon

energy, i.e., 1 keV as shown in Fig. 2.14. The number fraction of secondary electron is much larger than the primary electron.

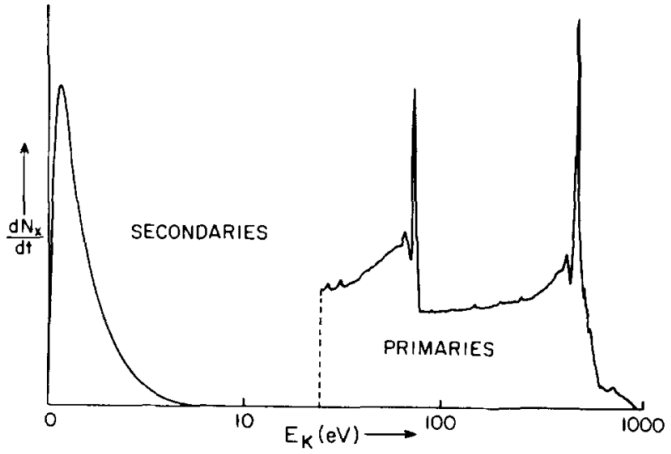

FIGURE 2.14: The larger fraction of the secondary electrons are generated. typically as a narrow distribution having a peak value below 10 eV. The higher energy primary photo electron consists of sharp elastic scattering component and Auger electrons which revealed as the low energy tail of sharp one.

Back-scattered secondary electron acceleration for reducing the arrival time difference[16]

Due to low kinetic energy and its distribution, slower electron arrive later than the fast one to the detector. This makes the temporal resolution degrade. To solve this problem, strong electric field is applied backside of the photo cathode to accelerate the back-scattered secondary electrons. Because the distance from the cathode to the detector is constant, the arrival time difference is getting lower if the kinetic energy is higher. The temporal resolution τ is then,

$$\tau = 3.37S\frac{\Delta^{0.5}}{V_0}\left[1+\frac{1}{4}\left(\frac{L}{S}-2\right)\left(\frac{\Delta}{eV_0}\right)^{0.5}\right] \tag{2.25}$$

Here Δ, V_0, L, S, e is the energy spread of secondary electron, the extracted electric potential, the traveling distance without electric potential, the traveling distance with electric potential and the electric charge, respectively. For example, when the secondary electron energy spread is 2 eV, and the extraction potential V_0 of 5 kV and the the distance S of 1mm, the temporal resolution τ will be 1 ps.

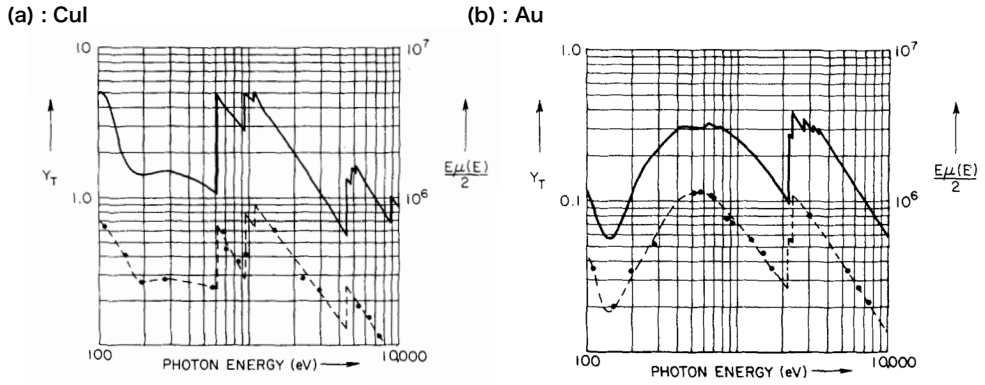

FIGURE 2.15: (a) The quantum yield for 1100 Åthick CuI photocathode. (b) The quantum yield for 300 Åthick Au photo cathode.

Photocathode material

In this research, the CuI photocathode was used. The plasma temperature in our experiment is expected to be 1-10 keV. According to black body radiation, $h\nu = 2.822 k_B T$ which means that the plasma temperature 1-10 keV generates mainly 2.822-28.22 keV X-rays. The laser generated plasma does not emits black body radiation for all X-ray energy region because the thickness of the plasma may opaque to the high energy X-rays. This makes the photon energy having peak emission intensity moves to the lower photon energy. But it can be said that the few keV X-ray have the most emittance for laser generated plasma. Fig. 2.15 shows the quantum yield of two-kinds of photocathode. As you can see, the CuI photocathode have 10 times higher quantum yield for 0.1 - 10 keV photon energy, than the Au photocathode. The higher signal can be obtained by using CuI. The CuI must be stored in the vacuum environment. Because the CuI is soluble in water, moisture of the atmosphere. The quantum yield decreases and/or the spatial unevenness makes the image degrade.

2.3.2 Temporal resolution of X-ray streak camera

The temporal change of the light source is spatially separated by the time-varying sweep electrode in the streak tube and observed in the time sweep direction on the fluorescent screen. The time resolution of the streak camera is determined by the spread in the time direction of the electron group that has reached the phosphor screen. The factors that determine the time resolution are explained below.

Electron transit time spread by initial velocity distribution of photoelectrons Δt_1

Photoelectrons on the photoelectric surface have angular distribution and velocity distribution. When photoelectrons traveling in the streak tube, those are spatially distributed to the velocity direction. This causes a time difference until the photoelectrons are accelerated by the accelerating mesh and arrive at the deflection electric field, which spreads the position on the fluorescent surface, that is time spread in the image. This time spread is

$$\Delta t_1 = 2.34 \times 10^{-6} \frac{\sqrt{\Delta\varepsilon}}{E} \tag{2.26}$$

Here, E is the acceleration electric field strength. $\Delta\varepsilon$ Is the full width at half maximum of the photoelectron energy distribution in the direction of the streak tube axis. The $\Delta\varepsilon$ is 3.5 eV, and the the accelerating electric field E of the X-ray streak camera (C7700) is 1.6×10^6 V / m. Then Δt_1 = 2.9 ps.

Time spread with finite spatial resolution Δt_2

The beam diameter of photoelectrons in the streak tube has a finite diameter. Even electron beams incident on deflection field at the same time the potential is different above and below (with respect to the deflection electric field). As a result, a travel time difference occurs, and this time spread Δt_2 Is expressed by the following.

$$\Delta t_2 = \frac{PV_dR}{v_cV_cD}. \tag{2.27}$$

Here, P is the length of the deflection electrode [m], Vd is the potential of the deflection electrode [V], R is the radius of the photoelectron beam [m], vc is the electron velocity corresponding to the acceleration voltage [m / s], Vc Is the acceleration voltage [V], and D is the distance [m] of the deflection electrode. In our XSC, $3.5 \times 10^{-2}, V_d = 243V, R = 1.0 \times 10^{-3}, V_c = 8.0kV, v_c = 5.3 \times 10^7 m/s, D = 8.7 \times 10^{-3} m$, so that $\Delta t_2 = 2.3ps$.

Time spread with finite spatial resolution Δt_3

When measurement is performed in the stationary mode of the streak camera with the sampling mask attached in front of the photo camera, a point image having a finite diameter can be obtained on the photocathode. This is the input pinhole image of the sampling mask, and the full width at half maximum affects the time resolution of the streak camera. The pinhole diameter in the sweep direction is the width that constitutes a streak image, and the sweep time

corresponding to this width limits the time resolution. Therefore, the time expansion (t 3 [s]) due to the spatial resolution is expressed by equation (3.23).

$$\Delta t_3 = d_p \times v. \tag{2.28}$$

Here, d_p is the sampling pinhole diameter [pixel] taking into consideration the point spread of the streak camera, and v is the sweep time [ps / pixel]. In the setup of this system, d_p = 5 pixel and v = 9.8 ps / pixel. Then Δt_3 = 49.0 ps.

Time resolution of the system Δt_{tot}

The time spread determined by the above three factors is considered to be independent of each other. Assuming that each spread is Gaussian, the overall time spread, that is, the time resolution is given by the square root of the sum of squares of three elements, and is expressed by the following.

$$\Delta t_{\mathrm{tot}} = \sqrt{\Delta t_1^2 + \Delta t_2^2 + \Delta t_3^2} \tag{2.29}$$

So the total temporal resolution Δt_{tot} in this system is to be 49.1 ps.

2.3.3 Timing measurement between compression laser and heating laser

A laser for fuel compression have nano-second pulse duration with maximum intensity of 10^{15} W/cm^2. Another laser for heating the compressed fuel have pico-second pulse duration with maximum intensity of 10^{19} W/cm^2. On target, on shot timing measurement between these two kinds of lasers is important. Due to the maximum compression maintaining less than 100 ps, heating should be done in accurate timing. A few keV X-ray signal is measured for chasing the laser irradiation timing. The X-ray intensity emitted by the interaction between heating laser and plasma is far beyond that the X-ray intensity due to compression laser. We have developed on shot, on target timing diagnosis to measure the timing between two types of lasers with 4 digit intensity difference.

Installing the hard X-ray shield, the timing between the compression laser and the heating laser can be measurable with high temporal accuracy. A hard X-ray is generated when short pulse high intensity laser is irradiated. The hard X-ray transmit the pinhole disc because its photon energy is too large (> 100 keV) for attenuating the hard X-ray. Thus we call this hard X-ray as a non-imaged hard X-ray. Non-imaged hard X-rays attenuated by the thick W shield placed right in front of the cathode and only near the window for cathode slit, remains. In streaked image, the signal of non-imaged hard X-ray is a shape of window. Since non-imaged

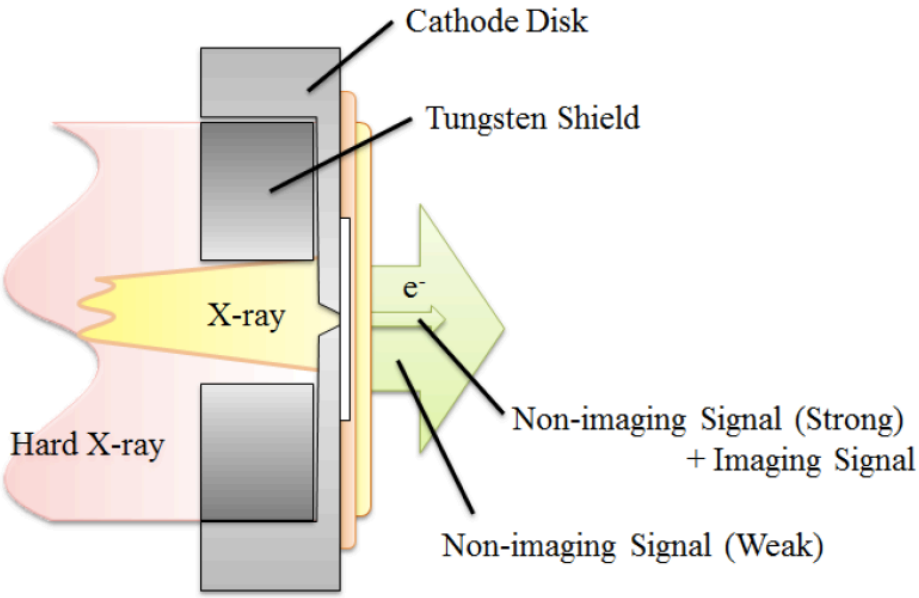

FIGURE 2.16: The schematic of hard X-ray timing measurement. A thick high-Z material (here we used Tungsten) is placed right before the photocathode slit. The X-ray image, which is imaged by the imager like pinhole of slit or the bent mirror is only recorded inside the slit. While the hard X-ray signal (its energy was estimated to be > 100 keV from the attenuation of signal) can penetrate the imaging disk and also the cathode disk. They generate high energy electrons by colliding with the photocathode with same size of tungsten shield. Those are finally detected to the CCD camera. Due to the pulse duration of hard X-ray is short enough (1 ps) than the temporal resolution of the XSC, the flash band signal appears on the imaged thermal X-ray. The peak intensity position is the hard X-ray timing, which is correspond to the high-power short-pulse laser irradiation timing.

hard X-rays are also short pulse as LFEX (1ps), which is much smaller than the temporal resolution of XSC. Thus, a snap shot of the window is observed with imaged X-ray signal generated by nano-second laser. By comparing the imaged X-ray signal and the instantaneous strapped signal, we can measure the timing of nano-second laser and the pico-second laser with 4 digit intensity difference.

Chapter 3

High density plasma generation using solid fusion fuel

3.1 Introduction on solid target

In FI, the compression process and heating process is separated. From the beginning of the FI experiment, only shell target was used for generate high density plasma. As explained in Chapter 1, many techniques should be used for compress shell target. Go back to the role of the shell target, it was adapted for generating a hot spot with moderate laser intensity. While in FI, hot spot does not generated during the compression process, but generated by the heating process with high-intensity pico-second laser pulse generated charged particles. This means that using shell target is not required.

Here a solid target is suggested for a new target shape for FI. The shell target is directly accelerated by the ablation pressure and accelerated. While the solid target is not accelerated but shock waves are driven inside the target. That shock wave accelerate particles to the target center. The critical point for using solid target is that the solid target is compressed by the shock wave. A shock wave is well-known self-stabilizing hydrodynamic phenomena. Even it has a initial perturbation on the shock surface, those are smoothed by the ion acoustic waves at the post-shocked region. A stability of converging spherical shock wave has been studied and briefly introduced here.

3.1.1 Stability of converging spherical shock wave

The most famous stability analysis is done by Chester, Chisnell and Whitham, and this theory is called CCW theory[4, 5, 53]. In this theory, the relative perturbation amplitude which is defined as the perturbation amplitude divided by the shock front radius, is constant for all spherical harmonics mode. The most recent analysis suggested that the stability of the shock wave depends

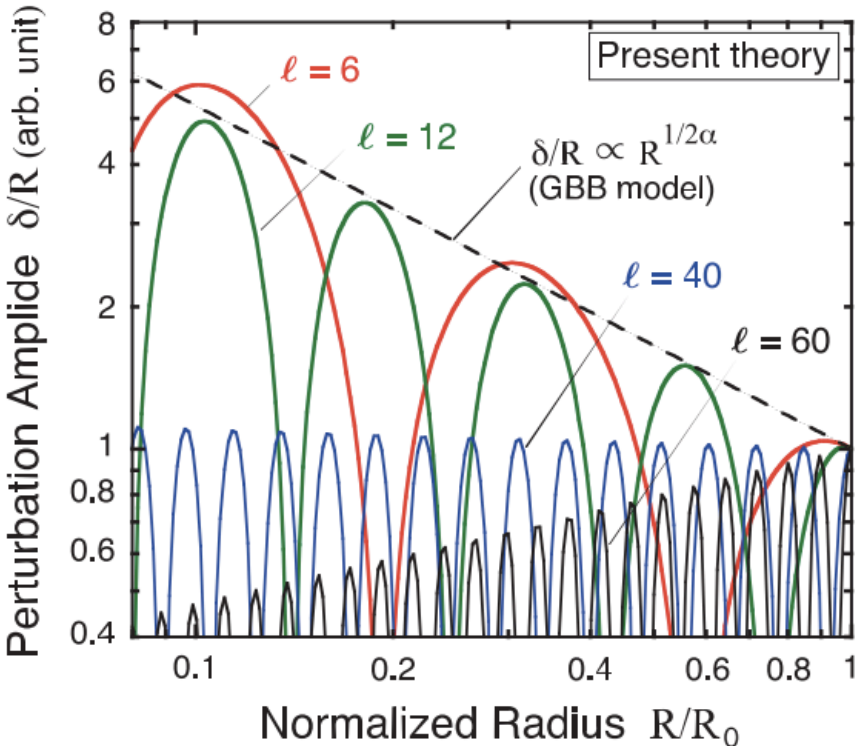

FIGURE 3.1: Evolutions of the normalized perturbation amplitude δ/R for different mode numbers for ideal gas($\gamma = 5/3$) for converging spherical shock wave. The initial amplitude is set to be unity at $R/R_0 = 1$. The CCW theory(GBB model) is shown as dashed line.

on the shock wave perturbation spherical harmonics mode[31]. The evolutions of converging spherical shock wave perturbation is shown in Fig. **??**. One can understand that the shock wave converges by oscillating. A low mode shock wave oscillate slower than the high mode shock wave. A low mode shock wave have longer wavelength than the high mode shock wave, which results in longer time delay to transmit the information of pressure perturbation. The CCW theory is plotted as a dashed line. In the CCW theory, it is assumed that the shock front does not affected by the post-shocked medium. With that approximation, the relative perturbation amplitude is increasing proportional to the $R^{-0.5}$. Here it is important that the relative perturbation is growing by converging while, the absolute perturbation amplitude is getting smaller because $\delta/R \propto R^{-0.5}$ then $\delta \propto R^{0.5}$. By converging, R is getting smaller and smaller which means the perturbation amplitude is also getting smaller and smaller. In recent theory, Murakami, et. al., took account the effect of the supersonic region in the post-shocked medium. Due to supersonic region does not perturbed because those are faster than any other point of neighborhood thus, they can smear out the perturbation having wavelength shorter than the distance between the

shock front and the sonic surface. Thus, for higher mode shock wave perturbation, the growth rate is much smaller than CCW predicted values.

Compare to the RTI, there is no positive feedback loop for increasing the perturbation amplitude. Which means that the shock wave is much more stable than the shell converging case. Thus, we suggested solid target and performed an experiment for compressing the shell and solid fuel and measured the density of compressed fuel.

3.2 Solid fuel compression using Gaussian laser pulse

3.2.1 Experimental conditions

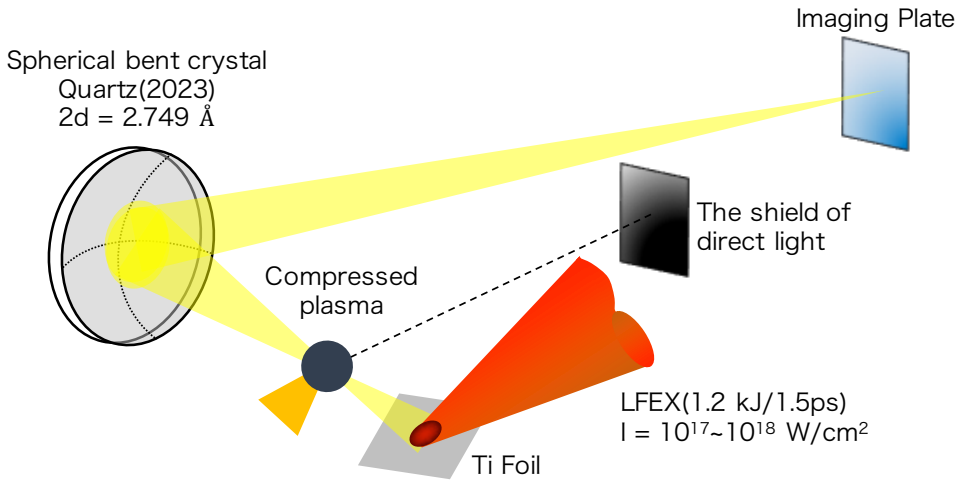

FIGURE 3.2: The experiment layout. Ti foil is place 2 mm away from the target to the direction of along the line of crystal-target. Near the maximum compression timing, the Ti foil is irradiated by the LFEX laser. Flash Ti-K_α X-rays are generated isotropically. The 2 cm thick Tungsten(W) shield is placed to shield the self emission on imaging plate side but not to shield the Ti-K_α X-ray image.

The experiment was performed at Institute of Laser Engineering using the GXII nano-second laser[55] and LFEX pico-second laser. A 200 μm diameter solid CD fuel with Au cone was irradiated by 9 GXII beams having 527 nm wavelength. The total energy of lasers is 2.7 kJ (300J/beam) having 1.3 ns FWHM Gaussian pulse duration. The density of compressed fuel was measured by flash K_α X-ray backlighting method as showed in Fig. 3.2. Around the peak compression timing, the Ti foil placed 2 mm away from the target is irradiated by LFEX laser and it emits high intensity Ti-K_α (4.51 keV) emission. Emitted Ti-K_α X-rays passed through

the compressed target. Attenuated Ti-K_α X-ray is imaged by the spherically bent crystal and the image was detected by the BAS-SR IPs[42]. The imager had a 11.5 magnification and 5 eV spectral resolution. The spatial resolution is 12.5 μm which is estimated by the shadow of gold cone. Due to LFEX laser have 1.5 ps pulse duration, hydrodynamic resolution degrading can be negligible.

3.2.2 Result and discussion

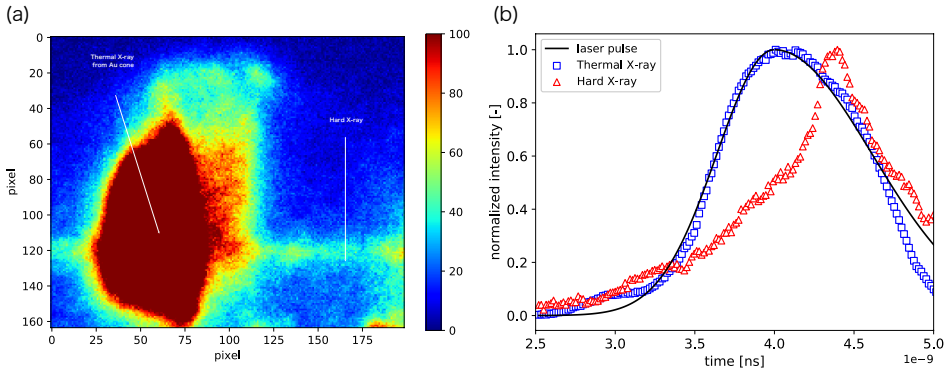

FIGURE 3.3: The image of temporal evolution of X-ray emission image measured by XSC. (a) shows the Raw data XSC image. Horizontal line recorded spatial distribution and vertical line recorded temporal evolution. (b) shows the line outs. Red square dots shows the temporal evolution of 2-5 keV thermal X-rays. Blue triangle dots shows the hard X-ray. The spread of hard X-ray to the time direction is caused by the finite width of thick Tungsten window.

The relative timing of the backlighter Ti-K_α X-ray with respect to the compression lasers was measured by XSC[45, 46, 22]. Fig. 3.3 shows the measured XSC image and line outs. The image of 2-5 keV thermal X-rays emission generated by the interactions between GXII(nano-second laser) and fuel plasma was recorded using XSC. Therefore, the temporal evolution of thermal X-rays can be assumed to be the laser pulse shape. The timing of the LFEX was determined by matching the leading edge of the thermal X-ray emission profile to the laser profile. Here, the peak timing of GXII was chosen to be 4.0 ns. The timing error is $\pm$ 42 ps which was discussed in Chap.2.

Fig. 3.4 shows obtained backlighting raw images. The formation process of high density plasma was observed. At 4.11 ns, the fuel size is half of the non-driven image. At 4.17 ns, the fuel is compressed more than that of 4.11 ns and there is triangle shape shadow of the dense

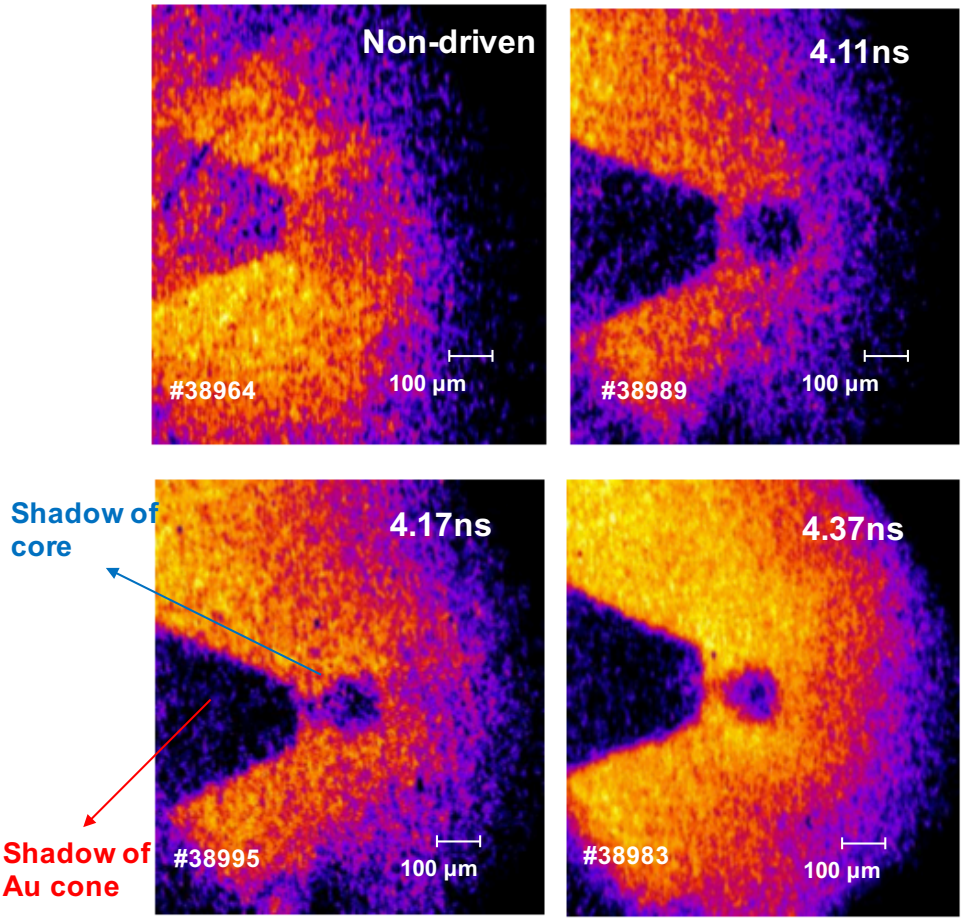

FIGURE 3.4: The radiography image measured by backlighting imager.

region. The triangle shape core plasma is due to the non-symmetric compression. 9 beams without 3 beams placed around the gold cone were irradiated, the pressure of opposite side of gold cone is higher than that of gold cone side. The shock waves collided at 4.37 ns so that small shadow was observed. By interpreting the data, transmittance images and inverse Abel transformed optical depth images were produced as shows in Fig. 3.5.

The solid sphere compression was simulated with a two-dimensional radiation hydrodynamic simulation code RAICHO[35] using the experimental laser parameters and target specification. Numerical scheme of RAICHO is based on the finite volume method with an Eulerian mesh. Absorption of laser energy is calculated via inverse bremsstrahlung with one-dimensional ray-tracing over the radial direction. Radiative transport and heat transfer equation are using a flux limiting model (f = 0.06) and ignoring nonlocal effects. The target opacity is included using tabular data calculated by an average ion model assuming collisional radiative equlibrium. High

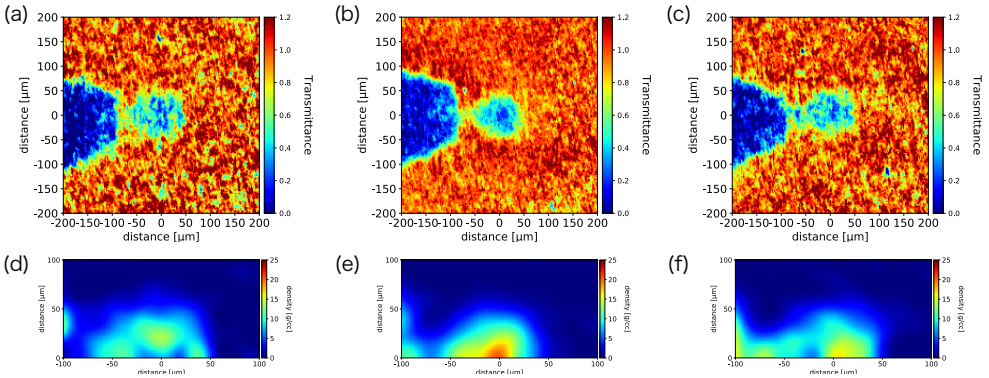

FIGURE 3.5: The image of temporal evolution of plasma transmittance and the inverse Abel transformed optical depth distribution. (a) (c) (e) shows the temporal evolutions of the transmittance. (b) (d) (e) shows the temporal evolution of optical depth.

density plasma equation of state was constructed by the theory developed by More et al[29].

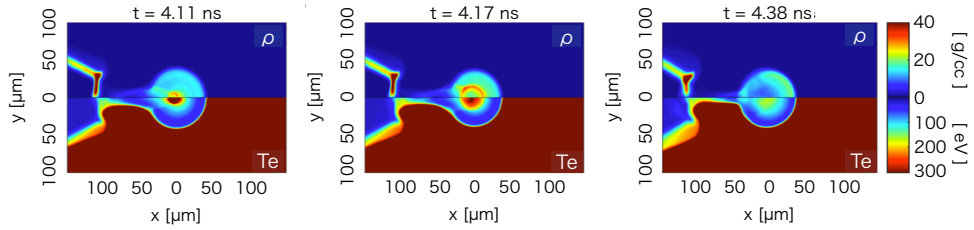

FIGURE 3.6: An areal densities and a temperatures calculation result at the timing of experiment. The radiation hydrodynamic simulations were performed in two-dimensional cylindrical geometry for cone attached solid fuel compression.

Figure 3.6 shows simulated two-dimensional mass density and temperature contour map smoothed at experimental resolution. The variation in temperature and density of the azimuthal mean radial profile of the core is used to estimate the variation of the calculated mass attenuation coefficient. The mean value of the mass attenuation coefficients is 21 $\pm$ 3 cm^2/g with the electron density uncertainty of 100 - 300 eV. The simulated areal density was calculated by integrating the density in perpendicular direction to the cone. The sphere compression was also calculated with one-dimensional radiation hydrodynamic simulation code, Helios[27]. The maximum compression timing of 2D simulation result is delayed compare to 1D case. This is because in asymmetric compression, since the pressure of the shock wave flows to the side where the laser is not irradiated, the pressure of the shock wave decreases. Due to the shock wave propagates with almost the sound velocity expressed as below, decrease of shock pressure

result in the decrease of the shock speed.

$$c_s = \sqrt{\frac{\gamma p}{\rho}} \tag{3.1}$$

Here, γ, p, ρ is the heat capacity ratio, pressure of shock wave and mass density of non-shocked material, respectively. The shock pressure decrease results in the decrease of maximum compression rate. The target preheating caused by strong radiation from Au cone is also affect the decrease of the compression rate. The high energy X-rays caused by the interaction between laser and Au plasma, deposit their energy to the non-shocked fuel region. This results in the increase of the non-shocked fuel pressure. The compression rate due to shock wave is defined by the pressure ratio between non-shocked fuel and shock wave. The increase of pressure of non-shocked fuel decrease the compression rate of the shock wave.

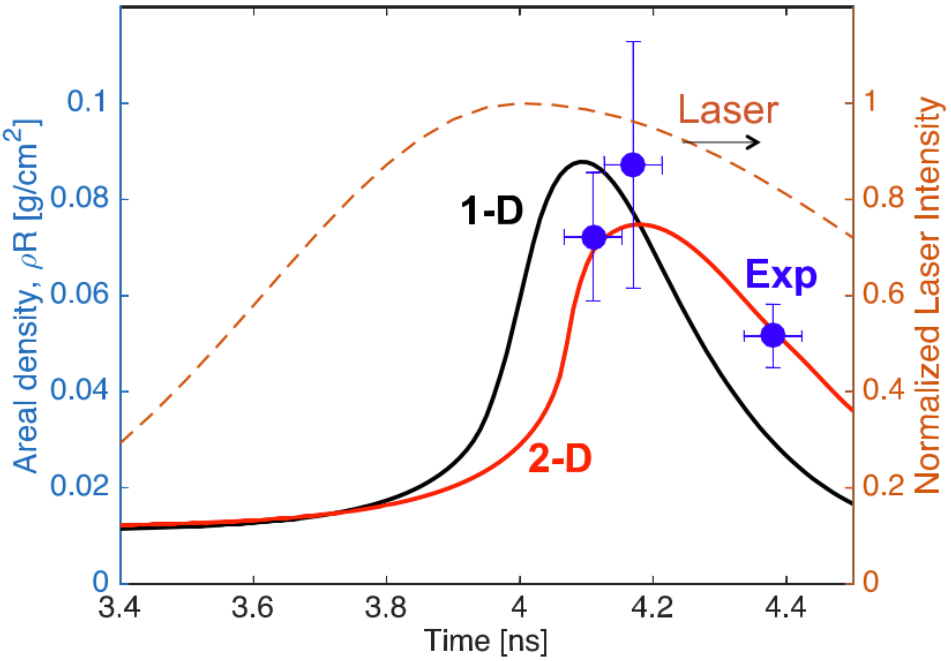

FIGURE 3.7: A comparison of the experimentally measured areal density and calculated areal density. The radiation hydrodynamic simulations were performed in two-dimensional cylindrical geometry for cone attached solid fuel compression. The one-dimensional calculation was also done.

Fig. 3.7 shows the temporal evolution of areal density of simulated results compared with

the experimental data. The experimental results agree with the 2D calculation results. The uncertainties are evaluated from the background subtraction and the extrapolating Ti-K_α emission distribution.

In conclusion, the process of solid fuel compression is measured by flash K_α imaging techniques. In this experiment, no laser intensity distribution smoothing techniques was used. The laser irradiation condition of d/R = -3 were used for all experiment. It is obvious that the intensity distribution have large perturbation on the surface of the fuel. Figure 3.15 shows the spatial distribution of pressure in the laser irradiation condition of d/R = -3. In shell compression experiment, no shadow of the core was measured in this laser condition. The solid fuel compression showed the stability in high density fuel generation. The arial density of the fuel in this experiment is 0.05 g/cm^2. As mentioned before, more than 0.3 g/cm^2 of areal density is required for realization of ignition condition.

The compression rate due to the shock wave is limited by the Rankine-Hugoniot relation.

$$\tilde{\rho} = \frac{(\gamma+1)\tilde{p}+(\gamma-1)}{(\gamma-1)\tilde{p}+(\gamma+1)} \tag{3.2}$$

For γ = 5/3, p = ∞, the compression rate ρ is 4. Only 4 times compression is possible in planar geometry. Spherically converging shock wave have more compression rate due to the decrease of the volume of shocked region as converging. Gudderley, et al. shows the 36 times compression of ideal gas using single strong converging shock wave by self-similar analysis. Thus 36 times compression is then the theoretical limits of solid ball compression using single strong shock wave. The experimentally measured maximum density is 52.5 $\pm$ 7.5 g/cc which is larger than 36 times of initial density (1.0 g/cc). This is because the 0.9 ns of Gaussian rising laser pulse generated not only one strong shock wave, but also some weak shock waves which is preceding the main shock wave. Preceding shock waves firstly compress the fuel with small compression rate and the main strong shock wave compress the pre-compressed fuel. The entropy increasing of this process is lower than the single strong shock compression process.

3.3 Adiabatic compression method of solid fusion fuel using tailored laser pulse

As discuss before, the compression rate of strong shock wave is limited by the Rankine-Hugoniot relation. A high density compression by multi-weak-shock waves was introduced to compress the fuel adiabatically using laser. Adiabatic compression rate is not limited physically compare

to shock compression. Thus we can get much higher compression rate by the adiabatic compression method. Adiabatic compression by the laser was introduced from the beginning of the ICF researches. Here the heuristic compression idea and the preliminary experiment on solid fuel compression using tailored laser pulse will be shown.

Here a fundamental idea for adiabatic compression of the sphere will be introduced[20]. The simplest case of adiabatic compression is homogeneous adiabatic compression, i.e. an adiabatic compression in which every volume element is compressed with same compression rate. An important property of an adiabatic compression is that maximum compression is achieved with an applied pressure. Kidder suggest the analytical form of the pulse shape by the following.

$$\frac{I}{I_0} = \left(\frac{R_0}{R}\right)^2 (1-\tau^2)^{-11/4} \tag{3.3}$$

3.3.1 Compression by the tailored laser pulse

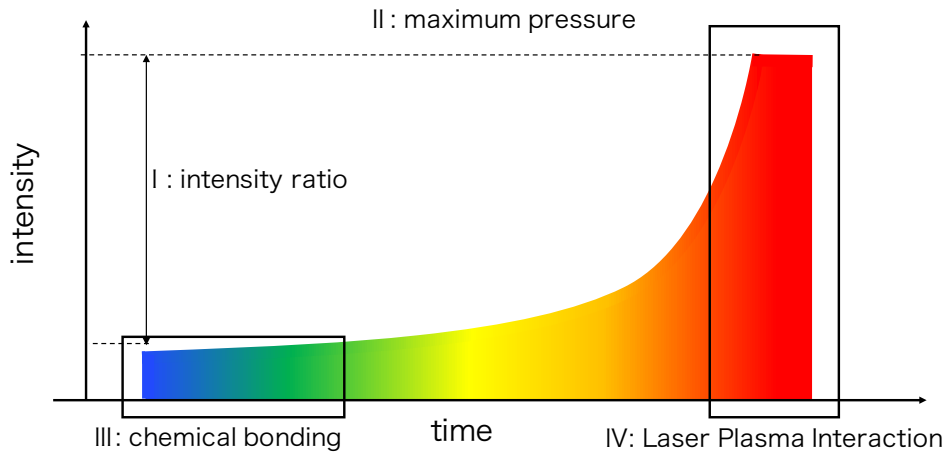

FIGURE 3.8: A physical issues on tailored laser pulse. I : the higher intensity ratio is required for increasing the compression ratio. II : the higher maximum intensity is required for increasing the compression ratio because of the Fermi pressure increase. III : the chemical bonding issue should be studied at low-pressure shock wave and matter interaction. IV : when the laser intensity is higher than 10^{14} W/cm^2, the laser plasma instabilities occur which results in degrading the laser absorption and preheating the plasma.

In reality, the laser pulse should be designed by considering many physical issues shown in Fig. 3.8.

Firstly, the intensity ratio of initial laser intensity to the final laser intensity is important. In adiabatic compression, total pressure compression ratio is proportional to the density compression ratio.

$$\tilde{p} \propto \tilde{\rho}^{\gamma} \tag{3.4}$$

The γ is usually assumed 5/3 as an ideal monotonic gas in high energy density physics. The shock wave generated at low intensity region, the increase of the temperature due to the first shock wave is less than 1 eV. Which means that the 5/3 of γ value cannot be used anymore. Due to the chemical bonding effect, a low temperature and solid density plasma pressure is much lower than that of ideal gas. This makes the first shock wave slower than the ideal gas case, it degrade the compression ratio.

Second, the maximum laser intensity is also important. Due to the Fermi pressure is proportional to the 5/3 power of the mass density, It is increased as compression goes by. As an example, the Fermi pressure of solid density parylene plastic is 4 Mbar. To compress the parylene plastic, more than 4 Mbar pressure is needed. In same sense, 100 times compressed parylene plasma have Fermi pressure is 8 Gbar. To compress this matter, more than 8 Gbar pressure shock wave should be drived. The ablation pressure generated by 10^{15} W/cm^2 laser intensity is only 100 Mbar. This value is much smaller than the Fermi pressure of 100 times compressed parylene. The effect of converging makes this pressure increase. The shock pressure increase with proportional to the r_0/r_s, here r_0 is the initial fuel radius and r_s is the shock front radius. When the shock front radius is $1/80$ of the initial radius, the pressure can be increased to 8 Gbar.

Ideally, the converging shock pressure increase to the infinity, however in reality, it is not. That is because of the existence of the pressure perturbation. The pressure perturbation limits the size of the core plasma. When the perturbation depth exceed the shock front radius, shock wave is collapsed and generate outward shock wave. The shock front perturbation is induced by the spatial non-uniformity of laser intensity at the surface of the fuel. Spatial smoothing technique should be used for reducing the shock front perturbation.

If we increase the laser intensity higher than 10^15 W/cm^2, the laser plasma instabilities grows faster. The laser plasma instabilities degrade the laser absorption and generate non-thermal hot electrons. These phenomena is complicated that analytical design is impossible. These physical issues should be considered when pulse shape designing.

3.3.2 Laser pulse design using one-dimensional radiation hydrodynamic simulation

As mentioned before, theoretically designed laser pulse is not applicable in experiment. Many physical issues should be considered : a EOS of low temperature state and a non-thermal hot electrons generated by laser plasma instabilities. One-dimensional radiation hydrodynamic simulation code was performed. A EOS of low temperature plasma is considered, especially the chemical-bonding is considered that the shock velocity of initial shock waves can be estimated accurately. As the target, 1.3 mm diameter DT ice target was compressed by the laser showed as blue curve in Fig. 3.9. The maximum laser intensity is 10^{15}W/cm^2 with wavelength of 351 nm. The maximum areal density ρR of compressed core is 1.4 g/cm^2 which is much higher than the areal density for ignition. Also, only 50 kJ laser energy was used for this calculation. Due to the adiabatic compression keeps the plasma pressure minimum at that time, the input energy is also minimized compare to strong shock wave compression or shell compression.

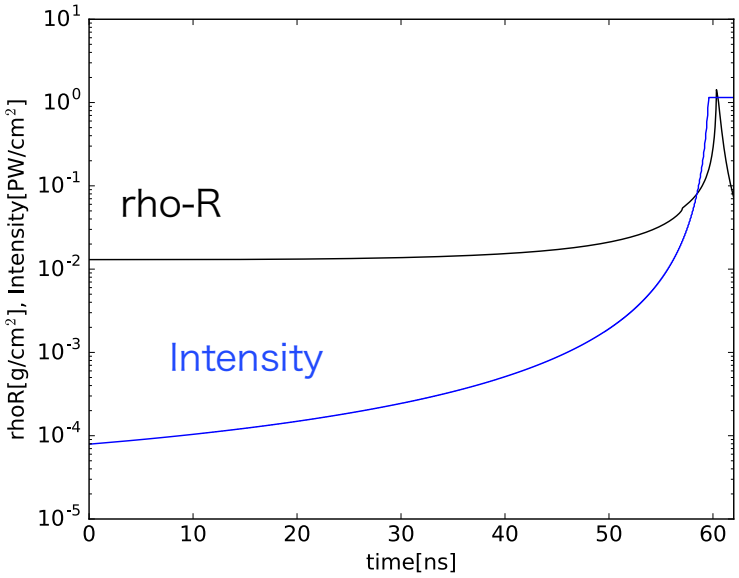

FIGURE 3.9: The temporal evolution of ρR of the compressed fuel and the laser profile. 1D radiation hydrodynamic simulation code was used for this calculation.

3.4 Adiabatic compression experiment of solid fusion fuel using tailored laser pulse

3.4.1 Laser pulse tailoring with fiber oscillator

A pressure tailoring is required to achieve adiabatic solid fuel compression. A fiber oscillator was installed to the GXII system to shaping the laser pulse. The fiber laser uses an optical fiber as the active medium, which usually has a rare-earth doped core. Using fiber oscillator, an arbitrary pulse shape laser pulse can be generated. In this system, 1/1000 of intensity ratio between the initial intensity and the maximum intensity is achievable. At the stage of the laser energy amplification, the intensity ratio increases to $1/1000^2$ due to the energy gain is proportional to the square of the laser intensity in low intensity region.

3.4.2 Experiment on solid fuel compression using tailored laser pulse

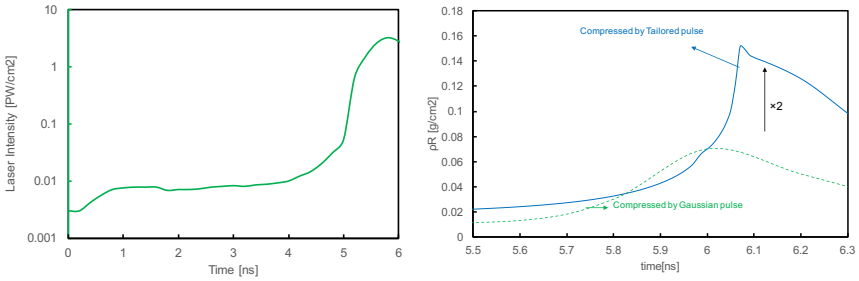

FIGURE 3.10: A measured 527 nm laser pulse shape. 1/1000 intensity ratio is achievable in this system. The expected areal density is plotted as blue solid line. The green dotted line shows the compression by the Gaussian laser pulse. The one-dimensional radiation hydrodynamic simulation code was used.

The solid fuel compression experiment was done with the laser pulse showed in Fig. 3.10(a) having 527 nm wavelength. The 200μm CD sphere was compressed by 12 laser beams symmetrically with laser irradiation condition of d/R = -3. And the expected fuel density was estimated using one dimensional radiation hydrodynamic code. Fig. 3.10 (b) shows the calculated areal density. Green dashed line shows the temporal evolution of fuel areal density compressed by Gaussian laser pulse. Blue solid line shows the temporal evolution of fuel areal density compressed by the tailored laser pulse. 1.8 times larger areal density plasma formation is expected.

The flash K_α X-ray backlighting was used to measure the density of the plasma. Captured radiography image shows in Fig. 3.11. The shape of the core was no more a round shape but an

uneven shape. The timing of the flash K_α X-ray was at 4.5 ns. The timing is defined according to the time axis of Fig. 3.10. The uneven core shape at 1.3 ns before the maximum laser intensity timing indicates that the presence of shock wave perturbation. The inverse Abel transformation does not performed to this plasma because we cannot assume axial-symmetric anymore.

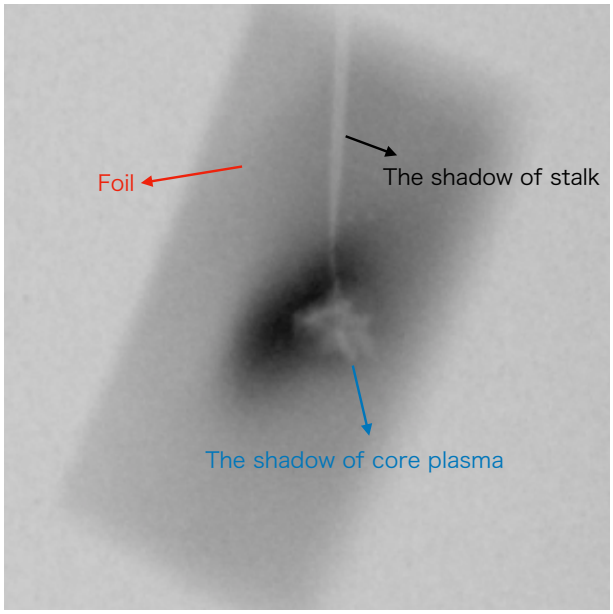

FIGURE 3.11: Flash Ti-K_α backlighting measurement result using the laser pulse which was shown in Fig. 3.10(a)

By changing the laser irradiation condition of d/R = -5, the compression experiment was also done. The laser irradiation condition d/R = -5 results in more uniform intensity distribution compare to d/R = -3 (Fig. 3.15). The measured core shape shows relatively spherical shape compare to d/R = -3 case. This indicates the strong effect of the non-uniformity of laser intensity at the fuel surface on core plasma formation. Still, the core shape is not sphere because of the laser intensity balance between laser beams. In this experiment, the maximum laser intensity was controlled to be same each other. The deviation of initial laser intensity then spread to be 20 % among 12 lasers. In this condition, the shock velocity driven by each laser beams have different values. The converging shock wave no more spherical shape, the perturbation depth of shock front surface is being higher.

A strong shock wave is stable phenomena. Even it have a perturbation, the relative perturbation defined as the perturbation depth ΔR divided by the shock front radius R_s decreases. A strong shock experiment was done using squared laser pulse. Due to the laser pulse rising time is short (100 ps Gaussian rising), strong single shock is generated. The laser irradiation condition

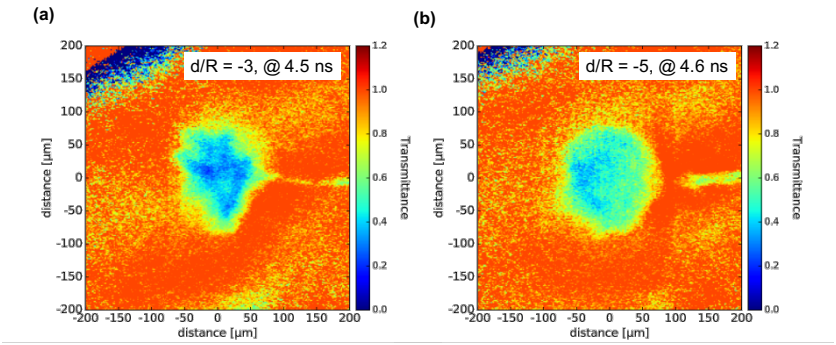

FIGURE 3.12: Flash Ti-K_α backlighting measurement results with different laser irradiation condition. (a) is the case of d/R = -3 and the image is at the timing of 4.5 ns. Even this timing is early stage of the compression, the shape of the core plasma is non-spherical, which was resulted by the laser intensity non-uniformity on the fuel surface. (b) is the case of d/R = -5 and the image is at the timing of 4.6 ns. The shape of the core plasma looks more spherical-like shape.

is set to d/R = -3, which was unstable for tailored laser pulse compression experiment. Fig. 3.13 shows the transmittance image of single shock compressed solid fuel. At all time, the shape of compressed core is round shape even the laser irradiation condition is non-uniform. The experimentally measured areal density ρR was compared to one-dimensional radiation hydrodynamic simulation results as shown in Fig. 3.14. These experimental results indicates that the weak shock wave is no more stable like strong shock wave. No theoretical and computational work on stability of weak shock wave was done. The theoretical work is difficult because the mathematical form of weak shock wave can not simplified like strong shock wave case($p_2/p_1 = \infty$). The computational work is necessary for weak shock wave calculation. There is another problem for computational work. Since the weak shock wave do not increase the entropy of the post-shocked matter, it may not be plasma. Which means, weak shocked matter is the strongly coupled matter like continuum. In this situation, the effect of chemical potential is strongly affect to the wave propagation in the matter and the temperature or density change due to shock wave varies with ideal gas case. The EOS models QEOS and/or SESAME that are widely used in plasma research region, have a large gap with the experimental results in the low temperature region. A new EOS models (like semi-empirical model) should be developed first, for studying the stability of weak shock wave.

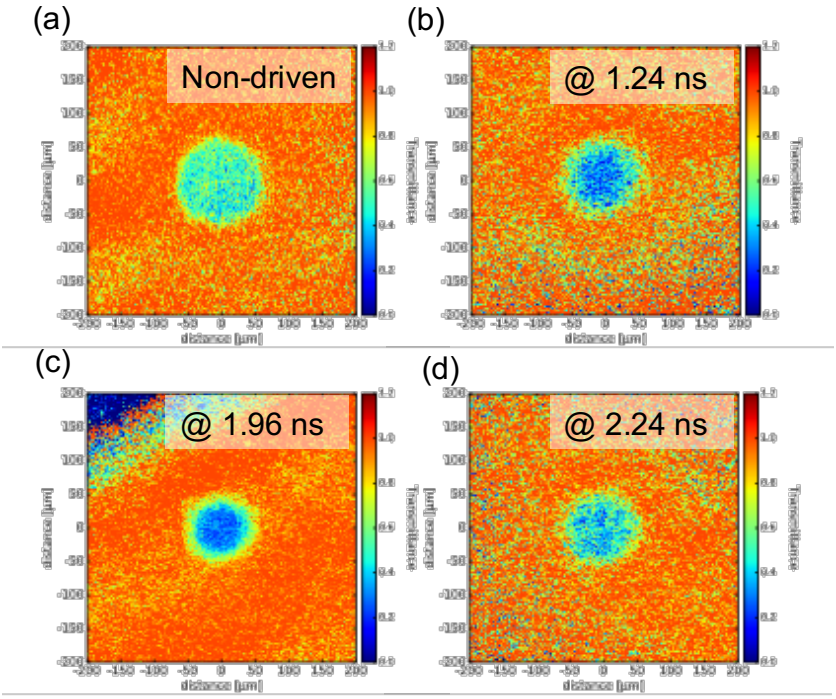

FIGURE 3.13: Flash Ti-K_α X-ray backlighting image of a solid fuel compressed by the strong shock wave.

3.4.3 Stability of a solid fusion fuel compression using tailored laser pulse

We experimentally observed the uneven shape of the compressed core plasma when using tailored laser pulse. We have numerically studied dependence of tailored laser pulse shapes and spatial beam non-uniformity on the compression of solid sphere using three-dimensional hydrodynamic simulation code (IMPACT-3D). Experimental pulse shapes may deviate from designed pulse shapes because of technical limitations and inaccuracies in modeling the equation of states also induce errors in pulse shape design. Resistance to deviation from the designed shape and spatial non-uniformity of applied pressure were investigated using three-dimensional pure hydrodynamic simulation code IMPACT-3D. In this simulation, the spatial pressure distribution on the surface of the solid sphere was calculated by 3D ray tracing code.

Evaluation of stability on multi-shock wave compression using IMPACT-3D

The IMPACT-3D which is three-dimensional pure hydrodynamic code was used[40]. IMPACT-3D have fully Eulerian and Cartesian coordinate system and both spatially, temporally has second order accuracy. The initial pressure and the density distribution is spherically symmetric.

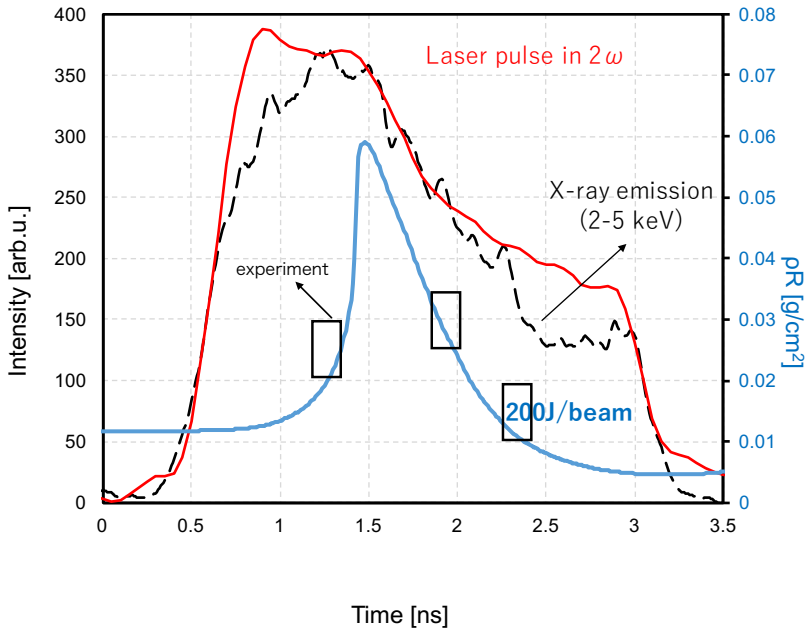

FIGURE 3.14: A compression laser timing evaluation from the X-ray emission. And the experimentally measured areal density is compared with the simulation results.

Assuming the Gekko XII facility, 12 laser beams are irradiated to the target from the direction of regular dodecahedron. The absorbed energy on the surface of the target is calculated by the 3D ray-tracing code. The initial pressure distribution on the target surface is calculated with the absorbed energy distribution. Fig. 3.15 shows the initial pressure distribution with the laser irradiation condition of d/R = -3.

The tailored laser pulse compression is simplified as three strong shock compression. The initial pressure region is defined as region I. The final pressure region is defined as region III. The initial radial pressure distribution was set as three shock waves arrive to the center at the same time.

Fig. 3.16 shows the high density compression sensitivity on pressure perturbation between 12 beams. One can easily understand that the pressure balance of low-pressure region is much more important to compress the solid ball with multi-shock wave. This is because, if converging speed is slower, absolute converging time difference of shock wave is larger under the same perturbation.

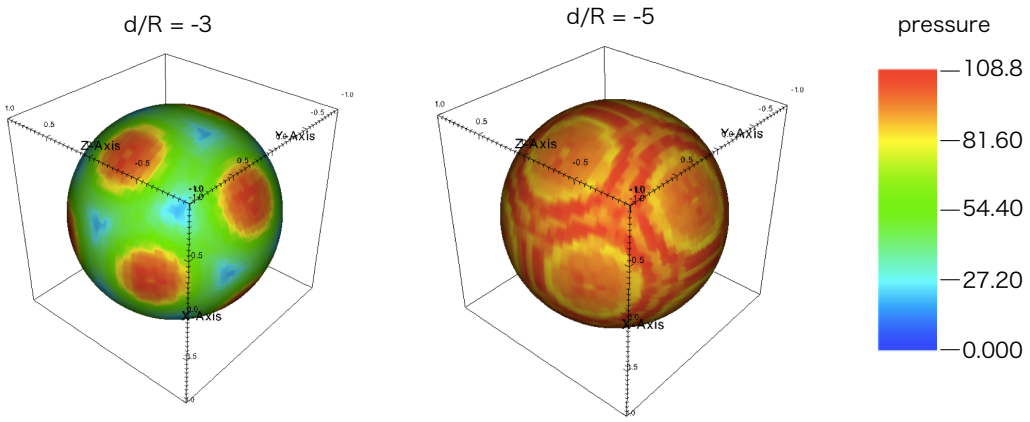

FIGURE 3.15: A pressure distribution with different laser irradiation conditions of d/R = -3 and d/R = -5.

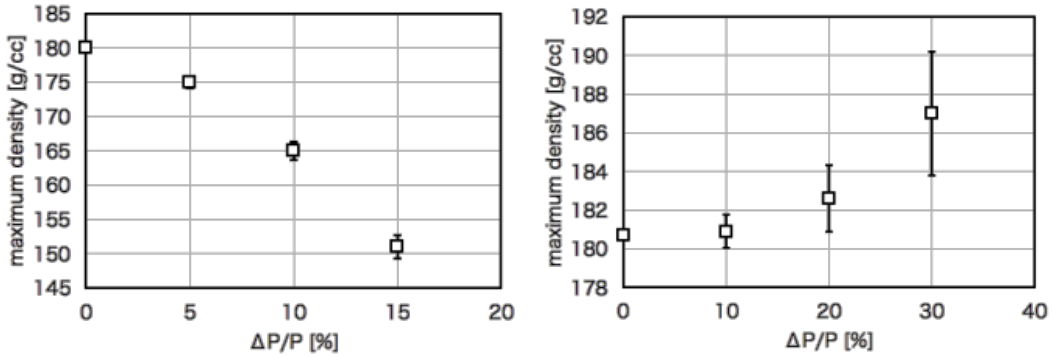

FIGURE 3.16: The image of raw data captured by backlighting method. (a) shows the Raw data image. The Ti-K_α monochromatic image of the foil and the shadows of cone-attached compressed core target is shown. Strong emission place right side of the foil is the direct light from the target consisted of photons in wide-range of photon energy. (b) shows the line out along the dashed line of (a). The data is consisted of background signal, foil emission and the shadows of the target.

Chapter 4

Two-color lasers plasma interactions for efficient production of non-thermal hot-electrons

4.1 Background

As discussed in Chapter III, lowering maximum laser intensity engineeringly have many advantages for the production of HED plasma. A conventional method for generating the shock wave is using ablation pressure. A laser can propagate only to its critical density region and deposit its energy near the critical density region where density is much smaller than the solid density, typically 100 times lower than the solid density. The electrons near the critical density region are oscillated by the oscillating laser electric field, and through the collisions the oscillating energy is being thermalized. The thermalized electron energy conducted to the direction of the solid density region and increasing the pressure. As a result, the shock wave generated. In the thermal conducting process, there are lots of energy loss. The radiation loss, and the energy is deposited to the region where the heat wave have passed by.

A another idea for generating shock wave is using hot-electrons not thermal electrons. The hot-electrons have larger range in the under dense plasma thus can penetrate the low density plasma with relatively small energy loss than thermal electrons. When the hot-electrons reaches to the solid or over solid density region, they deposit their energy there. This process is more efficient than the conventional one. Assuming laser and electron beam having same intensity. A pressure generated by the electron beam is 10 times higher than the laser ablation pressure, when 100 % of the electron beam energy is deposited to the plasma. From this advantage, using hot electron is the key parameter to increasing the shock pressure. For usage of this scheme, > 10 % hot electron conversion and < 100 keV hot electron temperature is required. Until now, the hot electron conversion was increased by increasing the laser intensity. While it may damage

the laser system and stronger laser fillamentation occurs because of strong pondermotive force. So, achieving > 10 % hot electron conversion and < 100 keV hot electron temperature without enhancing laser intensity is important.

4.2 Introduction for two color laser plasma interaction

A plasma holds waves composed of oscillating charges (electrons and ions), i.e., density fluctuations in the plasma. Both low-frequency ion wave and high-frequency electron plasma wave are excited by the ponderomotive force of a high-intensity laser. There could be a positive feedback loop in a certain condition among electromagnetic (EM) waves, electron plasma waves ans ion waves in plasma; therefore, a high-intensity laser rapidly decays into other waves. This phenomenon is referred to as laser-plasma parametric instability (LPPI). A non-thermal hot electrons are generated mainly by the electron heating due to plasma waves when using non-relativistic intensity laser.

Stimulated Raman scattering (SRS) is one of LPPIs that transfers large amplitude laser EM waves into scattered EM waves plus electron plasma waves. Two-plasmon decay (TPD) is another LPPI, in which the laser EM waves decay into two electron plasma waves. Background thermal electrons then are heated by damping of electron plasma waves in both collisional and collisionless manners, and some of them become non-thermal hot electrons. A plasma wave transmits its energy to electrons, of which the velocities are close to the phase velocity of that plasma wave. Both SRS and TPD occur in a region where the density is below a quarter critical density [$(1/4)n_{\mathrm{cr}}$] for the incident laser. Here, the critical density is given as $n_{\mathrm{cr}} = (2\pi)^2 c^2 m_{\mathrm{e}} \varepsilon_0 / e^2 \lambda_{\mathrm{L}}^2$, where c, m_{e}, ε_0, e, and λ_{L} are the speed of light, electron mass, dielectric constant, electric charge, and laser wavelength, respectively.

Many studies have been conducted on LPPIs [37, 10, 26, 30, 38, 23, 54, 44, 1, 2, 57, 56]. Several techniques have been developed to reduce the growth of LPPIs [9, 28, 11]. In particular, the LPPIs inflate the laser energy required to achieve nuclear fusion ignition in the inertial confinement fusion because the hot electrons cause preheating and degrading of the fuel compression, moreover, LPPIs increase the reflection rates of the incident lasers. On the other hand, hot electrons can be positively utilized in some applications, such as strong magnetic field generation using a laser-driven capacitor-coil [14, 6, 7, 12, 51], and shock pressure enhancement with intense spike laser [50, 32, 33].

According to theoretical studies [12, 51], the temperature of hot electrons is an important parameter to determine strength of the magnetic field generated with the laser-driven capacitor-coil scheme. Producing of hotter electrons with a large amount is a key to generate a stronger

magnetic field with this scheme. In addition, hot electrons can deposit their kinetic energy directly in an over-solid-density region, while a laser can deposit their energy only in a laser-plasma interaction region where the density is less than the critical density. Pressure, which is equal to energy density of matter, can be boosted by heating a dense plasma with adequate hot electrons, of which mean free path is shorter than the plasma thickness. A numerical simulation of the shock ignition scheme revealed a 50% enhancement of the shock pressure by hot electrons produced by LPPIs at the timing of spike laser irradiation [50].

4.3 Theory on laser plasma parametric instability

A laser plasma parametric instability(LPPI) is expressed as a resonance among waves exist in plasma. A plasma have a plasma frequency ω_p which is a eigen-frequency of the plasma. When some oscillator enters to the plasma, its behavior is determined by the plasma frequency. For example, when a electro-magnetic(EM) wave enters to the plasma, its wave vector is changed inside the plasma. That is determined by the dispersion relation as shows below.

$$\omega_0^2 = \omega_p^2 + c^2 k^2 \tag{4.1}$$

Here, ω_0, ω_p, c ,k is the EM wave frequency, plasma frequency, speed of light, and the wave vector of EM wave, respectively. From this relation, one can understand that the EM wave frequency should be lower than the plasma frequency. When $\omega_0 < \omega_p$ case, the wave vector k is to be imaginary number, which means the wave do not oscillate, but only decays with decay factor of skin depth. When $\omega_0 = \omega_p$, the wave vector k = 0, which means that the wave cannot propagate anymore. At this point, the energy of EM wave efficiently transfers to the plasma. This is representative resonance phenomena between the EM wave and the plasma.

This situation can be simplified as a sinusoidally forced oscillator as shows in Fig. 4.1. The equation of the oscillator motion is expressed as below.

$$\frac{dx^2}{dt^2} + \omega^2 x = \cos \omega_o t \tag{4.2}$$

Here ω and ω_0 is the oscillator frequency(plasma frequency) and the driver frequency (EM wave frequency), respectively. Computational calculation results shows in the graph of Fig 4.1. When ω/ω_0 = 1 case, the amplitude of the oscillator distance increase but the other cases it was not amplified. Which mean when $\omega = \omega_0$ case, the driver energy efficiently transfer to the oscillator energy. This is two-wave resonance. In laser plasma interaction, the resonance excitation of

plasma wave is the typical example of two-wave resonance. The resonance condition in this case strictly localized when ω/ω_0 is equal to 1, in the laser plasma interaction. The plasma have a temperature, the matching condition become loose due to the plasma temperature. The plasma wave frequency then modified to ω_{ek} by thermal effect as follows.

$$\omega_{ek}^2 = \omega_{\mathrm{p}}^2 + 3v_{\mathrm{p}}^2 k_{\mathrm{p}}^2 \tag{4.3}$$

where v_{p}, k_{p} is plasma velocity and the plasma wave vector, respectively. Due to the plasma have a velocity distribution(Maxwellian or non-Maxwellian), the resonance condition also loosen by the thermal effect.

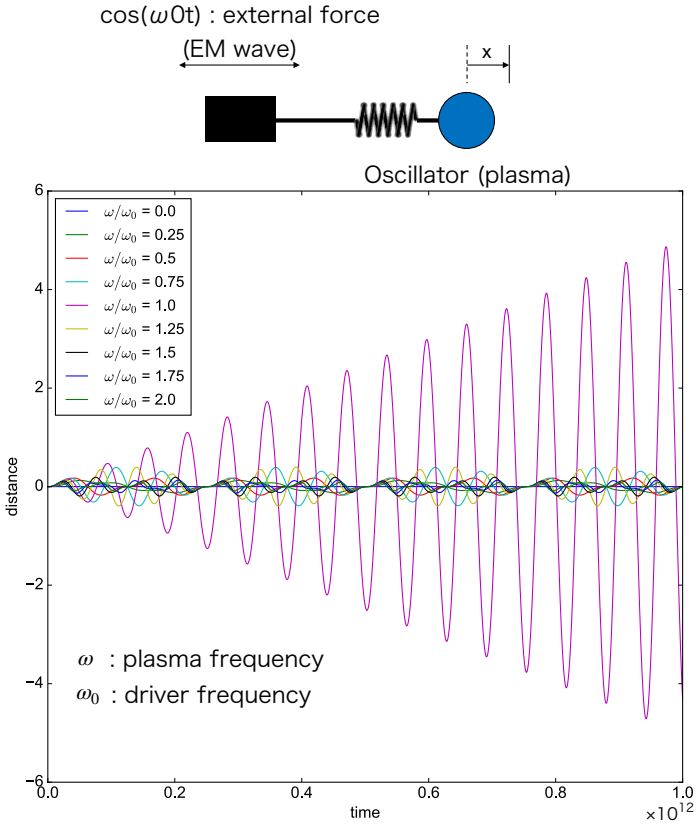

FIGURE 4.1: Correlation between Cu-K_α and electron temperature calculated by PHITS. (a) Electron temperature dependence of Cu-K_α photon flux measured from the front side and rear side detectors. (b) Calculated Cu-K_α photon ratio for different electron temperatures. The ratio is defined as the rear-measured photon flux divided by the front-measured photon flux.

The three wave interaction will be discussed below. The resonance is exist not only two-wave resonance, but also three- or four- or more resonance. However the resonance condition will be more complicated than two-wave resonance. This condition is simplified as two-connected oscillator with driver oscillator, shows in Fig. **??**

The most biggest difference with two-wave resonance is the exist of threshold. In the two-wave resonance, there is no amplitude threshold requirement on resonance but only the matching condition determine the resonance condition. In the three-wave resonance case, however, there exist an amplitude threshold to the driver. This is because the two waves excited by the driver wave, interacts each other which results in smoothing themselves. The driver amplitude should be higher than this smoothing effect. This three wave resonance equation is shown as below.

$$\frac{dx_1^2}{dt^2} + \omega_1^2 x_1 = c_1 x_2 E_0 \cos\omega_0 t \tag{4.4}$$

$$\frac{dx_2^2}{dt^2} + \omega_2^2 x_2 = c_2 x_1 E_0 \cos\omega_0 t \tag{4.5}$$

4.3.1 Stimulated raman scattering : SRS

A Raman scattering is a decay of laser wave into a plasma wave and a scattered EM wave. The positive feedback loop exist in the Raman scattering process due to the wave beating between laser wave and the scattered EM wave. A counter propagating EM wave generate a beat wave. The beat wave have large amplitude and spatial gradient so that the electron waves are exited by the beat wave. The compressional electron waves have same frequency with the plasma wave generated by Raman scattering. So the Raman scattering process become faster and faster. The Raman scattering rate grows exponentially with time, thus we call this phenomena 'instability'. And this phenomena is called as stimulated Raman scattering(SRS).

The dispersion relation of first order SRS can be expressed as below. Detailed derivation process is not showed here, and find from the ref [24].

$$\omega^2 - \omega_p^2 = \frac{\omega_p^2 k^2 v_{os}^2}{4}\left[\frac{1}{D(\omega-\omega_0, \boldsymbol{k}-\boldsymbol{k}_0)} + \frac{1}{D(\omega+\omega_0, \boldsymbol{k}+\boldsymbol{k}_0)}\right] \tag{4.6}$$

$$D(\omega, \boldsymbol{k}) = \omega^2 - k^2c^2 - \omega_p^2 \tag{4.7}$$

Here, D determines the resonance condition of SRS. The first order resonance case, whose the laser wave decays into the one plasma wave and the one scattered EM wave, ω and $\boldsymbol{k}$ will be $\omega = \omega_p + \omega_s$ and $\boldsymbol{k} = \boldsymbol{k}_p + \boldsymbol{k}_s$.

When the laser wave decays into two plasma wave and one scattered EM wave, that is the second order SRS resonance which occurs below 1/16 critical density region. The matching condition of that situation can be expressed as the following.

$$\omega = \omega_p + \omega_p + \omega_s \tag{4.8}$$

$$\boldsymbol{k} = \boldsymbol{k}_p + \boldsymbol{k}_p + \boldsymbol{k}_s \tag{4.9}$$

Due to the difference of ω_s between the first and the second order resonance SRS, ω_p and $\boldsymbol{k}_p$ is differ.

For example, here we think at 0.05 n_c of 527 nm laser having $\omega_{L2} = 2\omega_{L1}$ and ω_{L1} is the frequency of 1053 nm laser. The plasma frequency ω_{pe} at 0.05 n_c of 527 nm laser is = 0.45 ω_{L1}. Firstly, we think the first order SRS, and from the matching condition, ω_s = 1.55 ω_{L1} and dispersion relation of EM wave in a plasma leads $\boldsymbol{k}_s = 1.48\boldsymbol{k}_{L1}$. The the plasma wave have $\omega_p = 0.45\omega_{L1}$ and $k_p = 3.43k_{L1}$ for back scattering (SRBS) and $\omega_p = 0.45\omega_{L1}$ and $k_p = 0.465k_{L1}$ for forward scattering (SRFS) case. If we consider the Landau damping condition $k_p\lambda_D$<0.35 in the 1 keV temperature plasma, k_p should be less than $1.88k_{L1}$. Thus the first order SRBS at 0.05 n_c can not grow due to Landau damping. The phase velocity of 1st-order SRFS is 0.967 c.

With same process, the scattered EM wave due to the second order SRS have $\omega_s = 1.1\omega_{L1}$ and $k_s = 1.0k_{L1}$. The plasma waves then have $\omega_p = 0.45\omega_{L1}$ and $k_p = 0.974\omega_{L1}$ for forward scattering case and $\omega_p = 0.45\omega_{L1}$ and $k_p = 0.474\omega_{L1}$ for forward scattering case. Those can grow much larger because of smaller Landau damping effect compare to the first order SRS generated plasma wave case. The phase velocity of 2nd-order SRBS is 0.46 c and that of 2nd-order SRFS is 0.95 c. This situation can be found in simulation.

Here the one dimensional(1D) particle in cell(PIC) simulation was done.

Instability threshold of SRS

The threshold intensity is determined by the plasma density gradient and temperature. In inhomogeneous plasma, SRS can grow resonantly in the limited region. A wave energy propagates to a non-resonant region. So the growth of the SRS should be faster than the out flowing of the wave. Due to the wave vector is the function of position, $\kappa = k_1(z) - k_2(z) - k_3(z)$ can be defined. If $\kappa = 0$, the waves are resonantly couple or this point a mismatch developes. It can be estimated that the size of the interaction region

Langmuir decay instability : LDI

When the amplitude of the plasma wave is big enough to affect the ion motion, the plasma wave start to decay into a back scattered plasma wave and an ion acoustic wave. According to the dispersion relation, the frequency of ion acoustic wave is much smaller than that of plasma wave. Thus the back scattered plasma wave have almost same frequency with the initial plasma wave, and have almost same wave vector. This is why the hot electrons are generated with same amount to the direction of back and forth. Also, due to LDI, the instability saturated. Due to the initial plasma wave decays into the plasma wave having completely different characteristics with the initial plasma wave, the matching condition breaks. Thus the instability saturated. Preliminary researches suggests that the saturation occur almost within 10 ps with laser intensity larger than 10^{14} W/cm^2. In the case of an interaction between nano-second laser and plasma, it can be said that laser plasma instabilities are all saturated.

4.3.2 Plasma heating

Collisional damping

Electron-ion collisions make plasma wave damping. Due to the plasma wave is the compressional wave, having collective electrons motion. While the collision make the electron motion randomly with the rate of electron-ion collisions. The collisional damping rate ν_c is

$$\nu_c = \frac{\omega_{pe}^2}{\omega_p^2}\nu_{ei} \tag{4.10}$$

where ν_{ei} is the electron ion collision rate. The collisional damping effect may affect to the growth of the plasma wave at high dense region, while the conditions in ICF, the collisional effect is not major cause affecting to the LPPI.

Landau damping

A plasma wave can be damped even without the particle collisions due to the Landau damping. The Landau damping is the collisionless plasma wave damping phenomena. Most of the background electrons are not resonantly interact with plasma waves because plasma waves typically have much faster phase velocity than the electron thermal velocity. A small amount of particles resonantly interact with plasma waves having velocity close to the plasma wave phase velocity. Then the wave energy resonantly transmit to the electrons. The damping rate can be expressed

as below.

$$\frac{\gamma}{\omega_p} = \frac{\pi}{2}\frac{\omega_{pe}^2}{k_p^2}\frac{\partial f}{\partial v}\left(\frac{\omega}{k_p}\right) \tag{4.11}$$

where f is the plasma distribution function, ω_p is the plasma wave frequency and ω_{pe} is the plasma frequency. Note that γ depends on the slope of distribution function at phase velocity. If we consider a Maxwellian distribution with thermal velocity v_{th},

$$\frac{\gamma}{\omega_p} = -\sqrt{\frac{\pi}{8}}\frac{\omega_{pe}^2\omega_p}{{k_p}^3 v_{th}^3}\exp\left(-\frac{\omega_p^2}{2k_p^2 v_{th}^2}\right) \tag{4.12}$$

The Landau damping become effective when the growth factor 2π is comparable to the damping factor $-\omega_p^2/(2k_p^2v_{th}^2)$. From this, we can get the relation ω_p^2/k_p^2<$12.4v_{th}^2$. The dispersion relation of plasma wave $\omega_p^2 = \omega_{pe}^2 + 3k_p^2v_{th}^2$ lead the previous relation to ω_{pe}^2/k_p^2<$9.4v_{th}^2$. Using the Debye length $\lambda_D = v_{th}/\omega_{pe}$, it can be finalized that the Landau damping is sizable when $k_p\lambda_D$>0.3. Only the plasma wave having wave vector satisfying $k_p\lambda_D$<0.3 can grow effectively.

Non-relativistic zero temprature wave-breaking

A plasma wave, which is the compressional wave of electrons, is supported by the coherent motion of electrons. Electrons transmit the information of wave phase via collisions between neighbor electrons. When a potential depths of plasma waves become larger than so-called wave-breaking value, coherent motion of electrons dissipate. The most heuristic physical images of wave-breaking can be derived by comparing the electron velocity accelerated by the electric field of plasma wave $v_e = eEm_e^{-1}\omega_{\mathrm{p}}^{-1}$ and the phase velocity of the plasma wave v_ϕ. If the electron velocity is faster than the phase velocity of the plasm wave, the wave no more can be supported by electrons, then the plasma wave-breaking occur.

The maximum electric field $E_{\max}$, is then expressed as:

$$E_{\max} = \frac{m_e\omega_{\mathrm{p}}v_\phi}{e}. \tag{4.13}$$

Thermal effect and relativistic effect should be considered. Thermal effect reduce the maximum potential depth for two reasons : effect of diffusion by plasma pressure, thermal velocity of electrons enables them to be trapped at a lower potential depth than if they were initially at rest.

non-relativistic finite temperature wave-breaking

To derive the wave-breaking amplitude under finite temperature, a fluid model is used. Here it begin from the Vlasov equation and Maxwell equations.

$$\left(\frac{\partial}{\partial t}+v\frac{\partial}{\partial x}-\frac{eE}{m}\frac{\partial}{\partial v}\right)f=0 \tag{4.14}$$

$$\frac{\partial E}{\partial t}-4\pi env=0 \tag{4.15}$$

$$\frac{\partial E}{\partial x}-4\pi e(n-n_0)=0 \tag{4.16}$$

Then the momentum integrations of Vlasov equation leads to fluid equations. From mass conservation,

$$\frac{\partial}{\partial t}n+\frac{\partial}{\partial x}nv=0 \tag{4.17}$$

And the momentum conservation,

$$\frac{\partial}{\partial t}nv+\frac{\partial}{\partial x}\left(nv^2+\frac{p}{m}\right)=-en\frac{E}{m} \tag{4.18}$$

Due to the adiabatic pressure p is

$$\frac{p}{n^3}=\text{constant} \tag{4.19}$$

$$\frac{p}{n^3}=\frac{p_0}{n_0^3} \tag{4.20}$$

$$p=\frac{n^3}{n_0^3}p_0 \tag{4.21}$$

Due to the initial pressure $p_0=n_0k_BT_0$, we find

$$p=\frac{n^3}{n_0^2}k_BT_0 \tag{4.22}$$

From the Eq. 4.17, Eq. 4.18 can be reduced to Euler equation

$$\frac{\partial}{\partial t}v+v\frac{\partial}{\partial x}v=-\frac{eE}{m}-\frac{1}{mn}\frac{\partial}{\partial x}p \tag{4.23}$$

It is assumed that the solution is wave-like, where the fluid quantities are functions of the single variable $\Psi=t-(x/v_\phi)$. From this, the partial different $\partial/\partial t=\partial/\partial\Psi$ and $\partial/\partial x=-v_\phi^{-1}\partial/\partial\Psi$. Then Eq. 4.23, 4.15, 4.16, the Euler, Ampere, and Gauss equation, respectively

can be expressed as the following, using the plasma temperature $k_B T_0 = (m v_0^2/3)$.

$$\left(1-\frac{v}{v_\phi}\right)\frac{\partial}{\partial\Psi}v = -\frac{eE}{m}+\frac{1}{2}\frac{v_0^2}{v_\phi}\frac{1}{n_0^2}\frac{\partial}{\partial\Psi}n^2 \tag{4.24}$$

$$\frac{\partial E}{\partial\Psi}-4\pi env = 0 \tag{4.25}$$

$$-\frac{1}{v_\phi}\frac{\partial E}{\partial\Psi}+4\pi e(n-n_0) = 0 \tag{4.26}$$

Therefore, by combining these three equations Eq. 4.24, 4.25, 4.26,

$$\frac{\partial}{\partial\Psi}\left(v-\frac{v^2}{2v_\phi}-\frac{v_0^2 n^2}{2v_\phi n_0^2}\right) = -\frac{eE}{m} \tag{4.27}$$

The relation between v and n can be obtained from Eq. 4.25 and 4.26, and expressed as,

$$n = \frac{n_0}{1-v/v_\phi}. \tag{4.28}$$

By substituting Eq. 4.28 into Eq. 4.27, and defining $x = v/v_\phi$,

$$\frac{\partial}{\partial\Psi}\left(x-\frac{x^2}{2}-\frac{1}{2}\frac{v_0^2}{v_\phi^2}\frac{1}{(1-\beta)^2}\right) = -\frac{eE}{mv_\phi} \tag{4.29}$$

Differentiating Eq. 4.29 and substituting Ampere's law Eq. 4.15,

$$\frac{\partial^2}{\partial\Psi^2}\left(x-\frac{x^2}{2}-\frac{1}{2}\frac{v_0^2}{v_\phi^2}\frac{1}{(1-c)^2}\right) = -\omega_p^2\frac{x}{1-x}. \tag{4.30}$$

This can be integrated by multiplying through by Eq. 4.29 and resulting in

$$\frac{1}{2}\frac{\partial}{\partial\overline{\Psi}}\overline{E}^2 = \frac{\partial}{\partial\overline{\Psi}}\left[\frac{x^2}{2}-\overline{v_0}^2\left(\frac{1}{3}\frac{1}{(1-x)^3}-\frac{1}{2}\frac{1}{(1-x)^2}\right)\right]. \tag{4.31}$$

Here, $\overline{E} = eE/mv_\phi\omega_p$, $\overline{v_0} = v_0/v_\phi$ and $\overline{\Psi} = \omega_p\Psi$.

Finally, the non-relativistic finite-temperature wave-breaking limit is expressed as the following.

$$E_{\max} = \frac{m_e v_\phi \omega_{\mathrm{p}}}{e}\left(1-\frac{8}{3}\beta^{1/4}+2\beta^{1/2}-\frac{1}{3}\beta\right) \tag{4.32}$$

where $\beta = 3k_{\mathrm{B}}T_{\mathrm{e}}/m_{\mathrm{e}}v_{\phi}^2$ and k_{B} and T_{e} are the Boltzmann constant and plasma electron temperature, respectively.

Relativistic finite-temperature wave-breaking

Finally, the relativistic finite-temperature wave-breaking limit is expressed as the following.

$$E_{\max} = m_e v_{\phi} \omega_{\mathrm{p}} e^{-1} \beta^{-1/4} \left(\ln 2 \gamma_{\phi}^{1/2} \beta^{1/4} \right)^{1/2}, (\text{relativistic}) \tag{4.33}$$

where $\beta = 3k_{\mathrm{B}}T_{\mathrm{e}}/m_{\mathrm{e}}v_{\phi}^2$, $\gamma_{\phi} = (1-(v_{\phi}/c)^2)^{-0.5}$ and k_{B} and T_{e} are the Boltzmann constant and plasma electron temperature, respectively.

4.4 Two-color laser plasma interaction experiment

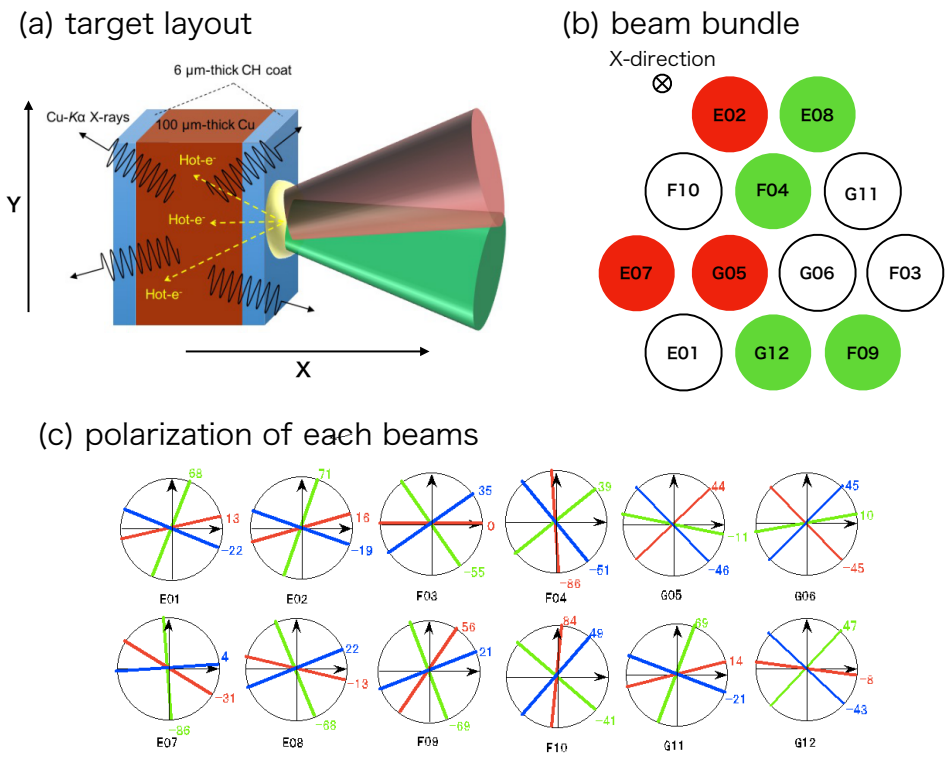

FIGURE 4.2: (a)Schematic diagram of experimental setup. Cu is used as a tracer to convert hot electrons to Cu-Kα photons. The plastic coating prevents direct interaction between the lasers and Cu. The hot electrons are characterized using Cu-Kα spectra measured from the laser-irradiation side (front side) and rear side. (b) The placement of beam bundle. In this research, Beam 2,5,7 was used as 1053 nm wavelength, and the beam 4, 8, 9,12 were used as 527 nm wavelength. (c) The polarization information of each beams. The beam set of [2] for 1053 nm and [8, 9] for 527 nm is selected to be the crossing angle of polartization is 87 °, and the [7] for 1053 nm and [8,9] for 527 nm is that to be 37 ° and [5] for 1053 nm and [4, 12] for 527 nm is that to be 1 °.

We have developed a scheme to efficiently produce hot electrons using two-color lasers, primary (λ_{L1} = 527 nm) and secondary (λ_{L2} = 1053 nm) lasers. The experiment was performed on the GEKKO-HIPER system at the Institute of Laser Engineering, Osaka University. HIPER system is consisted of 12 laser beams irradiated from the single direction. with F/15 lenses. The wavelength of each laser can be changed independently between λ_1 = 527 nm and λ_2 = 1053 nm (351 nm is available). All lasers have a temporal pulse shape that consists of 0.9 ns of full-width-at-half-maximum (FWHM) of a Gaussian function in the rising edge and 1.45 ns

of FWHM of a Gaussian function in the falling edge. The intensity of the primary laser was fixed at $I_{L1} = 9.0 \times 10^{14}$ W/cm^2. The intensity of the secondary laser was varied from $I_{L2} = 1.5 \times 10^{12}$ W/cm^2 to $I_{L2} = 7.0 \times 10^{14}$ W/cm^2. The focal spot diameter of both the primary and secondary lasers was fixed to 200 μm. The crossing angle Θ_{cross} between polarizations of the primary and secondary lasers was also changed among 87°, 37° and 1°. Fig. 4.2 (b) show the beam position and its polarizations. In this experiment, two 527 nm laser beams having almost same polarization angle, was used because of the intensity threshold of SRS. The intensity threshold of SRS of 527 nm is 4.0×10^{15} W/cm^2 and 4.0×10^{15} W/cm^2 laser intensity is the maximum intensity for one 527 nm laser beam. The beam lens position of each beams is shown in Table 4.1

TABLE 4.1: The absolute position of beam lenses

Beam number	X [mm]	Y [mm]	Z [mm]
1	4974.615	-435.778	-501.998
2	4974.615	-216.851	628.392
3	4974.615	652.628	-126.398
4	4974.615	0.0	251.837
5	4974.615	-218.097	-125.918
6	4974.615	218.097	-125.918
7	4974.615	-652.628	-126.398
8	4974.615	216.851	628.392
9	4974.615	435.778	-501.998
10	4974.615	-435.778	251.597
11	4974.615	435.778	251.597
12	4974.615	0.0	- 501.998

Fig. 4.2 shows the schematic diagram of experimental setup. A 100 μm thick Cu plate coated with a 6 μm thick parylene plastic was irradiated with the lasers. The plastic layer prevents the Cu plate from direct heating by the lasers. The lasers interact with the plastic layer and the Cu plate is a tracer to detect hot electrons traveling through the plastic layer and coming in the Cu plate as emission of Cu-K_α photons. The Cu tracer layer has sensitivity only to hot electrons whose kinetic energies are larger than the K-shell ionization energy (8.94 keV) of a neutral Cu atom.

The temperature, number, and spray angle of hot electrons were evaluated from comparisons between absolute Cu-K_α spectra and computations with the PHITS code [41], which is a three-dimensional Monte-Carlo simulation code used to treat radiation and particle transport in

matter. Cu-K_α spectra were measured with two calibrated X-ray spectrometers located at both the laser-irradiated front-side and the opposite rear-side. The X-ray spectrometer utilized highly oriented pyrolytic graphite (HOPG) as X-ray dispersion optics. The uncertainty of calibration was $\pm 16\%$, which is caused by the non-uniformity of the integral reflectivity of the HOPG over its full surface. X-ray spectra observed from the front and rear sides were different due to differences of the X-ray attenuation length from the Cu-K_α emission region to the spectrometers, and the Cu-K_α emission sizes between the front and rear sides, as described in the following section.

4.5 Experimental results

Hot electron characteristics measurement

The electrons generated at the front side travel through the tracer layer with spatial spread because of the hot electron divergence with half-spray angle θ_{spray} and spread by collisions between hot electrons and bulk electrons in the tracer layer. Therefore, the electron spray angle θ_{spray} can be modeled from a convolution of the Cu-K_α emission profiles at the front and rear sides as Eq. (1). These profiles are assumed to be Gaussian functions. Under this assumption, the FWHM of the Cu-K_α emission spot at the rear side (D_{rear}) is the square sum of the FWHM at the front side (D_{front}), The FWHMs of the point spread functions are caused by the spray angle [$2d\tan(\theta_{\text{spray}})$], and the collisional spread (D_{col}), which is expressed as:

$$D_{\text{rear}}^2 = D_{\text{front}}^2 + (2d\tan(\theta_{\text{spray}}))^2 + D_{\text{col}}^2, \tag{4.34}$$

where θ_{spray} and d are the half-spray angle of hot electrons and the thickness of the Cu layer, respectively. PHITS computation gave D_{col} = 130 μm under the experimental conditions.

Those spot diameters can be calculated from Cu-K_α line widths observed from the front and rear sides because the spectral line width $\Delta h\nu_{\text{source}}$, is broadened by the X-ray source size and is given as:

$$\Delta h\nu_{\text{source}} = \frac{D \cdot h\nu}{l} \frac{\cos\theta_{\text{B}}}{\tan\theta_{\text{B}}}, \tag{4.35}$$

where $h\nu$, D, l, θ_{B} are the photon energy, the X-ray source diameter, the distance between the source and the detector, and the Bragg angle, respectively.

The spectral resolution of the X-ray spectrometer is determined mainly by the thickness of the HOPG. A HOPG thickness of 1 mm corresponds to 15 eV of the spectral resolution; which is the FWHM according to the relation between HOPG thickness and the line broadening function

given in Ref. [58]. The measured Cu-K_α line widths were wider than the spectral resolution. Possible spectral line broadening effects were taken into account to reproduce the measured spectral width, such as natural broadening, opacity broadening, Zeeman broadening, Doppler broadening, Stark broadening and source size broadening.

The least-square method for two-variable was adapted to find appropriate combination of $\Delta h\nu_{\mathrm{Stark}}$ and $\Delta h\nu_{\mathrm{source}}$ to reproduce the observed Cu-K_α spectra because complicated calculations are required for accurate estimation of the Stark broadening for the Cu-K_α line emitted from a high-energy-density solid Cu layer. A Lorentzian function was used as the function for the line broadening caused by the Stark effect because collisional Stark broadening can be dominant in this experiment. A Gaussian function was used as the function for the line broadening caused by the source size. A Cu-K_α spectral profile was simulated as a convolution of the original X-ray spectrum, the spectral resolution function, the Lorentzian Stark broadening function, and the Gaussian source size broadening function. The square sums of the differences between the measured and calculated spectral intensities at each photon energy point were calculated with changing $\Delta h\nu_{\mathrm{Stark}}$ and $\Delta h\nu_{\mathrm{source}}$. Fig. **??** shows (a) the front and (b) the rear side measured Cu-K_α spectrum. The X-ray intensity is normalized for comparing shapes of spectrums.

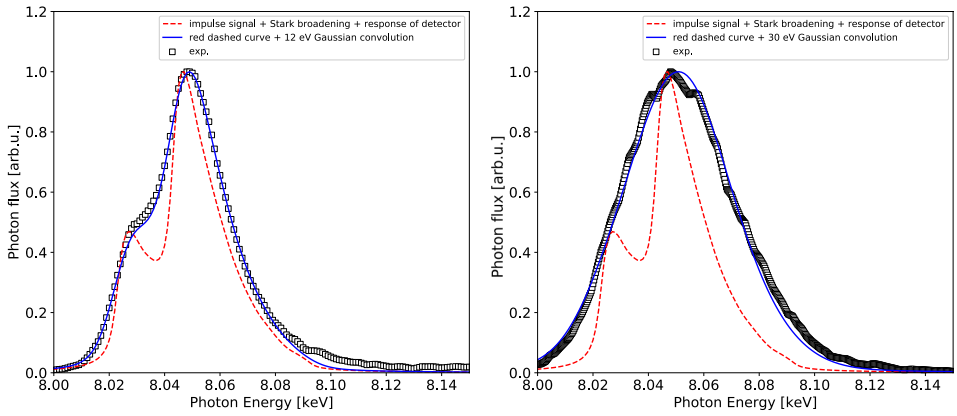

FIGURE 4.3: The Cu-K_α spectrum measured from the front side (a) and the rear side (b). The red dashed line shows the broadened impulse signal of Cu-K_α spectrum without source size broadening. The spectrum of blue solid line contains the source size broadening and reproduce the experimental data well. A Cu-$K_{\alpha 1}$ (8.048 keV) and $K_{\alpha 2}$ (8.028 keV) can be distinguishable in the front side measured spectrum while the rear side measured spectrum shows only one broad spectrum.

For example, $\Delta h\nu_{\mathrm{Stark}}$ and $\Delta h\nu_{\mathrm{source}}$ were estimated to be 4±2 eV and 14±2 eV at shot ID 40899, respectively. The 14±2 eV FWHM of the source size broadening corresponds to the 211±30 μm of the Cu-K_α source diameter. The spray angles were finally evaluated with the

estimated Cu-K_α emission diameters at the front and rear sides using the procedure described above. The estimated spray angles are listed in Table **??**.

The temperature of hot electrons was estimated from the ratio between the Cu-K_α intensities measured from the front and rear sides. The energy distribution of hot electrons was assumed to be a single temperature Boltzmann function as $f(E) = (N_{\rm hot}/T_{\rm hot}) \cdot \exp(-E/T_{\rm hot})$, where $N_{\rm hot}$ and $T_{\rm hot}$ are the number and temperature of the hot electrons, respectively. The Cu-K_α intensity ratios were computed with the PHITS code for the Cu tracer layer and hot electrons having $D_{\rm front}$, $\theta_{\rm spray}$ and $T_{\rm hot}$.

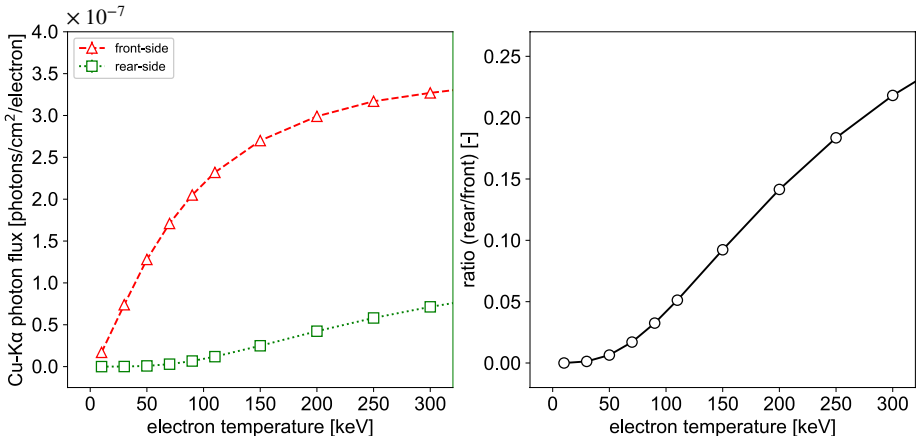

FIGURE 4.4: Correlation between Cu-K_α and electron temperature calculated by PHITS. (a) Electron temperature dependence of Cu-K_α photon flux measured from the front side and rear side detectors. (b) Calculated Cu-K_α photon ratio for different electron temperatures. The ratio is defined as the rear-measured photon flux divided by the front-measured photon flux.

Fig. 4.4 (a) shows the computed dependence of the Cu-K_α photon yields per hot electron in units of photons/cm^2/electron, which were measured from the front (triangle marks) and rear (square marks) sides on the electron temperature. Fig. 4.4 (b) shows the computed dependence of the Cu-K_α ratio on the electron temperature. The front-side Cu-K_α photon yield was almost saturated for $T_{\rm hot} > 250$ keV because the K-shell ionization cross-section peaks around 24 keV and decreases until 1 MeV, while the rear-side Cu-K_α photon yield increases continuously, even for $T_{\rm hot} > 250$ keV. The temperature of hot electrons was determined uniquely from the yield ratio shown in Fig. 4.4 (b). The absolute number of hot electrons ($N_{\rm hot}$) was calculated from the absolute Cu-K_α photon yields measured from both the front and rear sides with the computed dependence show in Fig. 4.4 (a). The conversion efficiency $\eta_{\rm hot}$, is defined as the ratio between the total kinetic energy of the hot electrons and the incident laser energy.

The final experimental results are listed in Table. 4.2. The listed errors are evaluated from the uncertainty of Cu-K_α photon yields. Identifying the exact area of the HOPG where the X-ray diffracted is practically difficult. We used the uncertainty of $\pm 16\%$ caused by the non-uniformity of the integral reflectivity of the HOPG over its full surface as the error of Cu-K_α photon yield. The alignment between target and HOPG was not changed during all measurements. The detected Cu-K_α photons were always reflected from the same area in the HOPG. It is important to refer here that the listed errors of data are a certain value within the error, keeping relations between other values.

Backscattered visible light spectroscopy

A near-backscattered visible light spectrum was measured for understanding the origin of high energy electron generation. The spectroscopy system was set to the 3 ° tilted side of incident laser axis. To avoid the scattered light from the experimental environment, an imaging system was used. The target image is imaged on the slit of the spectrometer. The Raman scattered light is the direct proof of the SRS. However, it was not applicable in our experiment. That is because the Raman scattered light of 527 nm laser is covered by the strong reflected light of 1053 nm. The photon energy of Thomson scattered probe laser is shifted by the interaction between plasma waves as shown in Fig. **??**. As a probe laser, 527 nm laser was used. That is because, 527 nm laser was the main laser beam and its laser intensity did not changed for all experiment.

The measured near-backscattered is shown in Fig. 4.5. Near 351 nm, there is a strong signal which means the existence of the absolute SRS of 527 nm laser. The case of 526 nm laser only and 1053 nm + 526 nm laser have same intensity of 351 nm signal which means that two wave mixing does not affect to the SRS of 526 nm laser. While 421 nm signal is significantly changed. 421 nm signal means the existence of SRS of 1053 nm laser or plasma waves generated near the quarter critical density of 1053 nm laser. Other signals are not backscattered signal but noises. From the backscattered light spectroscopy, it can be understood that the laser plasma instability occurs in this experiment, and the increase of electron temperature and conversion efficiency might be related to the increase of 421 nm wavelength signal.

4.6 Discussion

From now, discussions will be done using data of $\Theta_{\mathrm{cross}} = 87^\circ$. Irradiation of two-color lasers significantly increases T_{hot} and η_{hot} as shown in Fig. 4.6 (a). The maximum electron temperature

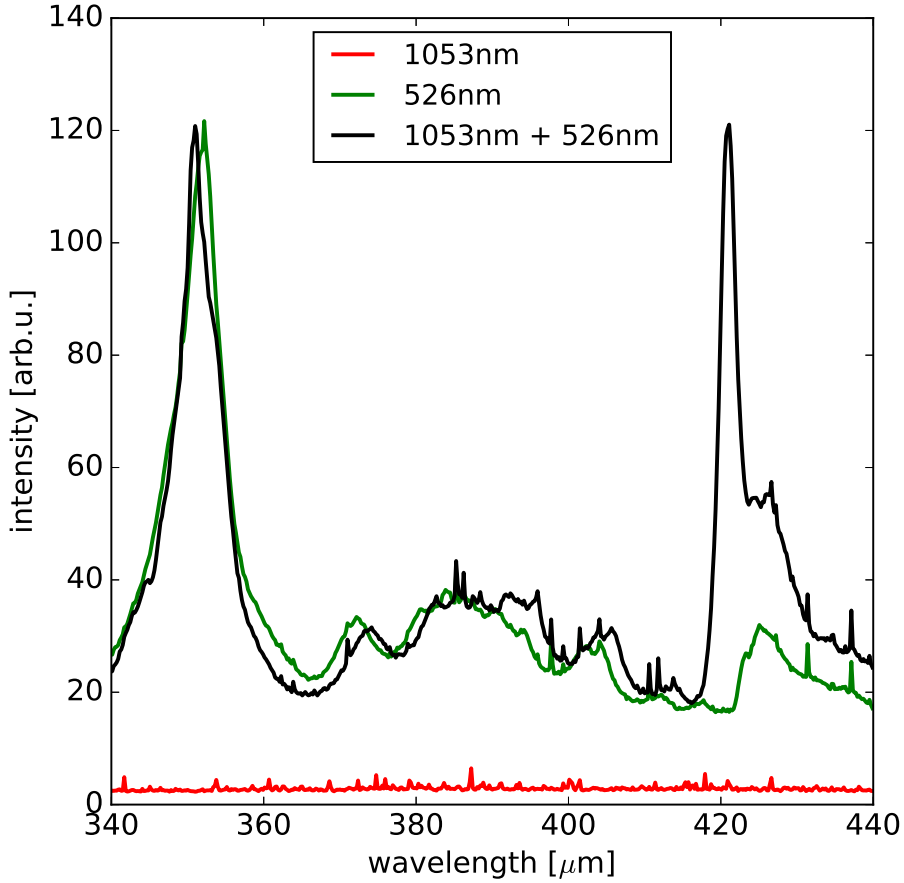

FIGURE 4.5: Spectrum of backscattered 527 nm laser light by the plasma wave.

of $T_{\mathrm{hot}} = 273 \pm 80$ keV (shot ID 40883) obtained with two-color laser irradiation was higher than that obtained with single color laser irradiation: $T_{\mathrm{hot}} = 57 \pm 4$ keV with the 527 nm laser (shot ID 40899) and $T_{\mathrm{hot}} = 51 \pm 4$ keV with the 1053 nm laser (shot ID 40897). The energy conversion efficiency $\eta_{\mathrm{hot}} = 12.5 \pm 2.0$ % (shot ID 40883) obtained with two-color laser irradiation was higher than the sum of those obtained with single color laser irradiation: $\eta_{\mathrm{hot}} = 4.5 \pm 0.5\%$ with the 527 nm laser (shot ID 40899) and $\eta_{\mathrm{hot}} = 0.5 \pm 0.1\%$ with the 1053 nm laser (shot ID 40897).

This result infers the staged heating mechanism [54, 57]. 'Staged' means a 'handover' of electrons from a slower phase velocity plasma wave to a higher phase velocity plasma wave. A large amplitude electron plasma wave traps electrons, of which the velocities are close to the wave phase velocity v_ϕ, in the electric potential valley. The trapped electrons move oscillatory within the potential valley of the electron plasma wave. The electron plasma wave is damped

TABLE 4.2: Summary of experimental results

Shot ID	Θ_{cross} [degree]	I_{L1} (527 nm) [W/cm^2]	I_{L2} (1053 nm) [W/cm^2]	T_{hot} [keV]	η_{hot} [%]	θ_{spray} [degree]
#40899		8.57×10^{14}	**N/A**	57±4	4.5±0.5	41±5
#40897		**N/A**	6.27×10^{14}	51±4	0.5±0.1	41 ± 5
#40888	87	8.53×10^{14}	1.50×10^{12}	172±25	3.2±0.4	47 ± 5
#40887		8.52×10^{14}	9.79×10^{12}	139±17	1.6±0.2	45 ± 5
#40884		9.11×10^{14}	8.47×10^{13}	239±58	3.8±0.4	54 ± 6
#40883		9.35×10^{14}	6.93×10^{14}	273±80	12.5±2.0	60 ± 7
#40899		8.07×10^{14}	**N/A**	57±4	4.5±0.5	41 ± 5
#40891	37	**N/A**	6.10×10^{14}	41±4	1.9±0.2	41 ± 5
#40874		9.45×10^{14}	8.35×10^{14}	150±21	13.1±2.1	61 ± 7
#40872		8.53×10^{14}	**N/A**	39±7	2.2±0.2	41 ± 5
#40873		**N/A**	5.78×10^{14}	24±5	0.4±0.1	41 ± 5
#40889	1	8.64×10^{14}	6.93×10^{12}	22±5	0.2±0.1	42 ± 5
#40885		8.03×10^{14}	6.90×10^{13}	28±6	1.1±0.1	45 ± 5
#40876		9.04×10^{14}	7.25×10^{14}	89±8	3.0±0.2	49 ± 6

by transferring its energy to the trapped electrons.

The electron velocity must be within the range of $v_\phi \pm \Delta v_{tr}$ to be trapped by the potential valley moving with v_ϕ, where Δv_{tr} is the trapping velocity relative to v_ϕ. The trapping condition is satisfied when the kinetic energy of a trapped electron is below the depth of the potential well; therefore, the maximum trapping velocity is given as $\Delta v_{tr} = 2\sqrt{e\Phi_{max}/m_e}$, where Φ_{max} is half of the potential well depth.

To calculate electron trapping energy range of a plasma wave, it is necessary to evaluate the amplitude of plasma wave. In the case of $\gamma_\phi \gg 1$, the relativistic form of maximum electric field was used, otherwise, non-relativistic form was used. $E = -\nabla\Phi$ can be approximated as $\Phi_{max} = E_{max}/k_p$ for a sinusoidal plasma wave, where the wave number is k_p. Notice that Φ_{max} is determined by characteristics of plasma wave like k_p, ω_p and v_ϕ.

The characteristics of the plasma wave is determined by the plasma electron density and wave matching conditions. The plasma electron density n_e = 0.06 n_{cr1} is assumed in this discussion, where n_{cr1} is the critical density for the primary laser (λ_{L1} = 527 nm). The convective SRS has the peak gain coefficient near 0.06 n_{cr1}[43] with the electron temperature T_e = 0.86 keV. The electron temperature was computed using two-dimensional radiative hydrodynamic simulation code FLASH [13]. Due to the twice longer wavelength of the secondary laser, the density 0.06 n_{cr1} corresponds to 0.24 n_{cr2}, which is near the quarter critical density

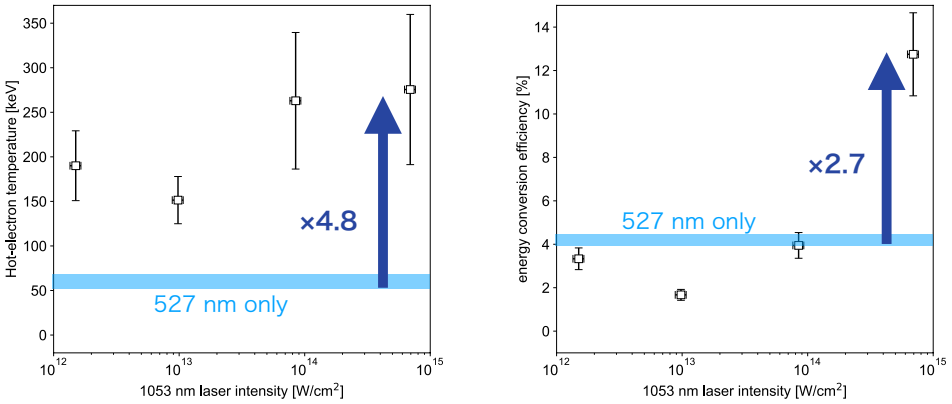

FIGURE 4.6: (left) Hot electron temperature versus 1053 nm laser intensity. (right) Hot electron conversion efficiency versus 1053 nm laser intensity.

of the secondary laser, absolute SRS of secondary laser (λ_{L2} = 1053 nm) exists. Considering one-dimensional LPPIs, electron plasma waves are generated by stimulated Raman back scattering (SRBS) and stimulated Raman forward scattering (SRFS). The lengths of the plasma wave vector caused by SRBS and that caused by SRFS have different values due to the wave frequency matching condition($\omega_L = \omega_s + \omega_p$) and wave vector matching condition($\boldsymbol{k}_L = \boldsymbol{k}_s + \boldsymbol{k}_p$). Here ω and $\boldsymbol{k}$ are angular frequency and wave vector of plasma wave, subscripts of L, s, p indicates laser EM wave, scattered EM wave and plasma wave, respectively. Then, the minimum and maximum trappable electron energy can be evaluated: $\varepsilon_{min} = (1/2)m_e(v_\phi - v_{tr})^2$ and $\varepsilon_{max} = (1/2)m_e(v_\phi + v_{tr})^2$.

Fig. 4.7 shows the energy ranges of trappable electrons in electron plasma waves caused by SRBS or SRFS excited by the 527 nm or 1053 nm laser. There is a large energy gap between the trappable energy ranges of SRBS and that of SRFS for the 527 nm laser. The electron kinetic energy in order to be trapped in electron plasma wave caused by SRFS of 527 nm is 680 keV. Since electron plasma wave caused by SRBS of 527 nm can only heat electrons less than 65 keV, staged heating cannot occur with only the primary 527 nm laser. Electron plasma waves excited by the secondary 1053 nm laser hand over electrons firstly heated by the wave caused by SRBS of the 527 nm laser to the wave caused by SRFS of the 527 nm laser. Thus, the enhancement of T_{hot} and η_{hot} using two-color laser irradiation can thus be explained qualitatively.

The electron temperature was unexpectedly increased, even with a relatively weak secondary 1053 nm laser with an intensity of 1.5×10^{12} W/cm^2(shot ID 40888). This intensity is clearly lower than the intensity threshold of SRS or TPD. The intensity threshold of TPD

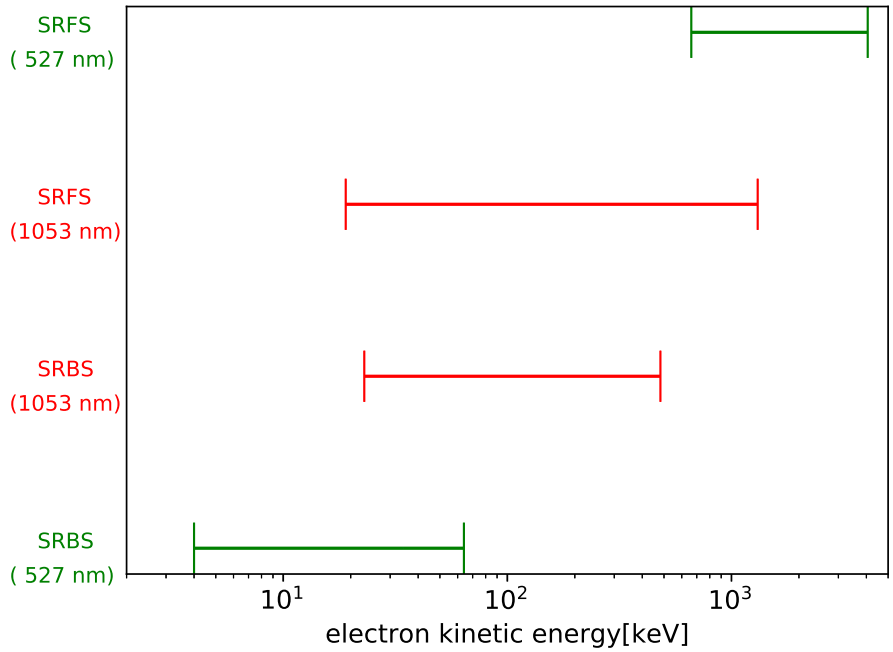

FIGURE 4.7: Kinetic energy ranges of trappable electrons in electron plasma waves caused by SRFS or SRBS excited by 527 nm and 1053 nm lasers. For the kinetic energy exceeding the rest energy of electron(511 keV), relativistic calculation was done.

with the 1053 nm laser is $I_{\mathrm{TPD}} = 8.2 T_{\mathrm{e}} L_{\mu\mathrm{m}}^{-1} \lambda_{\mu\mathrm{m}}^{-1} = 7.7 \times 10^{13}$ W/cm^2 [1]. The intensity threshold of SRS with the 1053 nm laser is $I_{\mathrm{SRS}} = 99.5 L_{\mu\mathrm{m}}^{-4/3} \lambda_{\mu\mathrm{m}}^{-2/3} = 2.4 \times 10^{14}$ W/cm^2 [24, 2]. Here, $L_{\mu\mathrm{m}}$, T_{e}, and $\lambda_{\mu\mathrm{m}}$ are the plasma scale length in micrometers, the electron temperature in electronvolts, and the laser wavelength in micrometers. $L_{\mu\mathrm{m}} = 90$ μm and $T_{\mathrm{e}} = 860$ eV were computed with the FLASH code. A significant reduction of the intensity threshold of LPPI may occur due to plasma wave sharing in the two-laser overlapped region.

Above discussion is more valid when the polarization crossing angle Θ_{cross} is closer to 90 °. In experiment, T_{hot} and η_{hot} are higher for $\Theta_{\mathrm{cross}} = 87^\circ$ than those for 1°. When the polarization crossing angle is close to 90°, two-color lasers do not interfere. Two-color lasers individually interact with plasmas and generate plasma waves by increasing the plasma density perturbation each other. When two-color lasers interfere, complex interference pattern emerges near n_{cr2} region. This interference pattern may smear out the plasma density perturbation generated near n_{cr2} region. This should be verified using a large scale three-dimensional particle-in-cell simulation.

4.7 Conclusion

In summary, experiments on the hot electrons generation using two-color laser irradiation were conducted with various experimental condition. The enhancements of the hot electron temperature and conversion efficiency were observed with the irradiation of 527 nm and 1053 nm lasers. Staged heating mechanism qualitatively explains the enhancements of the hot electron temperature and conversion efficiency. The co-existence of plasma waves caused by SRBS and SRFS of 527 nm and 1053 nm lasers at $n_e = 0.06\, n_{cr1}$ induce staged heating by sharing trappable electron energy ranges among plasma waves. One-dimensional analysis have been done in this article, while multi-dimensional correction should be considered. Experimentally measured hot electron half-spray angles with values of 40 $^\circ$ to 60 $^\circ$ suggest the existence of stimulated Raman side scattering and/or TPD. Stimulated Raman side scattering and TPD generate electron plasma waves having transverse phase velocity components which results in divergence of hot electrons. Finally, we emphasize that the two-color laser irradiation is a novel approach for efficient production of hot electrons and opens a new frontier of laser plasma interaction research.

Chapter 5

High energy density plasma generation using fast isochoric heating

The fast isochoric heating experiment was performed using nano-second laser pulse Gekko-XII and pico-second laser pulse LFEX. A cone attached solid fuel was compressed by the Gekko-XII. Near the maximum compression timing, the LFEX laser is irradiated on the target from the Au cone side. A relativistic electrons(REBs) are generated by the interactions between LFEX laser and pre-plasma. The REBs transmit their energy to the compressed core plasma through collisional manners. For an efficient HED plasma generation, the heating process should be understood. In this section, a process of HED formation observation will be introduced. From the experimental results, a conditions for generating further HED plasma will be presented.

For increasing the compression rate, we are using solid fuel consisted of low-Z materials like plastic(CH). A heated plasma have typically have a temperature of few keV. In such temperature, almost of ions are fully ionized. Fully ionized plasma can not generate a spectral X-ray lines, but a bremsstrahlung X-rays. Then it is difficult to evaluate the plasma properties. For exploring the properties of heated plasma, solid fuels containing 1 atomic wt% Cu ions were used. A He-like Cu emits X-ray spectral lines having energies 8.2 to 8.4 keV. A H-like Cu emits X-ray spectral lines having energies 8.5 to 8.7 keV. From the relation between maximum photon energy $E_{\max}$ and the plasma temperature T_e, for blackbody radiation $E_{\max} = 2.822T_e$, those X-rays have the maximum intensity when the plasma temperature is 2 to 3 keV.

A plasma temperature of compressed solid fuel is around 100 eV, a K_α emission imaging is a powerful tool for visualizing the energy deposition of REBs to the core. A K_α emission is due to the collision between REB and K-shell Cu, we can estimate the number of REBs because K-shell electron cross-section is well-known parameter by accumlumation of many studies,

5.1 Fast isochoric heating experiment W/O B-field

5.1.1 Density measurement

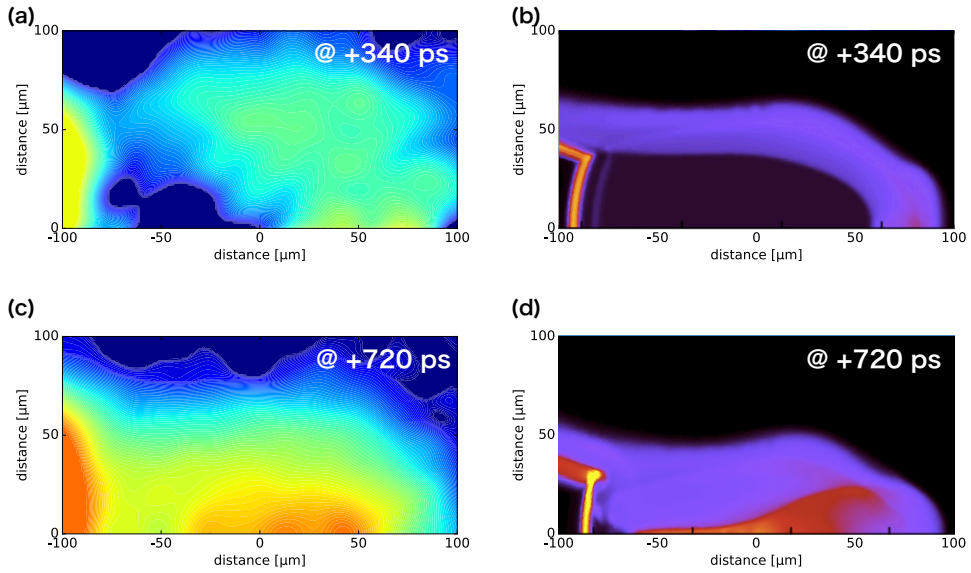

FIGURE 5.1

Firstly the density profiles were measured by flash Cu-K_α X-ray backlighting. The experimentally measured density profiles were compared with the 2D radiation hydrodynamic simulation results. Despite the experimental data is the compression with external magnetic field, the measured density profile is reproduced in simulation without magnetic field. So, here the influence of external magnetic field to the solid fuel compression is assumed to be low. The RAICHO was also used in this calculation which was well agree with the gaussian laser compression experiment showed in chapter 3. Fig. 5.1 shows the experimental data measured with 340 ± 45 ps after the compression laser peak timing and 720 ± 45 ps after the compression laser peak timing. At the time of 340 ps, the shock waves are not collide yet as shown in Fig. 5.1 (a). The 2D hydrodynamic simulation also agree with the experiment as shown in Fig. 5.1 (b). Still the shape in not completely reproduced. The different shape may be originated by the spatial intensity distribution, laser absorption and non-local effects. In this simulation code, no spatial distribution was considered. Only one-dimensional inverse-bremsstrahlung was calculated which may over-estimate the absorbed laser intensity. Fig. 5.1 (c) shows the density distribution near maximum compression timing. The simulation results as shown in Fig. 5.1 (d) agrees with

the experiment. The maximum density of 340 ps timing and 720 ps timing were 8 g/cc and 18 g/cc, respectively.

5.1.2 X-ray spectrum measurement

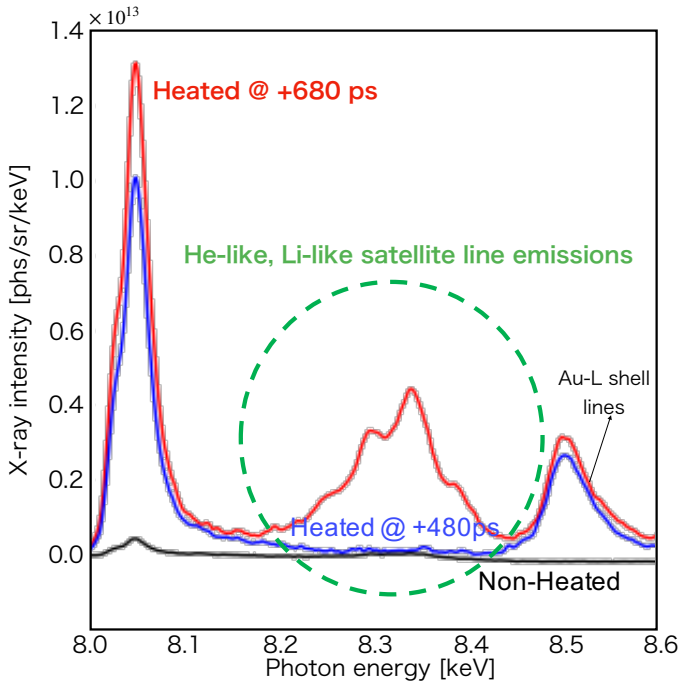

FIGURE 5.2

The X-ray spectrum emitted from the compressed and/or heated fuel were measured. The measured energy range is from 7.9 keV to 9.0 keV. Because the compressed plasma absorb the low energy X-rays, higher energy X-ray generated from Cu ions were selected. As an example, the transmittance of 4.51 keV to the compressed core was 0.2. While the transmittance of 8.048 keV X-ray at the timing of maximum compression was 0.7. The measured spectrum is shown in Fig. 5.2. The black line shows X-ray spectrum when only compressed by Gekko-XII. Only small amount of Cu-K_α X-ray was observed. It is due to the non-thermal electrons having few tens of keV kinetic energy, generated by laser plasma instabilities such as stimulated Raman scattering and/or two plasmon decay. Because the K-shell ionization energy of Cu is 8.949 keV, those non-thermal electrons can make the Cu ions inner-shell ionized state. No He-like and Li-like satellite X-ray were observed. When the LFEX laser heat the compressed plasma at

480 ps, which is before the maximum compression timing, we can observe strong Cu-K_α X-ray but still there is no X-rays from highly ionized Cu [1]. The He-like and Li-like satellite X-ray spectral lines were observed when the plasma was heated at 680 ps. If we assume the He-like and Li-like satellite X-ray line emissions at 480 ps were inside the noise, we can say that the X-ray intensity increased at least 100 times higher. It can be said that between those two timing, the heating efficiency were changed by some reasons.

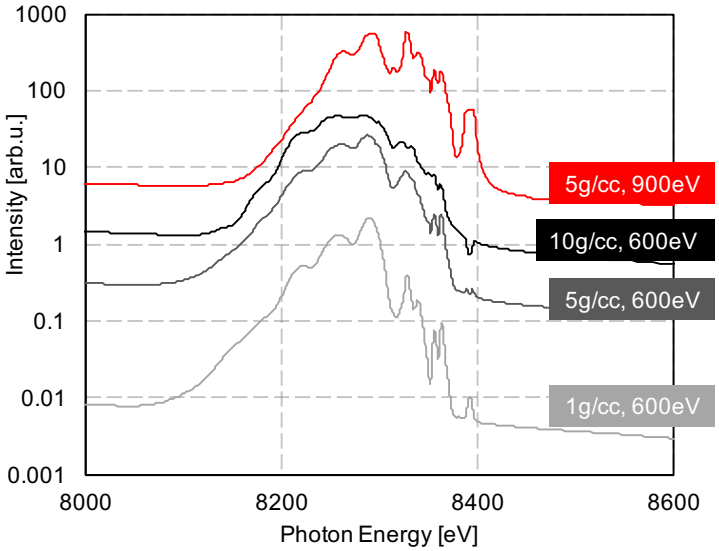

FIGURE 5.3

A difference between 480 ps and 680 ps is the plasma density. The plasma density near the REBs source increased at 680 compare to 480 ps. Due to the REBs have large divergence angle, it is physically correct to think that the temperature near the electron source is higher than the farther region. The density at 480 ps was 1 g/cc (non-compressed) and the density at 680 ps is 5 g/cc. We have the density distribution image at 720 ps, the 40 ps difference is too short time to shock wave. As an example, the typical shock velocity 10^6 cm/s propagate only 0.4 μm within 40 ps.

The Cu number increase affect to the X-ray signal intensity as shown in Fig. 5.3. Fig. 5.3 shows the simulated X-ray emission calculated by FLYCHK code. By comparing 1 g/cc, 600

[1] It is obvious that the number of He-like or Li-like Cu may exist more than that of compress only case. Many noises like hard X-rays, high energy particles and secondary electrons or X-rays are exist in fast isochoric heating environment. Especially, the secondary electrons and particles arrive to the detector after the X-ray signal, they may cause a de-excitation of excited the electron state of IP as signal. Which means they may 'erase' the X-ray signals. Here the issues on this will not discussed, but it should be taken measures.

eV case and 5 g/cc, 600 eV case, we can see the X-ray intensity increased about 5 times for spectral lines. The free-free component increase 25 times because the bremsstrahlung emission is proportional to the square of the number density. However, 100 times higher X-ray intensity can not explained just by the number increase. Temperature also should be increase with density increase. If you compare the 1g/cc, 600 eV case and 5g/cc, 900 eV case, it can be found that the X-ray intensity increased more than 100 times. The X-rays with energies from 8100 eV to 8400 eV is emitted by highly ionized Cu. Especially, we can see the strong He-α resonance($1s^1 2p^1(^1P) - 1s^2(^1S_0)$) line (8391 eV), the He-α intercombination($1s^1 2p^1(^3P) - 1s^2(^1S_0)$) line(8346 eV) and many Li-like Satellite lines.

The experimental data indicates that the increase of the density results in the increase of the plasma temperature. In general, the increase of mass density can increase the collisional energy coupling. The absolute number of particles also increase so that the energy per one particle should not be changed. However, considering the energy losses during heating process leads to the conclusion that an increase in density makes temperature increase.

5.1.3 Discussion

To understand the heating process, a simple heating model was used as follows.

$$P_{\text{input}} = P_{\text{deposit}}(t) - P_{\text{loss}}(t) \tag{5.1}$$

$$P_{\text{loss}}(t) = P_{\text{rad}}(t) + P_{\text{con}}(t) + P_{\text{hyd}}(t) \tag{5.2}$$

Here P_{input} is the increase of internal energy per unit time which is defined as the deposited energy per unit time minus energy loss per unit time.

There are several energy coupling precesses from REBs to the bulk plasma. Those are collisional heating, resistive heating and diffusive heating.

The collisional heating is the energy deposition through binary collisions among REBs and the background plasma. Due to the low cross-section, the plasma areal density should be much larger than the REB range to generate the localized hot spot. When the plasma areal density is same as the REB range, the ignition condition changes to the volume ignition condition. Then we need much higher temperature condition.

The resistive heating is Ohmic heating due to the return current induced by the REB potential. Due to the velocity of return current electron is much slower than REBs, those are collisional. As a result of collisions with return current electrons and the background plasma, the plasma heated up. Here we can think two different plasma density : a critical density and

the over solid density. The return current density j_r for both cases is same, with values of REB current density j_f. The deposited energy due to Ohmic heating is expressed as below.

$$E_{\mathrm{Ohm}} = \kappa_e j_r^2 \tag{5.3}$$

Here κ_e is the Spitzer resistivity. Due to κ_e is depend on only to the T_e, not the density, so that the deposited energy by Ohmic heating seems not depend on the plasma density. However, if we think a certain volume for those cases, the absolute number of electrons whose affected by the potential of REBs are completely different. Simply, 100 times difference of density results in the 100 times difference of return current electron number within same volume. Then the average electron energy of each cases are different. For example, the solid density DT plasma (ρ = 0.212 g/cc) is heated up by the return current having current density of 10^{13} [A cm^{-2}] to 1.7 keV. While the 100 g/cc DT plasma is heated up by same current density to only 3.4 eV. In our case, the Cu(II) Oleate plasma have much larger electron number than the DT plasma, the heating due to Ohmic heating can be negligible.

The diffusive heating should be considered because the corona plasma is heated up by the Ohmic heating which results in few tens of keV. The high temperature can heat up the core plasma by driving a heating wave to the direction of core plasma. So the diffusive heating also considered.

The collisional energy deposition were considered here. The energy deposition ratio was simplified as the areal density of the plasma divided by the average stopping range of electrons. The energy of REB is assumed to be 40 % of the laser energy which was measured parameter from experiment, and the slope temperature T_h of the electron was calculated with the ponder-motive scaling.

$$T_h = m_e c^2 \left(\sqrt{1 + \frac{I\lambda^2}{1.37 \times 1018}} - 1 \right) \tag{5.4}$$

Then the energy deposition per unit time is expressed as,

$$P_{\mathrm{loss}}(t) = 0.4 P_L \frac{l}{0,6T_h} \tag{5.5}$$

where, P_L, l, $0.6T_h$ is the laser power, the length of the cell, and the electron range of Beg scaling, respectively.

The energy loss per unit time P_{loss} is consisted of three process : radiation loss, conduction loss and the hydrodynamic loss. The radiation loss was used two radiation models :

bremsstrahlung radiation and blackbody radiation. The mathematical expression shows below.

$$P_{rad}(t) = \text{, (Bremsstrahlung radiation)} \tag{5.6}$$

$$P_{rad}(t) = \text{, (Blackbody radiation)} \tag{5.7}$$

Detailed calculation also was done using PrismSPECT code, which is collisional radiative atomic code for X-ray line emission calculation. The calculated emissivity and opacity were used in this model and will be shows in the last.

The conduction loss is expressed as below.

$$P_{con}(t) = \int \nabla \cdot (\kappa_e \nabla T) dV \tag{5.8}$$

By assuming one dimensional case,

$$P_{con}(t) = \kappa_e \frac{dT}{dx} S \tag{5.9}$$

Where κ_e and S is the thermal conductivity and the cross-section area, respectively. The Spitzer resistivity is used as κ_e.

$$\kappa_e = \frac{\pi Z_i e^{7/2} m_e^{1/2} \ln\Lambda}{(4\pi\varepsilon_0)^2 (T_e)^{3/2}} \tag{5.10}$$

Here the $\ln\Lambda$ is the Coulomb logarithm which is a factor for quantum correction term of binary collision and m_e, Z_i, T_e is the electron mass, average ion charge, and the electron temperature in eV, respectively. The strictly calculated Coulomb logarithm $\ln\Lambda$ is fitted divided by two regions for the convenient use, those are expressed as the following.

$$\ln\Lambda = 24 - \log\left(\frac{\rho}{m_i Z_i}\right)^2 \frac{Z_i}{T_e^{3/2}}, \ (T_e < 10 Z_i^2) \tag{5.11}$$

$$\ln\Lambda = 24 - \log\left(\frac{\rho}{m_i Z_i}\right)^2 \frac{1}{T_e}, \text{ (else)} \tag{5.12}$$

where the m_i is the ion mass.

The hydrodynamic loss is expressed as below.

$$P_{hyd}(t) = \int p \nabla \cdot u dV \tag{5.13}$$

By assuming one dimensional case,

$$P_{hyd}(t) = pu_{ex}S \tag{5.14}$$

Here, the p and u_{ex} is the pressure and expansion velocity.

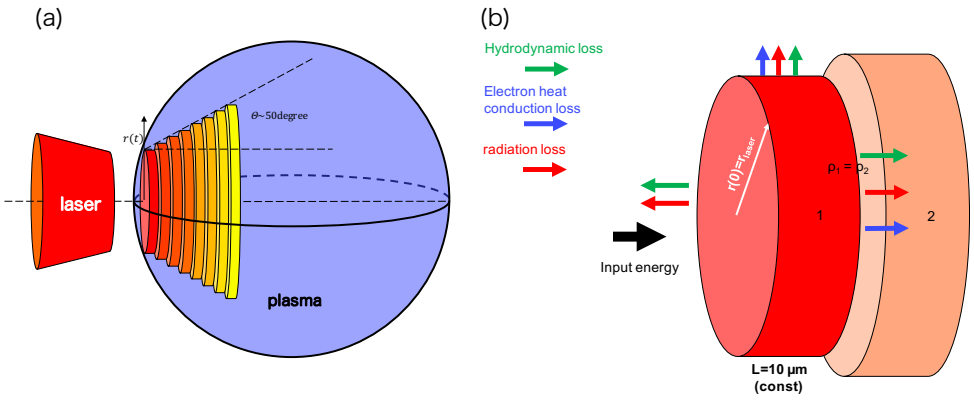

FIGURE 5.4: The image of one-dimensional heating model. An electron divergence and the diffusion due to from laser plasma interaction region is also considered here.

Fig. 5.4 shows the image of heating model. According to 2D hydrodynamic simulation result, the temperature of compressed plasma increase up to 100 eV. The initial temperature is set to 100 eV. For calculating the conduction loss, due to the temperature gradient dT/dx should be estimated. The temperature gradient was assumed from the spatial distribution of laser. A laser at focussed point have a Gaussian spatial distribution. From the laser intensity, the plasma temperature can be estimated, so that the temperature gradient dT/dx was calculated. The half divergence angle is assumed to be 50 °. The electron beam intensity decrease on the process of propagation due to divergence.

Fig. 5.5 shows the density dependence of temperature increase. For the plasma density of 1 g/cc case, the maximum temperature is 400 eV. The energy loss is being greater than the absorbed laser energy around 5 ps timing and from that time, the temperature start to decrease. A conduction energy loss is the main mechanism in this situation. When the plasma density 10 g/cc case, the maximum plasma density increased to 700 eV. The timing when the energy loss exceeding the absorbed laser energy is about 7 ps. This makes plasma temperature increase more than 1 g/cc case. The radiation energy loss increased about 100 times because

bremsstrahlung radiation is proportional to the square of density. It is important here that the conduction energy loss does not changed from 1 g/cc case. This is because the conduction energy loss does not affected by the plasma density, but only the temperature and temperature gradient. Also, 20 g/cc case, the plasma temperature reached near 800 eV which was measured in the experiment. From this, the experimentally measured X-ray spectrum difference between earlier timing and laser timing can be explained by the density effect. For earlier timing, the plasma was not compressed yet, thus the plasma density is 1 g/cc and in this case, the absorbed energy is small and conduction loss is the main energy loss factor. For later timing, the plasma was compressed to 10 g/cc, the absorbed energy increased 10 times compare to 1 g/cc case furthermore the conduction loss does not changed. And the X-ray spectrum in these cases was calculated before in Fig. 5.3. By comparing 1 g/cc 600 eV case and 5 g/cc 900 eV case, the He-like X-ray signal increases more than 100 times. For all cases, hydrodynamic energy loss was ignorable. Since the heating times is short enough for hydrodynamic motion, the isochoric heating was occur.

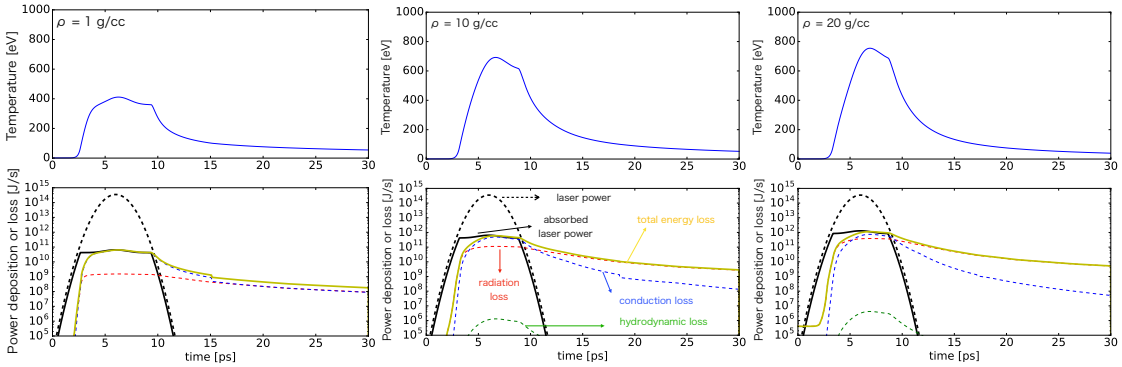

FIGURE 5.5: Density dependence of plasma heating process. Blue solid line shows the temperatue, black dashed line shows the laser pulse, black solid line shows the absorbed laser energy, red dashed line shows the radiation energy loss, blue dashed line shows the conduction energy loss, and the green dashed line shows the hydrodynamic energy loss.

The radiation is not always increasing with proportional to square of the density because of the re-absorption in the optically thick plasma. If the plasma is optically thick for all radiation energy, then the plasma can be assumed as black body. Here 100 g/cc plasma is set and the heating calculation was done with two radiation models : bremsstrahlung radiation, black body radiation. Fig. 5.6 shows the result of calculation. compare to Fig. 5.5, 100 g/cc case maximum temperature was less than 1,10, 20 g/cc cases due to strong radiation energy loss. The

maximum temperature of bremsstrahlung case was 600 eV while that of black body case was 1100 eV. The black body case, the radiation energy loss is significantly reduced compare to the bremsstrahlung case. Increasing the plasma density leads increasing of the plasma temperature. By these reasons, higher plasma density leads higher plasma temperature.

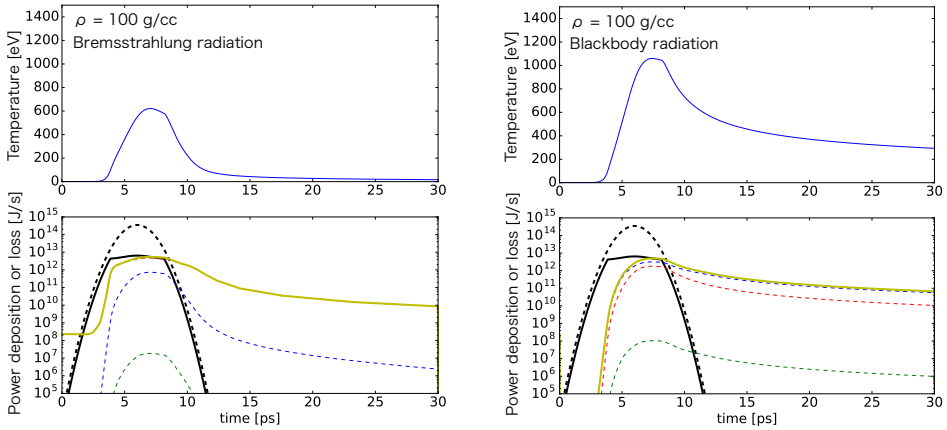

FIGURE 5.6: Radiation model dependence of plasma heating process. Blue solid line shows the temperatue, black dashed line shows the laser pulse, black solid line shows the absorbed laser energy, red dashed line shows the radiation energy loss, blue dashed line shows the conduction energy loss, and the green dashed line shows the hydrodynamic energy loss.

5.2 A guidance of REBs using external kT-class magnetic field

For achieving 5 keV plasma, not only the laser energy or plasma temperature, the REBs intensity is required. In this calculation, over 2×10^20 W/cm^2 was required for achieving the 5 keV plasma. Also, the laser pulse duration longer than 10 ps ls also required due the the time response for plasma heating. Due to the large divergence of REBs significantly degrade the REBs intensity, we applied external magnetic field to the direction of REBs propagation. The external magnetic field is generated by the laser driven capacitor coil. The magnetic field strength and the temporal evolution were measured by B-dot probing and also by the proton deflectometry. When the external magnetic field applied inside the plasma, the generated REBs can be confined with in the size of L_{conf} due to the gyro motion. L_{conf} is defined as $\sqrt{r_{\mathrm{Larmor}}^2 + r_L}$, where r_{Larmor} and r_L is the Larmor radius and Laser radius, respectively. To suppress the electron divergence within the laser spot size within the laser spot size, more than 100 T is necessary. According to

REF[25], a 700 T of magnetic field was measured using same capacitor coil. When the magnetic field strength is 700 T, $r_{\text{Larmor}} = 2.4\ \mu$m and r_L of LFEX laser is 25 μm. L_{conf} is then 25.1 μm. The electron beam intensity that we can obtain is 2.0×10^{19} W/cm^2 which is still small to generate 5 keV plamsa. Still, the electron beam guiding should be experimentally confirmed.

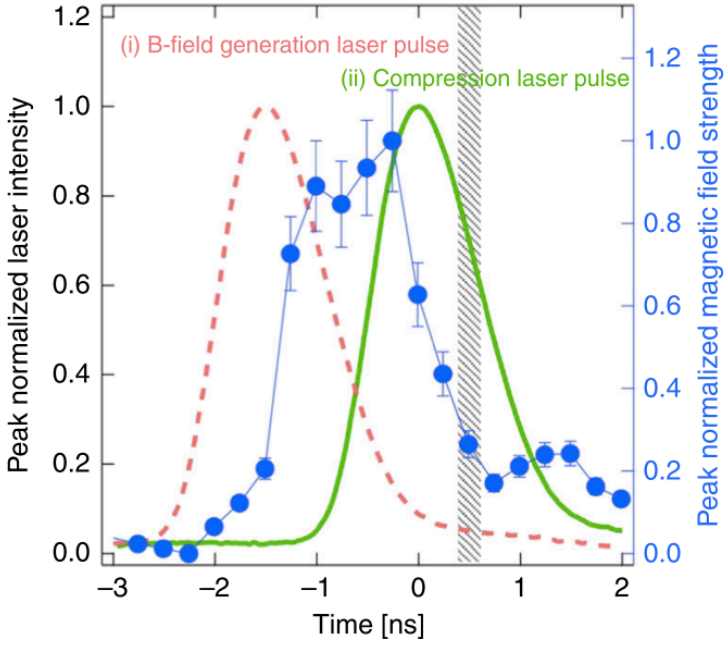

FIGURE 5.7

As a first demonstration of REB beam confining, we performed a fast isochoric heating experiment with external magnetic field. Fig. 5.7 shows the temporal evolution of magnetic field generated by the laser driven capacitor coil, compression laser pulse and capacitor driving laser pulse. The maximum magnetic field strength was 700 T and its timing is 1.2 ns after the capacitor coil driving laser peak timing. The Cu-K_α X-ray was measured using X-ray spectrometer with HOPG crystal. Due to Cu-K_α X-ray intensity is proportional to the REB number, we can estimated how many energy was deposited to the core plasma.

5.2.1 2D density distribution measurement

Flash Cu-K_α X-ray backlighting method was used to measure two-dimensional density profiles of compressed Cu(II) Oleate solid fuel applying an external magnetic field. The experimental layout is shown in Fig. 5.9. The X-ray radiograph image of compressed plasma were captured using IPs with spherically bent quartz(2131) crystal. The LFEX laser was used for generating

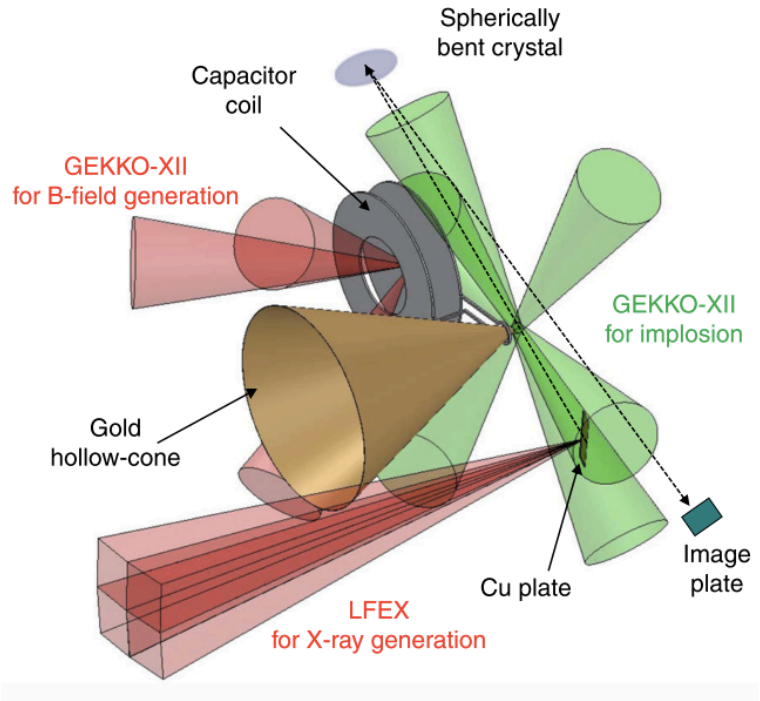

FIGURE 5.8

flash Cu-K_α X-ray. In order to generate a large amount X-rays, the LFEX laser was defocused to a 350 μm-diameter spot on a 20 μm-thick Cu foil, placed at 3 mm away from the solid ball along the line connecting the solid fuel and the crystal center. The areal density of the compressed fuel was calculated from the X-ray transmittance using an opacity of 100 eV temperature Cu(II) oleate for 8.05-keV X-rays. The plasma temperature is estimated using the 2D radiation hydrodynamic simulation code. A 2D density profile of the core was obtained after applying an inverse Abel transformation to the optical depth profile.

Fig. **??** shows the core density profiles at t=+0.38, +0.72, and +0.92 [ns]. Values on the contour lines represent mass density in the unit of [g cm^{-3}]. At the timing of t = +0.38 [ns], the converging shock wave is traveling toward the center of the fuel. The maximum compression timing is at around t = +0.72 [ns], and at the timing of t = +0.92 [ns] the plasma is expanding. Due to the difficulties to identifying the areal densities where REBs passed by, the areal densities ρ L of horizontal direction are averaged to the radial direction for using that values for the correlation factor calculation after. The values of areal densities at a certain time is are ρL=0.08 [g cm$^{?2}$] at t = + 0.38 [ns], ρL = 0.16 [g cm$^{?2}$] at t = + 0.72 [ns]. The average mass densities also averaged and those are ρ = 5.7 [g cm^{-3}] at t = + 0.38 [ns], ρ = 11,3 [g cm^{-3}] at t = + 0.72

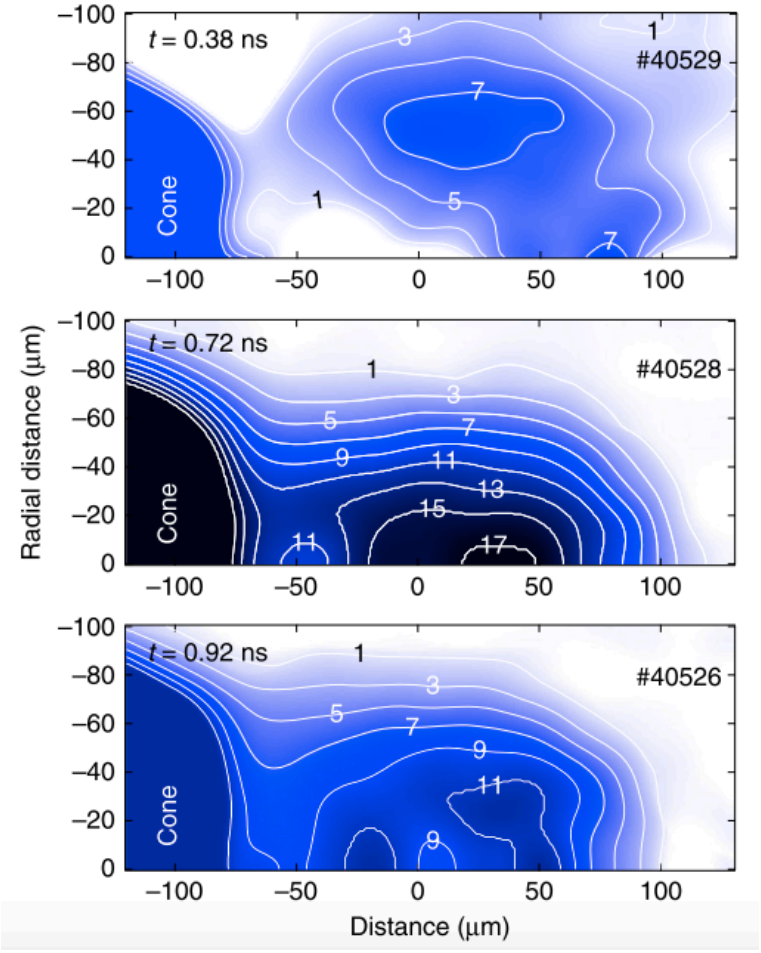

FIGURE 5.9: Experimentally measured density profile measured at 0.38 ns, 0.72 ns and 0.92 ns after the maximum intensity of compression laser Gekko-XII. The numbers on the contour lines shows the mass density in units of [g/cm^{-3}]

[ns].

5.2.2 Energy deposition distribution measurement

For visualizing the distribution of REBs energy deposition, Cu-K_α X-ray self-emission imaging were conducted. Fig. 5.10 shows the experimental layout. Six of Gekko XII laser beams were used for solid fuel compression, and three of Gekko XII laser beams were used for driving the capacitor coil. Near the maximum compression timing(0.72 ns) and before the compression timing(0.38 ns), the LFEX laser heat the core plasma. The self-emission of Cu-K_α X-ray is

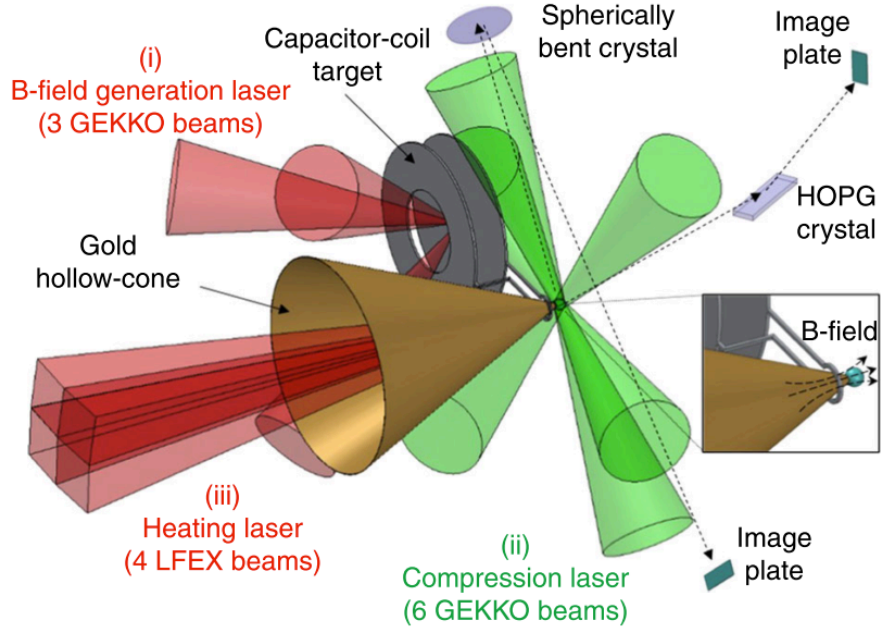

FIGURE 5.10: The schematic of the experimental layout for electron beam guiding experiment. Six of Gekko XII laser beams were used for solid fuel compression, and three of Gekko XII laser beams were used for driving the capacitor coil. A spherically bent mirror was used for imaging the self-emission of Cu-K_α emission, which has an information of the REBs number and distribution.

imaged by the spherically bent Quartz crystal and detected by the Fuji BAS-SR IPs. The heating timing was measured by XSC.

5.2.3 Correlation model between Cu K_α photons and electrons

For estimating the laser to core coupling efficiency, There are several K-shell ionization cross-section empirical models. Here the two K-shell ionization cross-section empirical models will be used which was introduced by Hombourger and Davies.

Hombourger formula

Hombourger(1998) proposed the cross-section of Cu K-shell electron impact ionization by the following expression[17]. This formula has a good agreement with experiments in the range of $1<U<10^4$, where U is over voltage which is defined as electron energy E divided by binding

energy of K-shell electron B_K, $U = E/B_K$.

$$\sigma_K = N_K \pi {a_B}^2 G_r \left(\frac{R_y}{B_K}\right)^{C_U} D_U, \tag{5.15}$$

$$G_r = \left(\frac{1+2J}{U+2J}\right)\left(\frac{U+J}{1+J}\right)^2 \left(\frac{(1+U)(U+2J)(1+J)^2}{J^2(1+2J)+U(U+2)(1+J^2)}\right)^{1.5}, \tag{5.16}$$

$$D_U = \left(3.125 - \frac{4.172}{U} + \frac{1.877}{U^2}\right)\frac{\ln(U)}{U}, \tag{5.17}$$

$$C_U = \left(2.0305 - \frac{0.3160}{U} + \frac{0.1545}{U^2}\right)\frac{\ln(U)}{U}, \tag{5.18}$$

where N_K, a_B, R_y is the number of K-shell electrons, the Bohr radius, the Rydberg energy (13.606eV), respectively.

The electron at the state of 2p of K-shell ionized state Cu will be de-excited to 1s, then Cu-K_α photons are generated. Also there are lots of emissions generated from K-shell ionized state Cu. For example, not only the K-shel lines but also L-shell and M-shell lines also emitted. The possibility of K_{shell} x-ray photon generation is proportional to the fluorescence yield f_K, which is a value of $f_K = 0.433$[18]. K-shell photon emission cross-section then will be expressed by the following.

$$\sigma_{Kph} = \sigma_K f_K. \tag{5.19}$$

Davies formula

Davies(2013) suggested the empirical model of Cu K-shell emission by electron impact ionization[8]. This model has 10% of error for all published experimental data.

$$\sigma_{Kph} = \left(1 - \frac{0.2824}{U}\right)\frac{20.95}{\beta^2} ln\left[\left(\frac{U+113.8}{114.8}\right)^{0.5}\frac{57.0098U}{56.9+0.1098U}\right] \tag{5.20}$$

Cu K_α photon intensity

Probability of K_α photon numbers per unit time per unit volume per unit solid angle $P_{K\alpha}(E)$ $[\mathrm{ph}/(\mathrm{sr}\cdot\mathrm{s}\cdot\mathrm{cm}^3)]$ from Cu due to REB is

$$P_{K\alpha}(E) = \frac{\phi_{REB}(E)\cdot n_{Cu}\cdot\sigma_{K\alpha}(E)}{4\pi} = \frac{\phi_{REB}(E)\cdot\rho\cdot F_{Cu}\cdot\sigma_{K\alpha}(E)}{4\pi\cdot m_p\cdot A_{Cu}}, \tag{5.21}$$

with the values $F_{\mathrm{Cu}} = 0.1014$ mass fraction of copper ions in the fuel, $m_{\mathrm{p}} = 1.672 \times 10^{-24}$[g] mass of proton, $A_{\mathrm{Cu}} = 63.54$ atomic number of copper ion. Where ρ is mass density of Cu(II) Oleate. Also, it was assumed that the K_α photons are emitted isotropically.

Here, only Cu-K_α photons will be discussed. The probability of K_α photon emission f_{K_α} from K-shell ionized ions is 0.880. The cross-section of Cu-K_α photon emission can be expressed $\sigma_{K_\alpha} = \sigma_{\mathrm{Kph}} f_{K_\alpha}$.

5.2.4 Energy deposition in the plasma

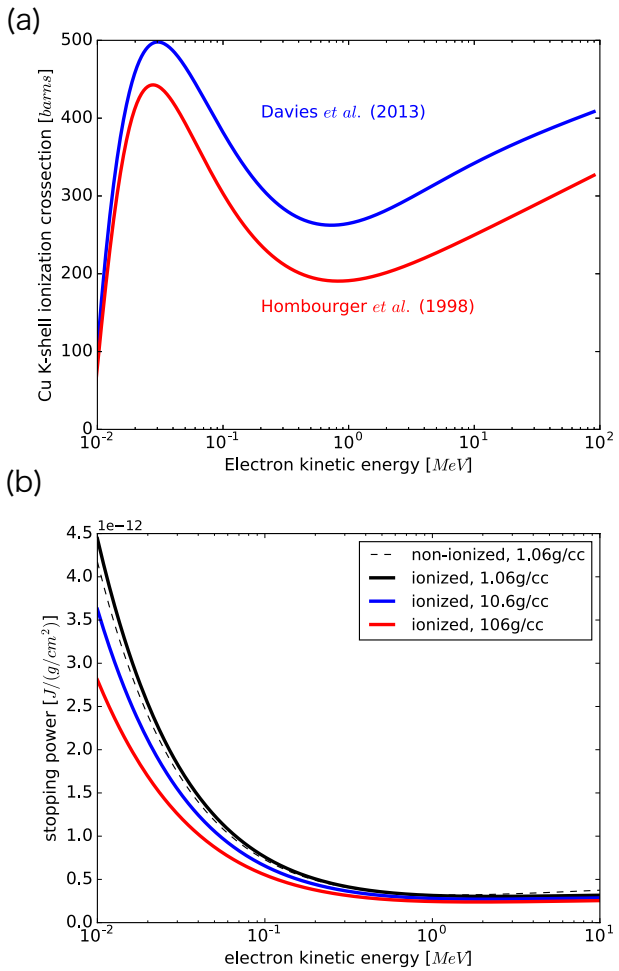

FIGURE 5.11: (a) Empirical K-shell impact ionization cross-section models by Hombourger(1998) and Davies(2013). Here, we used both models for a calculation of correlation parameter. (b) Electron mass stopping power in Copper(II) Oleate.

Here the collisional heating will be considered. The collisional stopping power of Solodov and Betti formula[48] was used here.

$$S_{\mathrm{n}}(E) = \frac{2\pi {r_0}^2 m_{\mathrm{e}} c^2 n_{\mathrm{e}}}{\rho\beta^2}\left\{ ln\left[\left(\frac{E}{I}\right)^2 \frac{\gamma+1}{2}\right] + \frac{1}{\gamma^2} + \frac{1}{8}\left(\frac{\gamma-1}{\gamma}\right)^2 - \left(\frac{2\gamma-1}{\gamma^2}\right)\ln 2 - \delta \right\}, \tag{5.22}$$

$$S_{\mathrm{i}}(E) = \frac{2\pi {r_0}^2 m_{\mathrm{e}} c^2 n_{\mathrm{e}}}{\rho\beta^2}\left\{ ln\left[\left(\frac{E}{\hbar\omega_{\mathrm{p}}}\right)^2 \frac{\gamma+1}{2\gamma^2}\right] + 1 + \frac{1}{8}\left(\frac{\gamma-1}{\gamma}\right)^2 - \left(\frac{2\gamma-1}{\gamma^2}\right) ln2 \right\}, \tag{5.23}$$

where I is the mean excitation energy of the medium and δ is the density-effect correction. Calculated results of stopping energy inside Cu(II) Oleate with various densities are shown in the Fig. 5.11 (b).

5.2.5 Correlation between REB energy deposition and Cu-K_α X-ray yield

The REB number density per unit time per unit cross-section is defined as ϕ_{REB} and expressed as the following.

$$\phi_{\mathrm{REB}}(E) = v(E) \cdot n_{\mathrm{REB}}, \tag{5.24}$$

where $v(E)$, n_{REB} are velocity of REB with its kinetic energy E and number density, respectively.

Deposited energy by REB

Deposited energy per unit time per unit volume by REB $\varepsilon_{\mathrm{dep}}(E)$ can be expressed like,

$$\varepsilon_{\mathrm{dep}}(E) = \phi_{\mathrm{REB}}(E) \cdot \rho \cdot S(E), \tag{5.25}$$

where $S(E)$ is mass stopping power [J/(g/cm^2)].

Correlation parameter calculation

We propose a parameter which is defined as the deposited energy divided by the Cu-K_α photon yields. The the production of the correlation parameter and the experimentally measured total Cu-K_α photon, we can estimate the deposited energy. The REB have a distribution function and depending on the electron energy, energy deposition and Cu-K_α yield is different. By the integration of the energy deposition and Cu-K_α yield with electron energy from 0 to the infinity, we can get correlation parameter which means averaged energy deposition per one

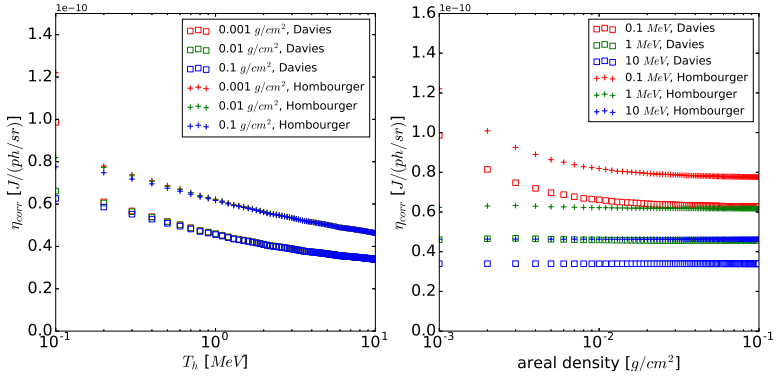

FIGURE 5.12: Areal density dependence of correlation parameter η_{corr} with a given T_{h}(left). REB Temperature dependence of correlation parameter η_{corr}(right). One can find that the correlation parameter η_{corr} is not sensitive to the areal density where REB passed by if $T_{\mathrm{h}} \geq 1$MeV.

Cu-K_α photon. Correlation parameter $\eta_{\mathrm{corr}}[J/(ph/sr)]$ can be defined as the following.

$$\eta_{\mathrm{corr}} = \frac{\varepsilon_{\mathrm{dep,total}}}{P_{\mathrm{K}\alpha,\mathrm{total}}} = \frac{\int \varepsilon_{\mathrm{dep}}(E)\cdot f(E)\cdot dE}{\int P_{\mathrm{K}\alpha}(E)\cdot f(E)\cdot dE}, \tag{5.26}$$

$$= \frac{4\pi\cdot m_{\mathrm{p}}\cdot A_{\mathrm{Cu}}}{F_{\mathrm{Cu}}}\frac{\int v(E)\cdot \exp(-E/T_{\mathrm{h}})\cdot S(E)\cdot dE}{\int v(E)\cdot \exp(-E/T_{\mathrm{h}})\cdot \sigma_{\mathrm{K}\alpha}(E)\cdot dE}, \tag{5.27}$$

where $f(E)$ is electron number per unit electron kinetic energy which has single-temperature Maxwell distribution function.

Fig. **??** shows the calculated correlation parameter η_{corr} which is the function of T_{h} and ρL of the core plasma. One can see that η_{corr} decreases when the REB temperature increases. This is because the electron energy dependence of stopping power is more sensitive than that of Cu-K_α emission cross-section. As you can see in the Fig. **??**, Cu-K_α emission cross-section have a peak value near 24 keV electron kinetic energy. The cross-section decreases to 1 MeV of electron energy because of the short coulomb collision time. And increase again because of the relativistic effect. The decrease of cross-section is only a factor of 2. While the stopping power have 10 times different values within the electron kinetic energy range of $10^{-2} \sim 10^{1}$MeV.

In this experiment, T_{h} was measured to be in the range of 0.8 to 4 [MeV]. The areal density of the plasma where hot elecctron passed by is difficult to decide because it was not measured. Here, we assume that all electrons were passed the fuel with parallel direction of the heating laser. Then, the areal density is in the range of 0.03 to 0.1 [g/cm^2]. η_{corr} contour map which is calculated using values measured in the experiment. Then, η_{corr} is in the range of $3.40 \sim 3.90\times$

10^{-11}[J/(ph/sr)](Davies formula) and $4.63 \sim 5.36 \times 10^{-11}$[J/(ph/sr)](Hombourger formula).

In our model, it is impossible to ignore areal density dependence of η_{corr}, because we have no information where the REB passed by. If you see figure.5, however, areal density dependence of η_{corr} can be negligible if $T_{\mathrm{h}} \geq 1$MeV. Also, in our experiment, T_{h} was measured to be 0.8 to 4 [MeV] which satisfy the above condition.

Still density dependency of stopping power can not be ignored which has an error of $\pm 5\%$. This error comes from uncertainty of the fuel mass where each energy of REB passed by. Finally, η_{corr} is in the range of $(3.53 \sim 4.45 \pm 5.5\%) \times 10^{-11}$ [J/(ph/sr)] (Davies formula) and $(4.87 \sim 6.00 \pm 5.5\%) \times 10^{-11}$ [J/(ph/sr)] (Hombourger formula).

REBs spectrum with 1 temperature, passing through 7μm gold

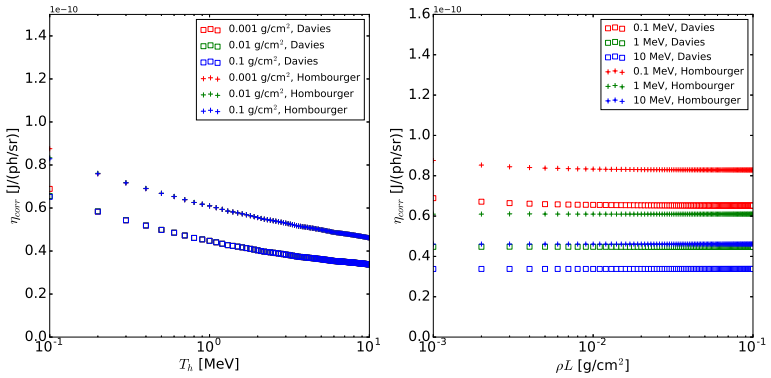

FIGURE 5.13: Correlation parameter η_{corr} calculated by electron spectrum passed through 7 μm thick gold filter. Areal density dependence of correlation parameter η_{corr} with a given T_{h}(left). REB Temperature dependence of correlation parameter η_{corr}(right).

The spectrum of REBs should be calculated for arbitrary distribution because the electron distribution is not always Maxwellian. Here one case will be shown. When the heating laser interact with high-Z material like Au, the REBs have to transport through the high-Z material. The lower energy components of REBs reduced due to strong attenuation inside the high-Z material, it should be considered. The calculated results will be shown in Fig. 5.13. Using a modified distribution function of REBs by the 7 μm Au stopping power, the integration of Cu-K_α emission and deposition of energy were conducted. When the REBs T_e is 200 keV, the correlation parameter decreased only 7 %. While the T_e is 100 keV, the correlation parameter decreased about 30 %. However, the typical T_e is about 1 MeV, thus the existence of 7 μm Au is ignorable.

Discussion

TABLE 5.1: Summary of laser to core coupling efficiencies

Shot ID	Heating energy [J]	Heating timing [ps]	Cu-K_α yield [ph/sr]	Coupling efficiency [%]
#40545	899	420	5.58×10^11	2.9 ± 0.5
#40541	683	650	5.53×10^11	3.9 ± 0.6
#40558	1516	400	1.19×10^12	3.1 ± 0.5
#40556	1016	610	1.02×10^12	4.3 ± 0.7
#40547	1100	380	1.28×10^12	5.5 ± 0.9
#40549	668	370	7.29×10^11	5.8 ± 0.9
#40543	625	720	9.32×10^11	7.7 ± 1.2

Using the modeled correlation parameter and experimentally measured Cu-K_α yield, the energy coupling efficiency from laser energy to the core plasma were estimated. One can see that the coupling efficiency increased about 2.0 times by applying the external magnetic field by comparing shot ID 40541 and 40543. This means that the REBs are effectively guided to the core plasma. Furthermore, the coupling efficiency is degraded by increasing the heating laser energy. This is because the higher heating laser intensity produces higher temperature REBs. The higher energy of REB decreased the energy deposition.

In this experiment, the electron beam intensity was not enough to generate 5 keV temperature plasma. For achieving higher electron beam intensity, 10 times higher laser energy is required. However, if laser energy increase, laser intensity is also increase. The experimental data shows that the increase of laser intensity decrease the energy coupling. Thus we should increase the laser energy without increasing laser intensity. Then we have two choices, increasing spot size or increasing pulse duration. Preliminary research[39] shows that the increasing pulse duration is the best choice for FI.

In this section, we have demonstrated experimentally fast isochoric heating method with and without external magnetic field for generating HED plasma. At without fast isochoric heating experiment, it was proved by using simple heating model that the electron temperature of the core plasma can be increased by increasing plasma density. In the process of low density plasma heating, conduction loss is the main energy loss. The conduction loss is not determined by the density, when the density increased, the plasma temperature also increased. The radiation re-absorption is also important message. The denser core plasma is necessary to increase the plasma temperature efficiently. In external magnetic field applied experiment, the coupling

efficiency was estimated by using correlation model. The enhancement of the coupling from the laser to core is the evidence of effective REB guiding with the external magnetic field. This result shows that the external magnetic field is applicable for increasing the laser to core energy coupling.

Chapter 6

Conclusion

In this study, a new high energy density plasma generation method by high-intensity laser was experimentally investigated by spatio-temporal-resolved and spectral-resolved measurement of X-ray spectrum. A new fuel for fast ignition, a solid fuel was suggested in this research. A spherical shell fuel used in conventional laser fusion scheme, the hydrodynamic instability, especially the Rayleigh-Taylor instability degrade the compression ratio. Many researches on Rayleigh-Taylor instability have been performed to understand and suppressing that. Go back to the initial laser fusion design, the first ignition target was solid fuel. Due to the limitation of hot spot generation using solid fuel, the shape of the fuel is changed to the spherical shell. In fast ignition scheme, the fuel compression and heating process is divided. Which mean that in the compression process, we do not need to make hot spot. There is no reason for using spherical shell target in fast ignition. A solid fuel is hydrodynamically stable than the spherical shell. In the compression process of a spherical shell fuel, the spherical shell is accelerated for a long time on a hydrodynamically unstable state. While in the compression process of a solid fuel, it is only subjected to instantaneous acceleration by a shock wave. Increase in distortion in solid fuel due to hydrodynamic instability is relatively smaller than spherical shell fuel. In the experiment, a solid sphere is compressed with a high-intensity laser, and a short pulse high-intensity laser is irradiated to a thin metal foil to generate a short pulse of K_α X-ray. An X-ray is imaged using a spherically curved crystal and X-ray transmittance image with high spatial resolution (Δx = 10 μm) and high temporal resolution (Δt = 1 ps) was recorded on the imaging plate. In this experiment, no spatial smoothing techniques was used for the laser. Furthermore, the experiment was performed in d/R = -3 laser irradiation condition which the intensity non-uniformity is over 50 %. The shadow of the fuel were observed stably using solid fuel. The maximum areal density 0.87 $\pm$ 0.24 g/cm^2 and the maximum density 26 g/cc was obtained.

For increasing the compression ratio, the shock pressure should be increased. However, over 10^15 W/cm^2 intensity makes laser absorption low and too large power is a source of the laser optics damage. To avoid this, shock pressure enhancement using high energy electron

is necessary. In the conventional shock wave generation method, the shock wave is driven by laser ablation pressure. The laser deposit its energy near the critical density, 2 to 3 digits lower than the solid density. While a high energy electrons can deposit their energy directly to the over-solid density. The pressure of shock wave can be increased by absorbing high energy electrons behind the shock front. A new method for efficient generation of high energy electron is studied. We have demonstrated the efficient production of non-thermal hot electrons by interaction between a long-scale pre-plasma and two-color lasers with wavelengths of 527 and 1053 nm. The two-color laser-plasma interaction caused a 4.8 times enhancement of the hot electron temperature and a 2.7 times enhancement of energy conversion from lasers to hot electrons compared with that obtained with only a 527 nm laser. These experimental results can be explained by a staged electron heating occurs near one-sixteenth critical density of the 527 nm laser which is correspond to quarter critical density of the 1053 nm laser. The primary 527 nm laser excites electron plasma waves which a gap between their trappable electron energies is large. Electron plasma waves excited by the secondary 1053 nm laser fill that gap, therefore, staged electron heating realized with a mixture of two-color lasers. Some of the background thermal electrons can be heated to several hundred keV through staged heating. The two-color laser irradiation is a novel approach for efficient production of hot electrons and opens a new frontier of laser plasma interaction research.

The plasma temperature generated only by the compression is low. Therefore, we aimed to generate HEDP by irradiating high intensity laser and heating low temperature and high density plasma within tens of picoseconds in which the compressed plasma maintains high density state by its inertia. A high intensity laser pulse is irradiated to the plasma to accelerate the relativistic electron beam and heat the high density plasma with this relativistic electron beam. Since the relativistic electron beam has a large divergence angle, the beam intensity drops sharply while propagating from the generation point to the fuel. We proposed the idea of guiding relativistic electrons to the fuel by applying an external magnetic field parallel to the propagation direction of the heating laser. Visualization of the heating region and diagnosis of the heating efficiency were carried out using Cu-K_α X-ray imaging techniques and measuring absolutely calibrated X-ray spectroscopy of Cu-K_α radiation. A Cu ion contained solid sphere was used in this experiment. It is experimentally showed that the heating efficiency increased 2 times by applying an external magnetic field,

This research has succeeded in proposing and demonstrating a novel method, which is completely different from the conventional method in high density plasma generation and high density plasma heating. This result will greatly contribute to the development of future high energy density scientific research.

Bibliography

[1] Bedros B. Afeyan and Edward A. Williams. “A variational approach to parametric instabilities in inhomogeneous plasmas II: Stimulated Raman scattering”. In: *Physics of Plasmas* 4.11 (1997), pp. 3803–3826.

[2] Bedros B. Afeyan and Edward A. Williams. “A variational approach to parametric instabilities in inhomogeneous plasmas III: Two-plasmon decay”. In: *Physics of Plasmas* 4.11 (1997), pp. 3827–3844.

[3] Raymond Brusasco, Michael Saculla, and Robert Cook. “Preparation of germanium doped plasma polymerized coatings as inertial confinement fusion target ablators”. In: *Journal of Vacuum Science & Technology A* 13.3 (1995), pp. 948–951. DOI: 10.1116/1.579656.

[4] W. Chester. “CXLV. The quasi-cylindrical shock tube”. In: *The London, Edinburgh, and Dublin Philosophical Magazine and Journal of Science* 45.371 (1954), pp. 1293–1301. DOI: 10.1080/14786441208561138.

[5] R. F. Chisnell and Michael James Lighthill. “The normal motion of a shock wave through a non-uniform one-dimensional medium”. In: *Proceedings of the Royal Society of London. Series A. Mathematical and Physical Sciences* 232.1190 (1955), pp. 350–370. DOI: 10.1098/rspa.1955.0223. URL: https://royalsocietypublishing.org/doi/abs/10.1098/rspa.1955.0223.

[6] C. Courtois et al. “Creation of a uniform high magnetic-field strength environment for laser-driven experiments”. In: *Journal of Applied Physics* 98.5 (2005). ISSN: 00218979.

[7] H. Daido et al. “Generation of a strong magnetic field by an intense CO2 laser pulse”. In: *Physical Review Letters* 56.8 (1986), pp. 846–849. ISSN: 00319007.

[8] J. R. Davies et al. “Copper K-shell emission cross sections for laser–solid experiments”. In: *Physics of Plasmas* 20.8 (2013), p. 083118. DOI: 10.1063/1.4819721.

[9] R. Decoste et al. “Reduction of the hot electron energies with increasing pulse rise time in CO2-laser–target interaction”. In: *The Physics of Fluids* 30.9 (1987), pp. 2898–2902.

[10] J. F. Drake et al. “Parametric instabilities of electromagnetic waves in plasmas”. In: *Physics of Fluids* 17.4 (1974), pp. 778–785. ISSN: 00319171.

[11] J. R. Fein et al. “Mitigation of hot electrons from laser-plasma instabilities in high-Z, highly ionized plasmas”. In: *Physics of Plasmas* 24.3 (2017), p. 032707.

[12] Gennady Fiksel et al. “A simple model for estimating a magnetic field in laser-driven coils”. In: *Applied Physics Letters* 109.13 (2016), pp. 1–5. ISSN: 00036951.

[13] B. Fryxell et al. “FLASH: An Adaptive Mesh Hydrodynamics Code for Modeling Astrophysical Thermo-nuclear Flashes”. In: *The Astrophysical Journal Supplement Series* 131.1 (2000), pp. 273–334.

[14] Shinsuke Fujioka et al. “Kilotesla magnetic field due to a capacitor-coil target driven by high power laser.” In: *Scientific reports* 3 (2013), p. 1170. ISSN: 2045-2322.

[15] Shinsuke Fujioka et al. “Suppression of Rayleigh–Taylor instability due to radiative ablation in brominated plastic targets”. In: *Physics of Plasmas* 11.5 (2004), pp. 2814–2822. DOI: 10.1063/1.1705654.

[16] B. L. Henke, J. P. Knauer, and K. Premaratne. “The characterization of x-ray photocathodes in the 0.1 - 10 keV photon energy region”. In: *Journal of Applied Physics* 52.3 (1981), pp. 1509–1520. ISSN: 00218979. DOI: 10.1063/1.329789.

[17] C Hombourger. “An empirical expression for K-shell ionization cross section by electron impact”. In: *Journal of Physics B: Atomic, Molecular and Optical Physics* 31.16 (1998), pp. 3693–3702. DOI: 10.1088/0953-4075/31/16/020. URL: https://doi.org/10.1088%2F0953-4075%2F31%2F16%2F020.

[18] A. Kahoul et al. “K-shell fluorescence yields for elements with 6Z99”. In: *Radiation Physics and Chemistry* 80.3 (2011), pp. 369 –377. ISSN: 0969-806X. DOI: https://doi.org/10.1016/j.radphyschem.2010.11.011. URL: http://www.sciencedirect.com/science/article/pii/S0969806X10004408.

[19] Y. Kato et al. “Random Phasing of High-Power Lasers for Uniform Target Acceleration and Plasma-Instability Suppression”. In: *Phys. Rev. Lett.* 53 (11 1984), pp. 1057–1060. DOI: 10.1103/PhysRevLett.53.1057. URL: https://link.aps.org/doi/10.1103/PhysRevLett.53.1057.

[20] R E Kidder. “Theory of homogeneous isentropic compression and its application to laser fusion”. In: *Nuclear Fusion* 14.1 (1974), p. 53. ISSN: 17414326. DOI: 10.1088/0029-5515/14/1/008. URL: http://stacks.iop.org/0029-5515/14/i=1/a=008.

[21] J. P. Knauer et al. “Improved target stability using picket pulses to increase and shape the ablator adiabat”. In: *Physics of Plasmas* 12.5 (2005), p. 056306. DOI: 10.1063/1.1882332.

[22] Koga, M. et al. “High-resolution X-ray imaging in fast ignition experiment using Gekko and LFEX lasers”. In: *EPJ Web of Conferences* 59 (2013), p. 03006. DOI: 10.1051/epjconf/20135903006. URL: https://doi.org/10.1051/epjconf/20135903006.

[23] T. Kolber, W. Rozmus, and V. T. Tikhonchuk. “Saturation of backward stimulated Raman scattering and enhancement of laser light scattering in plasmas”. In: *Physics of Plasmas* 2.1 (1995), pp. 256–273.

[24] William Kruer L. “The Physics of Laser Plasma Interactions”. In: Westview Press, University of California, Los Angeles, 2003.

[25] K. F. F. Law et al. “Direct measurement of kilo-tesla level magnetic field generated with laser-driven capacitor-coil target by proton deflectometry”. In: *Applied Physics Letters* 108.9 (2016), p. 091104. DOI: 10.1063/1.4943078.

[26] C. S. Liu, Marshall N. Rosenbluth, and Roscoe B. White. “Raman and Brillouin scattering of electromagnetic waves in inhomogeneous plasmas”. In: *Physics of Fluids* 17.6 (1974), pp. 1211–1219. ISSN: 10706631.

[27] J.J. MacFarlane, I.E. Golovkin, and P.R. Woodruff. “HELIOS-CR – A 1-D radiation-magnetohydrodynamics code with inline atomic kinetics modeling”. In: *Journal of Quantitative Spectroscopy and Radiative Transfer* 99.1 (2006). Radiative Properties of Hot Dense Matter, pp. 381 –397. ISSN: 0022-4073. DOI: https://doi.org/10.1016/j.jqsrt.2005.05.031. URL: http://www.sciencedirect.com/science/article/pii/S0022407305001627.

[28] D. T. Michel et al. “Measured hot-electron intensity thresholds quantified by a two-plasmon-decay resonant common-wave gain in various experimental configurations”. In: *Physics of Plasmas* 20.5 (2013), p. 055703.

[29] R. M. More et al. “A new quotidian equation of state (QEOS) for hot dense matter”. In: *The Physics of Fluids* 31.10 (1988), pp. 3059–3078. DOI: 10.1063/1.866963.

[30] W B Mori and T Katsouleas. “Wavebreaking of longitudinal plasma oscillations”. In: *Physica Scripta* T30 (1990), pp. 127–133.

[31] M. Murakami, J. Sanz, and Y. Iwamoto. “Stability of spherical converging shock wave”. In: *Physics of Plasmas* 22.7 (2015), p. 072703. DOI: 10.1063/1.4923437.

[32] Ph. Nicolaï et al. “Deleterious effects of nonthermal electrons in shock ignition concept”. In: *Physical Review E* 89.3 (2014), p. 033107. ISSN: 1539-3755.

[33] Ph. Nicolaï et al. “Effect of nonthermal electrons on the shock formation in a laser driven plasma”. In: *Physics of Plasmas* 22.4 (2015), p. 042705. ISSN: 1070-664X.

[34] John Nuckolls et al. “Laser Compression of Matter to Super-High Densities: Thermonuclear (CTR) Applications”. In: *Nature* 239.5368 (1972), pp. 139–142. ISSN: 0028-0836. DOI: 10.1038/239139a0.

[35] Naofumi Ohnishi. “Toward an accurate numerical simulation of radiation hydrodynamics in laser ablation plasmas”. In: *High Energy Density Physics* 8.4 (2012), pp. 341 –348. ISSN: 1574-1818. DOI: https://doi.org/10.1016/j.hedp.2012.09.003. URL: http://www.sciencedirect.com/science/article/pii/S1574181812001000.

[36] Harvey A. Rose. “Random phase plate hot spots and their effect on stimulated Brillouin backscatter and self-focusing”. In: *Physics of Plasmas* 2.6 (1995), pp. 2216–2223. DOI: 10.1063/1.871244.

[37] Marshall N. Rosenbluth. “Parametric instabilities in inhomogeneous media”. In: *Physical Review Letters* 29.9 (1972), pp. 565–567. ISSN: 00319007.

[38] C. Rousseaux et al. “Effects of density scale length on backward and forward stimulated Raman scattering in 0.53 m laser–plasma interaction”. In: *Physics of Fluids B: Plasma Physics* 5.3 (1993), pp. 920–931.

[39] Kojima Sadaoki. “Generation mechanism of relativistic electron beams by high-intensity-laser-plasma interactions”. In: *PhD thesis* (2017). DOI: 10.18910/61503. URL: http://hdl.handle.net/11094/61503.

[40] H. Sakagami and K. Nishihara. “Three-dimensional Rayleigh-Taylor instability of spherical systems”. In: *Phys. Rev. Lett.* 65 (4 1990), pp. 432–435. DOI: 10.1103/PhysRevLett.65.432. URL: https://link.aps.org/doi/10.1103/PhysRevLett.65.432.

[41] Tatsuhiko Sato et al. “Features of Particle and Heavy Ion Transport code System (PHITS) version 3.02”. In: *Journal of Nuclear Science and Technology* 55.6 (2018), pp. 684–690.

[42] H. Sawada et al. “Flash Kalpha radiography of laser-driven solid sphere compression for fast ignition”. In: *Applied Physics Letters* 108.25 (2016). ISSN: 00036951. DOI: 10.1063/1.4954383. URL: http://dx.doi.org/10.1063/1.4954383.

[43] W. Seka et al. “Convective stimulated Raman scattering instability in UV laser plasmas”. In: *Physics of Fluids* 27.8 (1984), pp. 2181–2186. ISSN: 10706631.

[44] W Seka et al. “Two-plasmon-decay instability in direct-drive inertial confinement fusion experiments Two-plasmon-decay instability in direct-drive inertial confinement”. In: *Physics of Plasmas* 16.2009 (2009), p. 052701.

[45] H. Shiraga et al. “Laser-imploded core structure observed by using two-dimensional x-ray imaging with 10-ps temporal resolution”. In: *Review of Scientific Instruments* 66.1 (1995), pp. 722–724. DOI: 10.1063/1.1146482.

[46] H. Shiraga et al. “Multi-imaging x-ray streak camera for ultrahigh-speed two-dimensional x-ray imaging of imploded core plasmas (invited)”. In: *Review of Scientific Instruments* 75.10 (2004), pp. 3921–3925. DOI: 10.1063/1.1789249.

[47] S. Skupsky et al. “Improved laser-beam uniformity using the angular dispersion of frequency-modulated light”. In: *Journal of Applied Physics* 66.8 (1989), pp. 3456–3462. DOI: 10.1063/1.344101.

[48] A. A. Solodov and R. Betti. “Stopping power and range of energetic electrons in dense plasmas of fast-ignition fusion targets”. In: *Physics of Plasmas* 15.4 (2008), p. 042707. DOI: 10.1063/1.2903890.

[49] M. Tabak et al. “Review of progress in Fast Ignition”. In: *Physics of Plasmas* 12.5 (2005), p. 057305. DOI: 10.1063/1.1871246.

[50] W. Theobald et al. “Spherical strong-shock generation for shock-ignition inertial fusion”. In: *Physics of Plasmas* 22.5 (2015). ISSN: 10897674.

[51] V. T. Tikhonchuk et al. “Quasistationary magnetic field generation with a laser-driven capacitor-coil assembly”. In: *Physical Review E* 96.2 (2017), pp. 1–10. ISSN: 24700053.

[52] K. Tsubakimoto et al. “Suppression of interference speckles produced by a random phase plate, using a polarization control plate”. In: *Optics Communications* 91.1 (1992), pp. 9 –12. ISSN: 0030-4018. DOI: https://doi.org/10.1016/0030-4018(92)90091-5. URL: http://www.sciencedirect.com/science/article/pii/0030401892900915.

[53] G. B. Whitham. “A new approach to problems of shock dynamics Part I Two-dimensional problems”. In: *Journal of Fluid Mechanics* 2.2 (1957), 145–171. DOI: 10.1017/S002211205700004X.

[54] B. J. Winjum et al. “Anomalously hot electrons due to rescatter of stimulated raman scattering in the kinetic regime”. In: *Physical Review Letters* 110.16 (2013), pp. 1–5. ISSN: 00319007.

[55] C. Yamanaka et al. “Nd-doped phosphate glass laser systems for laser-fusion research”. In: *IEEE Journal of Quantum Electronics* 17.9 (1981), pp. 1639–1649. ISSN: 0018-9197. DOI: 10.1109/JQE.1981.1071341.

[56] R. Yan, J. Li, and C. Ren. “Intermittent laser-plasma interactions and hot electron generation in shock ignition”. In: *Physics of Plasmas* 21.6 (2014), p. 062705.

[57] R. Yan et al. “Generating energetic electrons through staged acceleration in the two-plasmon-decay instability in inertial confinement fusion”. In: *Phys. Rev. Lett.* 108 (17 2012), p. 175002.

[58] U Zastrau et al. “Focal aberrations of large-aperture HOPG von- Hàmos x-ray spectrometers”. In: *Journal of Instrumentation* (2012).